

6-2020

Designing Metal-Organic Frameworks for Natural Gas Storage and Delivery

Labeeb Ali

Follow this and additional works at: https://scholarworks.uaeu.ac.ae/chem_petro_theses



Part of the [Chemical Engineering Commons](#)

Recommended Citation

Ali, Labeeb, "Designing Metal-Organic Frameworks for Natural Gas Storage and Delivery" (2020). *Chemical and Petroleum Engineering Theses*. 7.

https://scholarworks.uaeu.ac.ae/chem_petro_theses/7

This Thesis is brought to you for free and open access by the Chemical and Petroleum Engineering at Scholarworks@UAEU. It has been accepted for inclusion in Chemical and Petroleum Engineering Theses by an authorized administrator of Scholarworks@UAEU. For more information, please contact fadl.musa@uaeu.ac.ae.

United Arab Emirates University

College of Engineering

Department of Chemical and Petroleum Engineering

DESIGNING METAL-ORGANIC FRAMEWORKS FOR NATURAL
GAS STORAGE AND DELIVERY

Labeeb Ali

This thesis is submitted in partial fulfillment of the requirements for the degree of
Master of Science in Chemical Engineering

Under the Supervision of Dr. Eyas Mahmoud

June 2020

Declaration of Original Work

I, Labeeb Ali, the undersigned, a graduate student at the United Arab Emirates University (UAEU), and the author of this thesis entitled “*Designing a Metal-Organic Framework for Natural Gas Storage and Delivery*,” hereby, solemnly declare that this thesis is my own original research work that has been done and prepared by me under the supervision of Dr. Eyas Mahmoud, in the College of Engineering at UAEU. This work has not previously been presented or published or formed the basis for the award of any academic degree, diploma, or a similar title at this or any other university. Any materials borrowed from other sources (whether published or unpublished) and relied upon or included in my thesis have been properly cited and acknowledged in accordance with appropriate academic conventions. I further declare that there is no potential conflict of interest with respect to the research, data collection, authorship, presentation, and/or publication of this thesis.

Student's Signature:



Date: 05/07/2020

Copyright © 2020 by Labeeb Ali
All Rights Reserved

Approval of the Master Thesis

This Master Thesis is approved by the following Examining Committee Members:

- 1) Advisor (Committee Chair): Dr. Eyas Mahmoud

Title: Assistant Professor

Department of Chemical and Petroleum Engineering

College of Engineering

Signature 


Date: 5/7/2020

- 2) Member: Professor Nayef Mohamed Ghasem

Title: Professor

Department of Chemical and Petroleum Engineering

College of Engineering

Signature 

Date: 6/7/2020

- 3) Member (External Examiner): Professor Matthew Hill

Title: Associate Professor

Department of Chemical Engineering

Institution: Monash University, Australia

Signature 

Date: 22/6/2020

This Master Thesis is accepted by:

Dean of the College of Engineering: Professor Sabah Alkass

Signature  _____ Date 7/7/2020 _____

Dean of the College of Graduate Studies: Professor Ali Al-Marzouqi

Signature  _____ Date July 9, 2020 _____

Copy ____ of ____

Abstract

Natural gas is major resource in UAE, constitute about 90% methane and as compared to other fossil fuels, it is more environmentally friendly. Energy demand from natural gas can be projected to exceed two hundred exajoules per year in 2040. In the UAE, many natural gas filling stations are already built for utilizing natural gas as a vehicle transportation fuel where these materials have potential applications to store and deliver this fuel. This research aims to study various kinds of Metal-Organic Frameworks, and to investigate adsorption properties for the storage of natural gas and its delivery. MOFs possess porous material that exhibits a high deliverable capacity of gases. These are synthesized using strategies such as crystal engineering with varying organic groups such as linker length and hydrophilicity, pore shape, and phase changes. The main challenges in designing MOFs for methane storage are understanding the mechanical properties, developing thermal management solutions, and the effect of impurities on the working capacity as well as the manufacturing costs of MOFs. This thesis gives pathway to tackle such problems. Overall, HKUST-1 showed promising results for the various MOFs tested. Synthesis and characterization were done by scanning electron microscope, thermogravimetric analysis, X-ray diffraction, and nitrogen adsorption. Adsorption process, reaction heat, and total heat involved in the process were studied using Tian-Calvet calorimeter and gas chromatography. A significant part of this research was dedicated to designing and setting up the calorimeter used in obtaining the heat of adsorption. Moreover, the adsorption properties and separation of the gaseous mixture are also studied using the gas chromatography with some equipment modifications. Designing of MOFs, a class of adsorbents, is described considering the thermodynamics of adsorption of these porous materials for natural gas and methane storage. The thermodynamics of adsorption governs the adsorption isotherm and, therefore the deliverable capacity of stored natural gas and methane. Calorimetric and gas chromatography studies indicated that HKUST-1 has the best adsorbent among the tested MOFs.

Keywords: Metal-organic frameworks, methane storage, ANG; natural gas storage, synthesis, characterization, gas chromatography adsorption, adsorption calorimeter.

Title and Abstract (in Arabic)

تصميم الأطر المعدنية العضوية لتخزين وتسليم الغاز الطبيعي

الملخص

يعد الغاز الطبيعي أحد الموارد الطبيعية الرئيسية في دولة الإمارات العربية المتحدة ، ويتكون من حوالي 90% من الميثان ، اعتمادًا على المصدر ، وهو أكثر صداقة للبيئة مقارنة بالوقود الأحفوري الآخر. وباعتبارها ثاني أكبر مصدر للطاقة ، من المتوقع أن يتجاوز الطلب على الطاقة من الغاز الطبيعي مائتي إكسجول سنويًا في عام 2040. في الإمارات العربية المتحدة ، تم بالفعل إنشاء العديد من محطات تعبئة الغاز الطبيعي لاستخدام الغاز الطبيعي كوسيلة نقل وقود للمركبات حيث يكون لهذه المواد تطبيقات محتملة لتخزين هذا البحث إلى دراسة والتحقق من خصائص الامتزاز لأنواع مختلفة من الهياكل المعدنية العضوية (MOFs) لتخزين وتسليم الغاز الطبيعي. MOFs هي مواد مسامية ذات قدرة عالية على نقل الغازات. يتضمن تركيب MOFs استراتيجيات مثل هندسة الكريستال المستخدمة لتجميع MOFs عن طريق تغيير المجموعات العضوية مثل طول الرباط والرطوبة ، شكل المسام ، وحتى تغييرات الطور. تتم مناقشة استراتيجيات التصميم هذه من حيث الإدارة الحرارية ، والخصائص الميكانيكية ، وتأثير الشوائب على العمليات الناتجة بالإضافة إلى التصنيع الصناعي وتكلفة ال MOFs. يتم تصنيع المواد المسامية ودراسة خصائصها بالحيود بالأشعة السينية ، المجهر الإلكتروني الماسح ، والتحليل الحراري الوزني. يتم تحديد مسامية هذه المواد عن طريق امتصاص النيتروجين. تتم دراسة عملية الامتزاز وحرارة التفاعل والحرارة الكلية التي تطورت في العملية والخصائص الأخرى باستخدام جهاز قياس السرعات الحرارية للغاز. يعد تصميم وإعداد مقياس السرعات الحرارية لاختبار حرارة امتزاز MOFs جزءًا رئيسيًا من هذا البحث. بالإضافة إلى ذلك ، يمكن استخدام معلمات مختلفة لتحليل خصائص الكتلة ونقل الحرارة لنظام الغاز ، والتي يمكن توفيرها من المسعرات الحرارية لدراسات امتزاز الغاز. يوصف تصميم MOFs ، فئة من الممتزات ، بالنظر في الديناميكا الحرارية لامتناس هذه المواد المسامية للغاز الطبيعي وتخزين الميثان. تحكم الديناميكا الحرارية للامتصاص متساوي الامتناس وبالتالي القدرة على تسليم الغاز الطبيعي والميثان المخزنين. يتم أيضًا بحث الخصائص الديناميكية الحرارية للامتزاز من أجل زيادة القدرة على التسليم إلى أقصى حد.

مفاهيم البحث الرئيسية: الأطر المعدنية العضوية ، تخزين الميثان ، ANG ؛ تخزين الغاز الطبيعي ، توليف ، توصيف ، امتزاز اللوني للغاز ، مقياس السرعات الحرارية للامتزاز.

Acknowledgments

All praises are for The Almighty who helped me along the way to make it happen. Firstly, I would like to express my sincere thanks and gratitude to my advisor and mentor Dr. Eyas Mahmoud for his continuous encouragement, invaluable guidance, precious support, and valuable pieces of advice throughout this work. I appreciate his professionalism and academic ethics approachability blended in a friendly environment, which I have enjoyed throughout my entire studies.

Secondly, I would also like to acknowledge all members of the Chemical and Petroleum Engineering Department at the UAE University for their kind assistance during my studies and research. I would like to thank all lab engineers and lab mates for their significant support and assistance throughout my master program.

Finally, I must express thanks to my parents and family for their lifelong love and constant support. I cherish their motivation and encouragement during my research studies. I am grateful to them for believing in me.

Dedication

To my beloved parents and family

Table of Contents

Title	i
Declaration of Original Work	ii
Copyright	iii
Approval of the Master Thesis	iv
Abstract	vi
Title and Abstract (in Arabic)	vii
Acknowledgments.....	viii
Dedication	ix
Table of Contents	x
List of Tables.....	xii
List of Figures	xiii
List of Abbreviations.....	xv
Chapter 1: Introduction	1
1.1 Overview	1
1.2 Statement of Problems	4
1.3 Research Objectives	5
1.4 Limitation of the study	5
1.5 Organization of Thesis	6
Chapter 2: Literature Review	8
2.1 Introduction	8
2.2 Thermal Properties	13
2.3 Mechanical Properties	21
2.4 Natural Gas Impurities	23
2.5 Design Strategies of MOF for Methane Storage.....	24
2.5.1 Mesoporosity or Porosity Engineering.....	26
2.5.2 Linker Engineering.....	28
2.5.3 Functionalization of MOFs	30
2.5.4 Flexible MOFs.....	31
2.6 Practical Implementation	33
Chapter 3: Experimental Work	35
3.1 Materials.....	35
3.2 Synthesis	35
3.2.1 MOF-5	35
3.2.2 HKUST-1	37
3.2.3 Magnesium MOF	38

3.2.4 Calcium MOF.....	40
3.2.5 ZIF-1	41
3.2.6 ZIF-10.....	42
3.3 Instrumentation	43
3.3.1 X-Ray Diffraction	43
3.3.2 Scanning Electron Microscope (SEM).....	44
3.3.3 Thermogravimetric Analysis (TGA).....	45
3.3.4 Nitrogen Adsorption Setup.....	45
3.3.4.1 System Description.....	46
3.3.5 Gas Chromatography Setup	47
3.3.5.1 Column Packing	49
3.3.5.2 Methane gas filling	51
3.3.6 Calorimeter Design and Setup.....	51
3.3.6.1 Experimental Procedure	54
3.3.6.2 Calorimetric cell	55
3.3.6.3 Pyrex Glass Cell	59
3.3.6.4 Vacuum Pump	60
3.3.6.5 Calorimeter Stand.....	61
3.3.6.6 Calorimeter Constructed.....	63
Chapter 4. Results and Discussion	65
4.1 Characterization of MOFs by XRD	65
4.2 Nitrogen Adsorption	67
4.3 Scanning Electron Microscope	71
4.4 Thermogravimetric Analysis.....	73
4.5 Gas Chromatography Adsorption	76
4.5.1 Methane Gas Adsorption.....	76
4.5.2 Methane - Carbon dioxide Adsorption.....	80
4.6 Adsorption analysis using Calorimeter	82
4.6.1 Spurious Heat	84
4.6.2 Heat of adsorption of MOFs using the calorimeter.....	86
Chapter 5: Conclusion.....	91
References	93
List of Publications	108

List of Tables

Table 1: Pore volume, uptake, and deliverable capacity of selected MOFs	19
Table 2: Parts required for building the calorimeter	54
Table 3: Specification of vacuum pump	61
Table 4: Parts of calorimeter labeled as numbered in the figure.....	64
Table 5. Crystallographic data for the synthesized MOFs ¹	67
Table 6: Parameter for Gas Chromatography	77
Table 7: The heat of adsorption for different MOFs synthesized obtained from the calorimeter	88

List of Figures

Figure 1: Challenges associated with the implementation of MOFs for natural gas storage	13
Figure 2: Thermal and mass transport during gas adsorption in a MOF	17
Figure 3: Variable-temperature equilibrium isotherms for (a) Co(bdp), and (b) Fe(bdp), and differential enthalpies for (c) Co(bdp), and (d) Fe(bdp).....	20
Figure 4: Gas adsorption in HKUST-1	22
Figure 5: Isotherms for methane uptake in ST-2 MOFs at different temperatures and (0-200bar).....	26
Figure 6: The CH ₄ gravimetric/volumetric working capacities (between 5.8 and 65 bar) for UTSA-110a in comparison to best robust MOFs reported.....	28
Figure 7: Organic Ligand H4L1 and H4L4 linkers in (a) NOTT-101a, (b)UTSA-76.....	31
Figure 8: Methane storage in flexible Co(bpd) and its effects on pressure	32
Figure 9: Chemical synthesis of MOF-5	36
Figure 10: Chemical synthesis of HKUST-1	38
Figure 11: Synthesis of Mg-MOF	39
Figure 12: Synthesis of Ca-BTC	40
Figure 13: Chemical synthesis of ZIF-1	41
Figure 14: Synthesis of ZIF-10	42
Figure 15: XRD Machine.....	44
Figure 16: Scanning Electron Microscope	45
Figure 17: Nitrogen Adsorption Experimental Setup	46
Figure 18: Gas Chromatography Shimadzu GC-2014	48
Figure 19: Gas chromatography setup	49
Figure 20: Gas-tight syringe for injection.....	49
Figure 21: GC column packing apparatus.....	50
Figure 22: Column packed with MOF and glass wool	50
Figure 23: Methane gas filling into the syringe	51
Figure 24: Calorimeter sketch.....	53
Figure 25: Construction of calorimetric cell	56
Figure 26: Thermodynamic assessment apparatus.....	58
Figure 27: Fixing of thermopiles in calorimetric cell	59
Figure 28: Sample cell preparation	60
Figure 29: The vacuum pump used for calorimeter setup.....	61
Figure 30: Sketch of calorimeter stand	62
Figure 31: Calorimeter assembled and labeled	63
Figure 32: Simulated and experimental XRD patterns for the prepared MOF.....	66

Figure 33: Degassing HKUST-1 before nitrogen adsorption experiment	69
Figure 34: Nitrogen Adsorption-Desorption isotherms of HKUST-1 at 77 K	69
Figure 35: Nitrogen Adsorption-Desorption isotherms of MOF-5 at 77 K	70
Figure 36: Sample prepared for analysis.....	71
Figure 37: SEM images of different MOFs	72
Figure 38: TGA and DTG curves of different MOFs	74
Figure 39: GC graphs of inert column (left side) and HKUST-1 packed column (right side) for various injections of methane	78
Figure 40: Calibration curve for inert column injections.....	80
Figure 41: Analysis of gaseous mixture using GC	81
Figure 42: HKUST-1 activation.....	83
Figure 43: Pyrex glass cell packed with MOFs and glass chips	83
Figure 44: Heat Flux vs. Time for Spurious heat of compression	85
Figure 45: Linear correlation of spurious heat for gas dosage at different pressure	86
Figure 46: Heat Flux vs. Time for different MOFs.....	87
Figure 47: $\ln Q_{ad}$ vs. ΔP for HKUST-1, NICS-6, and MOF-5.....	89

List of Abbreviations

AFC	Advanced flow controller
ANG	Adsorbed natural gas
ASAP	Accelerated surface area and porosimeter analyzer
BASF	Badische anilin und soda fabrik
BDC	Benzene dicarboxylate
Bdp	Benzene dipyrazolate
BET	Brunauer-Emmett-Teller
Bi	Biot Number
BTB	Benzene tribenzoate
BTC	Benzene tricarboxylate
CNG	Compressed natural gas
CSD	Cambridge structural database
DMF	Dimethylformamide
Dobdc	2,5-dioxido-1,4-benzenedicarboxylate
DOE	Department of Energy
EDM	Electro Discharge Machining
GC	Gas chromatography
GCMC	Grande Canonical Monte Carlo
HPLC	High-performance liquid chromatography
IAST	Ideal adsorption solution theory
IRMOF	Isorecticular metal-organic framework
LAG	Liquid assisted grinding
LCD	Liquid crystal display

LNG	Liquified natural gas
MOF	Metal-organic framework
NGV	Natural gas vehicles
PCP	Porous coordination polymer
SBU	Secondary Building units
SEM	Scanning electron microscope
ST	Shanghai University Tech
STP	Standard temperature and pressure
TBM	Tert-butyl mercaptan
TCD	Thermal conductivity Detector
TGA	Thermogravimetric Analysis
UHP	Ultra-high purity
XRD	X-Ray diffraction

Chapter 1: Introduction

1.1 Overview

Natural gas, constituting methane as a prime component, has gained the research interest of many as a substitute to the petroleum category conventional fuels used for running vehicles due to its plentiful reserves. It is proven to be an exceptional alternate to that of petroleum due to its steady cost (since 2000), releases less carbon dioxide as compared to petroleum, and owes a high-octane number (Alvarez et al., 2012). Therefore, natural gas is focused for storing in a material known as metal-organic frameworks (MOF). In the case of adsorbed natural gas (ANG), it needs to be designed to meet performance requirements. These materials should be able to adsorb material and deliver it with high efficiency, requiring a high surface area and porosity (Morris & Wheatley, 2008). Currently, compressed natural gas (CNG) is the major energy source for the cars in UAE, but CNG necessity of high-pressurized tanks on vehicles are associated with safety concerns. Methane sorption by sorbent materials takes substantial heat amount, cooling of the whole tank, cooling down methane and preventing the ignition. As a result, while considering the safety the sorbent materials presence within the pressurized tanks provide an additional benefit as compared to CNG tanks.

The metal-organic frameworks are a new class of hybrid solids like zeolite, also recognized as porous coordination polymers. These hybrid solids are generally crystalline complexes made up of organic multidentate ligands, clusters, or metal ions. The extended network structures are formed by joining the two components with a covalent bond (Yaghi & Li, 2009). In the past few years, MOF chemistry is emerging

at an astonishing pace, indicated by an upsurge in original researches and review articles. The MOF exhibits extraordinarily great surface areas and permanent in porosity. The maximum surface areas of MOFs reported so far are more than 6,000 m²/g. The MOFs are crystalline solids in nature; therefore, precise locations of all atoms inside the framework can be easily recognized and correlated by measured properties. MOFs are usually synthesized under moderately mild conditions. The pore shape, pore size, surface functionalities, and network topology of MOFs can be tuned systematically. This suggest that the properties and structure of metal organic frameworks might be customized to match the requirements of the definite application. The storage of methane gas has been explored with MOFs. In 1997, the first-ever measurement on porous MOFs was done (Kondo et al., 1997). The implication of metal-organic frameworks for the storage of methane gas has not gained ample consideration as compared to CO₂ capture and H₂ storage. Linkers perform an essential role in enhancing the MOFs adsorption pattern as per previously published data (Siberio-Pérez et al., 2007). The study of the CPO-27-M series of MOF identified centers of unsaturated metal ions as primary binding sites of methane gas molecules coordinately. High capacities of methane storage have been exhibited by MOFs in research studies using experimental and computational protocols. For instance, a theoretical metal-organic framework called PCN-14 was forecasted to hold 205 v/v (v/v- volume of gas/volume of container) storage capacity (Wilmer et al., 2012). On the other hand, NOTT-107 displayed 213 v/v at the pressure of 35 bar and 298 K temperature.

Similarly, another series, named as MMOF-74, was also estimated for methane storage purposes (Wu et al., 2009). Another MOF which has been studied is UTSA-20. The

methane storage density measured was 0.222 g cm^3 (178 v/v) at 300 K and 340 bar (Guo et al., 2011). PCN-6x (where x=1,6, and 8) has volumetric capacities of 145, 110, and 99 v/v (Yuan et al., 2010). To increase gas storage capacity, it is very important to tune the pore sizes and shapes of porous sorbents very finely. Efforts focused on solely increasing surface area are sometimes not enough. A balance needs to be maintained between pore size, density, surface area, porosity, and many other aspects. With the discovery of hundreds of new porous materials structures every year, more efforts must be performed to assess these materials for their adsorbing capacities, which may fit these criteria. This research mainly focused on three MOFs: HKUST-1, MOF-5, and Mg-MOF (NICS-6). HKUST-1 is on the top of the list because there is a commercial product under the name Basolite C-300. This product is very good methane adsorbent which could be utilized in NGVs. Moving on, MOF-5 is famous for its high BET surface area and high thermal conductivity. This will allow to store huge amounts of methane in very little space, while dissipating heat in an efficient manner. Finally, Mg-MOF was chosen for its high heat capacity due to its dense structure. Along with its high degradation temperature, NICS-6 can withstand huge amounts of adsorption without breakdown.

This work seeks to test the adsorption capacity of new metal-organic frameworks for methane gas storage, which may rectify problems related to increasing methane storage capacity and the safety of having natural gas cylinders in vehicles. Furthermore, heats of adsorption need to be determined to assess the suitability of each material further and to establish a relationship between the structure, adsorption capacity, and experimentally measured thermodynamic values. Moreover, the research aims at a thermodynamic assessment of these adsorbent-adsorbate interactions.

1.2 Statement of Problems

Presently, the relatively less volumetric energy storage density of natural gas is a major challenge in its long-term usage in transportation vehicles, and the fluctuating prices of petroleum make it less reliable fuel source in transportation fuel. Currently, compressed natural gas technology is used to enhance natural gas storage capacity. CNG is basically the storage of natural gas as supercritical fluid in the oversized fuel tank at 200- 300 bar pressure at room temperature. It is suggested to make onboard tanks with thick metal, which makes them large and heavy in weight, whereas, for passenger vehicles, it should be light in weight made up of expensive carbon fibers that are related to safety, cost, and space issues. At -162°C , natural gas can be condensed into a liquid. Liquefied natural gas (LNG) owes lower density and volume as compared to CNG, which proves it to be cost-efficient for long-distance transportation without any local natural gas source where the pipeline cannot reach. However, the cost of cooling natural gas to -162°C is high, making this technology less feasible. Recently, ANG is considered to be a successful scheme for resolving these problems at stabilized pressures, which comprises tanks filling with porous storage materials to store natural gas. Relatively low-pressure tanks will be cheaper, smaller in size and lighter in weight, therefore can lessen the needs of space and cost. However, passenger cars are better for the implication of ANG technology. Hence, it is crucial to synthesize porous materials i.e., (MOFs) for storage and delivering high amounts of methane gas within a range of 65 and 5 bar pressure for full implementation of the natural gas system in passenger vehicles.

1.3 Research Objectives

The objectives of this thesis are:

- To synthesize different MOFs and study them in detail.
- Study and characterize the MOFs synthesized by XRD and nitrogen adsorption methods to calculate the porosity.
- Document the morphologies of different MOFs studied by using instrument SEM (Scanning Electron Microscope).
- Design and construct an experimental set-up for testing adsorption properties of different MOFs.
- Design new MOFs with high storage deliverable capacity of methane gas.

1.4 Limitation of the study

Despite of conducting all protocols successfully, there was some limitation faced during the whole project. One of the goals of this project is to build a high-pressure experimental setup to test the adsorption properties of porous materials. An experimental set-up was designed and sent to a company, Alfain Lab Equipment LLC, for assembly before November 7, 2018. One challenge that was faced in carrying out the goals of the project in a timely fashion is shipment. During shipment, the designed experimental setup was damaged. Therefore, the item was not shipped by the delivery date of March 10, 2019. Because the apparatus contained microchips, there was also a delay during customs clearance. Furthermore, when the equipment was delivered, there were some leakage issues also which took several days to be sorted out.

At the final stage of the project, due to the outbreak of COVID-19 since February 2020 and its declaration as a pandemic, led to the closure of the labs. Therefore, it was not possible to continue the experimental works and became a major hindrance to the completion of my research work. At the starting stage of the project, it was planned to run the adsorption experiment for each MOF synthesized. However, due to the above problems, it was mainly focused on the MOF called HKUST-1, which revealed the best adsorption properties for methane gas storage from literature studies.

The MOFs are synthesized in small scales in the lab. However, for some experiments, more quantity of MOFs was required and synthesizing that much quantity was time-consuming. Usually, to get a MOF synthesized, including filtration, solvent exchange, and activation takes around approximately 5-10 days, and after all these processes, the MOFs are obtained in range of 0.5 - 1.5 g. Whereas, for running the calorimeter experiment only, at least 3.5 g was required for each MOF synthesized.

1.5 Organization of Thesis

The first chapter provides an overview of the research work and a statement of problems which explains methane adsorption research within metal-organic frameworks (MOFs). The chapter continues with the research objectives to be done in the thesis, the challenges faced during the project and ends up with the organization of the thesis. Chapter Two includes recent literature reviewed about MOFs for adsorption of methane, the implementation for storage of natural gas, and the latest advances in designing the metal-organic frameworks for best adsorption properties. Chapter three consists of the experimental procedures carried out for synthesizing MOFs and characterizing MOFs by different methods like nitrogen adsorption, X rays

Diffraction analysis (XRD), Thermogravimetric Analysis (TGA) and SEM (Scanning Electron microscopy). Lastly, adsorption properties of metal-organic frameworks synthesized by two different methods i.e., Gas chromatography (GC) and Calorimeter, are studied in this section. GC modification to study the adsorption properties of MOF, and new calorimeter setup design to study heat of adsorption of MOFs are illustrated. Furthermore, in Chapter Four, the experimental outcomes are discussed. Finally, chapter five summarizes with derived conclusions.

Chapter 2: Literature Review

2.1 Introduction

In 2017, 4.6219 billion tons of oil equivalent were consumed for transportation and other uses (Nathan & Scobell, 2012). Fossil fuel use resulted in the emission of 33 billion tons of CO₂ (EIA, 2010; Id, 2016; Schoedel et al., 2016). In addition to CO₂ emission, the use of fossil fuels resulted in more than the doubling of the price of petroleum since 1998 (BP, 2015; World Bank, 2014; Zhou et al., 2012a). European Union member states committed to a 40% reduction in greenhouse gas emissions, such as CO₂ in the 2030 Climate and Energy Framework (European Council, 2018). In addition, many countries such as the United Kingdom, France, Germany, and parts of the United States and China plan to ban new gasoline vehicles sales by 2040 (Coren, 2018). To address the sustainability and environmental impacts of petroleum as a transportation fuel, renewable energy sources such as hydrogen and biomass are being developed (Akella et al., 2009; Drennen, 1994; Painuly, 2001). At the time when others are looking into alternatives and into making them practically and economically viable, natural gas is a good alternative or substitute to petroleum as a transportation fuel because it has a lower cost, is available, and releases 270 g of CO₂ per mile as compared to the 450 g of CO₂ per mile when gasoline is used as a fuel (ARPA-E, 2012). As of April 2019, there were 27,414,984 natural gas vehicles (NGVs) and 32,211 natural gas fueling stations (NGV Global, 2019).

Natural gas and methane can be stored and delivered as compressed natural gas, liquified natural gas, and adsorbed natural gas. In the case of CNG, natural gas is stored at a pressure of 250 bar (3500 psi) in low-cost steel tanks and delivered as a fuel. CNG

has an energy density of 9.2 MJ L^{-1} , which is 70% less than that of gasoline (Zhou et al., 2012b). However, carrying an extremely pressurized tank raises safety concerns in vehicles in the case of accidents and has an energy cost associated with compression. Furthermore, CNG, which is the established and predominant technology for NGVs, has a driving range of 350–450 km as compared to 400–600 km for gasoline-powered vehicles (ClimateTechWiki, 2012). Based on this, there is a need to develop gas storage technology beyond that which is already established in real-life applications. Further improvements in natural gas storage for NGV technology should seek to improve the driving range to decrease time at the pump and the corresponding number of required tank recharges. Increasing driving range would be helpful in implementing the technology in areas where natural gas filling stations are not as abundant. In addition, the CNG tank that holds the fuel takes up cargo space and technological advancements that decrease the volume of the natural gas fuel tank are beneficial. Another approach to store natural gas is LNG, which has an energy density of 22.2 MJ L^{-1} . Some drawbacks of LNG are the energy and cost associated with liquefaction (-162°C), which present major technological obstacles (Bae & Kim, 2017). Lastly, natural gas can be stored as ANG. Fairly large volumetric capacities of $4\text{--}6 \text{ MJ L}^{-1}$ at pressures of around 35 bar at room temperature for different adsorbents were achieved (Szilágyi et al., 2016). The presence of sorbent materials in high-pressure tanks reduces the pressure requirement of the tanks, making storage and delivery safer and allows for the use of single-stage compressors. ANG may increase the driving range and decrease the volume required of the fuel tank to achieve a specific driving distance as compared to CNG (Liang et al., 2017).

For ANG, different classes of adsorbents were designed and tested for natural gas such as activated carbons, zeolites, porous coordination polymers (PCPs) (Chui et al., 1999), and MOFs (Makal et al., 2012; Menon & Komarneni, 1998; Morris & Wheatley, 2008). These materials have to be able to adsorb and desorb natural gas, which consists of more than 90 mol% methane. In the case of activated carbons, volumetric methane capacities are in the range of 100–170 cm³ (STP) cm⁻³ (Hamza et al., 2016; Himeno et al., 2005; Matranga et al., 1992; Sircar et al., 1996). Zeolites typically have methane uptakes below 100 cm³ (STP) cm⁻³ (Menon & Komarneni, 1998). Cu(BPY)₂SiF₆ (BPY, 4,4-bipyridine), a PCP, has a gravimetric methane uptake of 146 cm³ (STP) g⁻¹ at 298 K and 36 atm (Noro et al., 2000). MOFs were found to have better methane storage capability (more than 170 cm³ (STP) cm⁻³) in part due to their crystallinity, stability, organic functionality, and porosity (Furukawa et al., 2010; Perry et al., 2009; Yaghi et al., 2003).

In 2012, the US Department of Energy (DOE) set new targets for methane storage to achieve a volumetric storage capacity of 350 cm³ (STP) cm⁻³, gravimetric storage capacity of 0.5 g (CH₄) g⁻¹ at room temperature, and capacity of 263 cm³ (STP) cm⁻³ after successful packing and densification. This target for methane storage materials corresponds to a gravimetric capacity of 50 wt.% and a volumetric capacity of 250 g L⁻¹.

MOFs are being designed to meet these storage targets through the variation of properties such as pore size (Guo et al., 2011), pore architecture (Liu et al., 2013), and hydrophobicity (Nguyen et al., 2014). Furthermore, the building-blocks of MOFs may be varied resulting in changes in the nature of organic ligands (Filipe et al., 2012; Zhao

et al., 2011), including ligand length (Zhao et al., 2011) and functionalization (Zhang et al., 2017a; Stock & Biswas, 2012), and metal center (Horcajada et al., 2006) to improve the working capacity of MOFs for natural gas and methane storage (Taylor et al., 2016). To this end, strategies such as breathing MOFs can also be used (Furukawa et al., 2013a; Deng et al., 2012; Li et al., 1999). One benchmark MOF material is HKUST-1, which is composed of $\text{Cu}_2(-\text{COO})_4$ secondary building units (SBUs = secondary building units) with a paddle wheel shape (Gotthardt et al., 2015). It has a surface area of $1800 \text{ m}^2 \text{ g}^{-1}$. For HKUST-1, the amount of methane adsorbed and desorbed between 65 bar and 5 bar, or the deliverable capacity is $190 \text{ cm}^3 (\text{STP}) \text{ cm}^{-3}$ (Li et al., 2015; Gándara et al., 2014; Moellmer et al., 2011). The reported deliverable capacity for HKUST-1 is $153 \text{ cm}^3 (\text{STP}) \text{ cm}^{-3}$ (109 g L^{-1}) at 35 bar. HKUST-1 is available as Basolite C300 in the market (Vikrant et al., 2017; Makal et al., 2012). An isorecticular MOF, IRMOF-6 (IRMOF = isorecticular MOF) showed a gravimetric uptake of $205 \text{ cm}^3 (\text{STP}) \text{ g}^{-1}$ and volumetric uptake of $155 \text{ cm}^3 (\text{STP}) \text{ cm}^{-3}$ at 36 atm, and 298 K. MOF-905 has a value rivaling of $203 \text{ cm}^3 (\text{STP}) \text{ cm}^{-3}$ (145 g L^{-1}) at 80 bar and 298 K (Yan et al., 2017). Other MOFs developed are aluminum MOFs termed as MOF-519 and MOF-520, composed of $\text{Al}_8(\text{OH})_8(-\text{COO})_{16}$ SBUs joined together with triangular BTB (benzene tribenzoate) linkers. MOF-519 has a narrowed size compared to MOF-520 with partially uncoordinated B2B (B2B = back to back) linkers and a Brunauer-Emmett-Teller (BET) surface area of $2400 \text{ m}^2 \text{ g}^{-1}$ which allows it to adsorb $259 \text{ cm}^3 (\text{STP}) \text{ cm}^{-3}$ methane with a high delivery capacity of $210 \text{ cm}^3 (\text{STP}) \text{ cm}^{-3}$ at 65 bar and 298 K (Gómez-Gualdrón et al., 2014a). A plethora of other MOFs were tested as described in review papers (Cohen, 2012; Getman et al., 2012; He et al., 2014; James, 2003; Long & Yaghi, 2009; H. C. Zhou et al., 2012) and others publications

(Farha & Hupp, 2010; Wang & Cohen, 2009). However, MOFs such as HKUST-1 and others do have limitations when implemented for natural gas storage.

For the implementation of MOFs for natural gas or methane storage, a variety of challenges arise, which can decrease uptake and deliverable capacity by up to 50%. As discussed by Mason and others, these challenges in implementation include thermal management, pelletization or densification losses in storage or deliverable capacity, and natural gas impurities (Figure 1) (He et al., 2014; Mason et al., 2014; Makal et al., 2012). These problems can be addressed from a system or materials design perspective (Li et al., 2016; Li et al., 2018; Lin et al., 2017). Here, it is discussed a detail description of how these problems can be addressed through materials design to decrease cost, weight, and space. The known thermal and mechanical properties of MOFs are considered in terms of a total system perspective (Howarth et al., 2016). In the ANG system, adsorption of gas is an exothermic process, and desorption is endothermic, which leads to potentially large changes in temperature that reduce the amount of gas that can be stored and delivered (Babaei et al., 2018). The heat management of MOFs that undergoing phase changes are examined. In the case of pelletization or densification losses on natural gas uptake and deliverable capacity, the mechanical properties of the materials should be considered to avoid pore collapse (Prajwal & Ayappa, 2014). The strategies' functionalization of MOFs can increase the bulk modulus and improve mechanical properties. In addition, natural gas impurities may block active sites and significantly decrease uptake and negatively impact cyclability (He et al., 2014). Effective MOF design strategies to mitigate these problems through pore engineering are discussed.

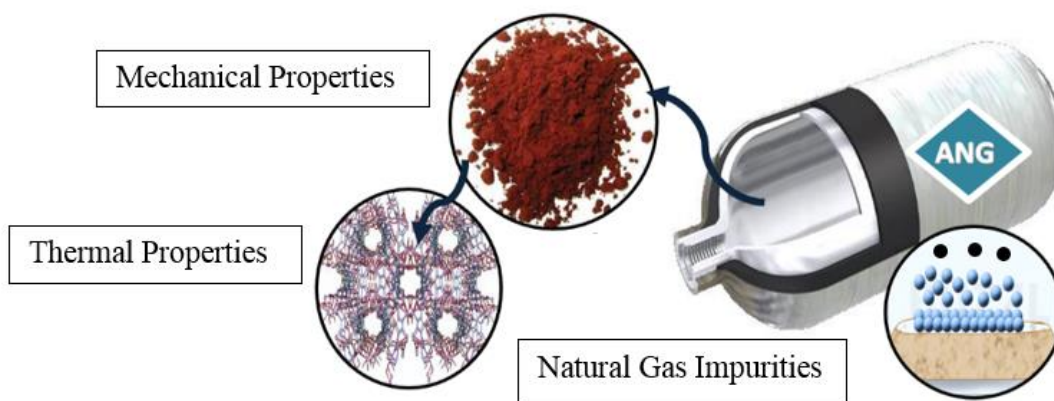


Figure 1: Challenges associated with the implementation of MOFs for natural gas storage

2.2 Thermal Properties

In the ANG system, adsorption of gas is an exothermic process, which leads to a potentially large increase in temperature that reduces the amount of gas that can be adsorbed (Babaei et al., 2018). In addition, desorption of gas is endothermic and can also contribute to a decrease in temperature, decreasing the amount of gas that can be desorbed (Chang & Talu, 1996). Therefore, during the fueling of the tank, the adsorbent bed will release heat and cool during discharge. Fueling the tank at a faster rate, which is often desirable to decrease the time at the tank, leads to even greater temperature changes. During normal driving, experiments have shown that a prototypical carbon tank can cool as much as 37°C, reducing methane storage capacity by 20%, as compared to the isothermal tank (Chang & Talu, 1996). Another negative consequence of this effect is that if the temperature of the tank exceeds the maximum temperature that the tank can tolerate, then the tank would no longer be able to withstand the pressure, and there may be a release of the fuel. From a systems-level

perspective, thermal management may be addressed by the incorporation of a heat exchanger in the system, changing the material of construction, and the geometry of the tank. However, this results in a trade-off between cost, weight, and available space.

Another approach to address thermal management is through material design (Babaei & Wilmer, 2016; Makal et al., 2012). Important properties of MOFs that affect thermal management are heat capacity, decomposition temperature, and thermal conductivity. High heat capacities of MOFs decrease the magnitude of temperature changes during the charging and discharging of the tank. Specific heat capacities of MOF-5, Cu-BTC, Fe-BTC, MOF-177 and MIL-53 (Al) (MIL = Materials Institute Lavoisier) were reported over a wide temperature range (Kloutse et al., 2015). The heat capacities of these MOFs at 300 K are in the range of 0.66 to 0.92 J g⁻¹ K⁻¹. Fe-BTC had the highest heat capacity of the materials studied, followed by MIL-53, MOF-177, and MOF-5. The heat capacities of these MOFs were found to monotonically increase with temperature. Additional thermal analysis and heat capacity studies of Mg-BTC, Co-BTC, Mn-BDC (BDC=1,4-benzenedicarboxylate), MOF-36, and IR-MOF-1 indicated that these MOFs have comparable heat capacities as other solids such as zeolites, carbon nanotubes, and other minerals (Mu & Walton, 2011). Mg-BTC was found to have the highest heat capacity of around 1.4 J g⁻¹ K⁻¹ followed by Co-BTC. Another thermal property to note is the decomposition temperature. Some MOFs were found to not significantly decompose at temperatures as high as 300°C, while other MOFs such as HKUST-1 decompose at temperatures of around 240°C. For MOFs, thermal stability is determined by the coordination number and local coordination environment and is not determined by the topology of the framework.

The structure of MOFs can be designed to increase the thermal conductivity of the MOF to obtain favorable heat transfer properties for natural gas storage and delivery. High thermal conductivities allow for faster dissipation of heat from the system. By decreasing the pore size of MOFs, the thermal conductivity can be simultaneously increased (Babaei et al., 2016). However, it must be noted that there exists an optimal pore size for gas storage. Therefore, the effectiveness of this strategy depends on what the optimal pore size is for storage and whether the designed pore size lies above or below this value. If the pore size is too low for significant uptake, further decreases in pore size do not lead to the achievement of the objective of obtaining a reasonable storage capacity while increasing the rate of dissipation of heat. In addition to pore size, pore shape also affects thermal conductivity. MOFs with hexagonal channels have the highest thermal conductivities along the channel direction and lowest thermal conductivities across the channel direction. Furthermore, the interpenetration of MOFs leads to parallel thermal transport pathways as shown by molecular dynamics simulations. This leads to a thermal conductivity that is the sum of the thermal conductivities of the two constituent frameworks (Sezginel et al., 2018). This would allow for more rapid transport of heat. This phenomenon holds for both cubic idealized MOFs and IRMOF-1. In cases where the frameworks are not maximally interpenetrating, and the interframework attraction is high, which is not very common, the thermal conductivity might be lower than that of the sum of the individual frameworks due to the effect of coupling. The coupling factor that is calculated using the force field parameters (σ and ϵ) from molecular dynamics can be used to determine the decrease in thermal conductivity and was minimal for $0.01 < \epsilon < 0.1 \text{ kcal mol}^{-1}$ and $1 < \sigma < 4.5 \text{ \AA}$. These molecular dynamics simulations suggest a new strategy for

the addition of frameworks to form an interpenetrated MOF structure with a larger number of adsorption sites and additional thermal transport pathways for thermal management. However, there may be a drawback to this strategy if the pore volume is too low for gas storage. The gas in the pores affects the thermal conductivity of the system. It was found that the thermal conductance of the MOF adsorption system is dominated by the lattice thermal conductivity and that conductance is reduced as the concentration of gas in the pores increases by transient simulations. The thermal transport is two orders of magnitude faster than gas diffusion. The fast release of heat is hindered by a large thermal resistance at the gas-MOF interface (Figure 2). The gas-MOF interface does not bottleneck the adsorption process. The thermal conductivities of some MOFs were measured. UiO-66, UiO-67, and Cu-BTC have thermal conductivities of $0.11 \text{ W (m}\cdot\text{K)}^{-1}$, $0.19 \text{ W (m}\cdot\text{K)}^{-1}$, and $0.39 \text{ W (m}\cdot\text{K)}^{-1}$, respectively (Huang et al., 2019). The thermal conductivity of MOF-5 was measured to be $0.32 \text{ W (m}\cdot\text{K)}^{-1}$ (Huang et al., 2007). More thermal conductivity data of MOFs is needed.

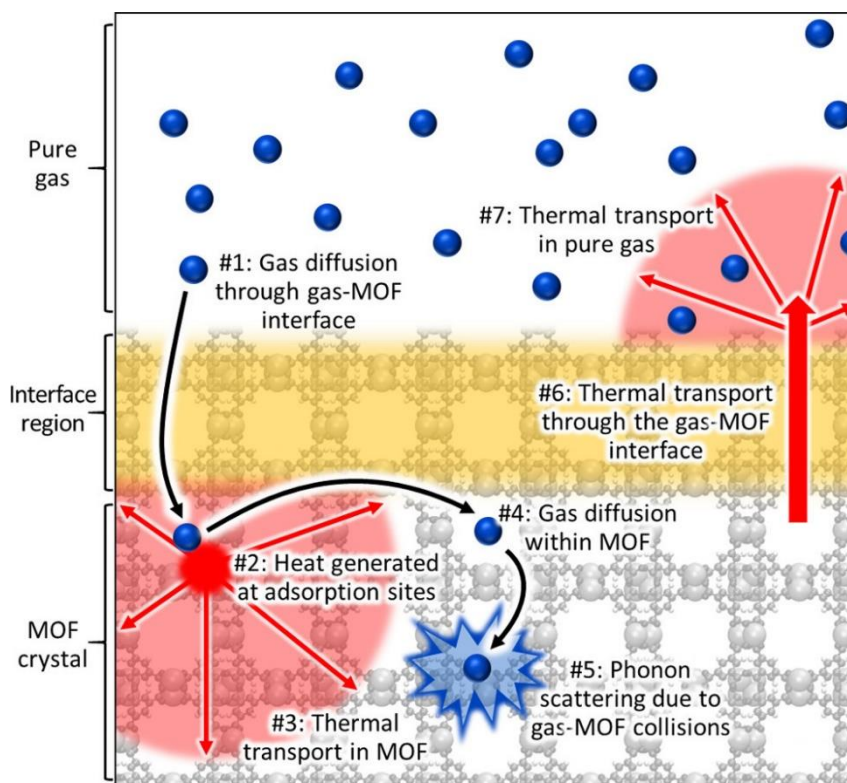


Figure 2: Thermal and mass transport during gas adsorption in a MOF. Reprinted with permission (Babaei et al., 2018)

Another factor to consider is thermal management is that some MOFs strongly interact with natural gas and methane. As a result, there is a heat release associated with the isosteric heat of adsorption (Q_{st}). During the operation of ANG systems, heat may raise the system's temperature and decrease deliverable capacity. In Table 1, the isosteric heat of adsorption of selected MOFs is provided. Q_{st} ranges from around 5 to 25 kJ mol^{-1} . Therefore, thermal management may consider the heat of adsorption of the material to designing MOFs for ANG systems. Lower heats of adsorption may decrease temperature swing during the charging and discharging of the tank. The heat of adsorption can be optimized during the design and selection of the MOF to minimize temperature swings and maximize gas storage and delivery (Bae & Snurr, 2010).

Managing the thermal fluctuations associated with adsorption and desorption presents challenges while maintaining the high capacities required of the system (Mason et al., 2015). Another strategy to address this problem is to select materials that undergo phase transitions to absorb and release heat during adsorption and desorption. For example, the phase transitions of Fe(bdp) (bdp = 1,4-benzenedipyrazolate) and Co(bdp) in response to changes in pressures result in a sharp ‘step’ in the adsorption and desorption isotherms. The phase transition energy can be tuned and was used to manage the temperature change associated with adsorption and desorption.

Adsorption isotherms typically exhibit Langmuir-type isotherms and possess a decreasing rate of the amount of CH₄ adsorbed as the pressure is increased (Figure 3). To overcome this, a material possessing a stepped isotherm was used whereby the adsorbed amount is low at about 5 bar and high at 65 bar. A phase exists that has a collapsed structure in addition to an expanded phase, which can adsorb more methane. The phase transition is reversible and occurs over 100 adsorption cycles. XRD was used to discover that the phase transition occurs around 17 to 23 bar for Fe(bdp) and Co(bdp). The density of the expanded phase (0.77 g cm⁻³) is nearly half of that of the collapsed phase (1.50 g cm⁻³). On the other hand, HKUST-1 and UTSA-76a possess Langmuir-type adsorption isotherms and therefore, a significant amount of CH₄ is left adsorbed at lower pressures of around 5 bar. By changing the material used from Co(bdp) to Fe(bdp), there is a 12% lower heat released per liter of adsorbent and Fe(bdp) released 41% less heat per liter of adsorbent than HKUST-1.

Table 1: Pore volume, uptake, and deliverable capacity of selected MOFs

MOF	V_p (cm^3g^{-1}) ^a	BET (m^2g^{-1})									Q_{ST} kJ mol^{-1}	REF
			Uptake ^b ($\text{cm}^3\text{cm}^{-3}$)	Delivery ^c ($\text{cm}^3\text{cm}^{-3}$)	T (K)	P (bar)	Uptake ^b ($\text{cm}^3\text{cm}^{-3}$)	Delivery ^c ($\text{cm}^3\text{cm}^{-3}$)	T (K)	P (bar)		
PCN-61	1.36	3000	171	127	298	35	219	174	298	65	-	(Furukawa et al., 2013b)
HKUST-1	0.71	1555	190	-	303	35	254	-	303	65	20.7	(Moellmer et al., 2011)
MgMOF-74	0.69	-	200	113	298	35	230	142	298	65	18.5	(Mason et al., 2014)
MOF-5	1.4	-	150	118	298	35	214	182	298	65	12.3	(Mason et al., 2014)
PCN-14	0.83	1984	202	125	298	35	239	160	298	65	17.6	(Mason et al., 2014)
CoMOF-74	0.51	-	221	110	298	35	249	136	298	65	19.5	(Mason et al., 2014)
PCN-61	1.36	3000	171	127	298	35	219	174	298	65	-	(Deng et al., 2010)
MOF-210	3.60	6240	83	71	298	35	143	131	298	65	-	(Furukawa et al., 2013b)
PCN-14	0.85	2000	195	122	298	35	230	157	298	65	18.7	(Peng et al., 2013a)
NU-111	2.09	4930	138	111	298	35	206	179	298	65	14.2	(Peng et al., 2013a)
NU-140	1.97	4300	138	108	298	35	200	170	298	65	14	(Gómez-Gualdrón et al., 2014b)
NU-125	1.29	3120	181	133	298	35	228	180	298	58	15.5	(Wilmer et al., 2013)
NiMOF-74	0.47	1218	214	94	298	35	236	116	298	65	-	(Loiseau et al., 2004)
NU-111	2.09	4930	138	111	298	35	206	179	298	65	15.2	(Peng et al., 2013b)
NOTT-109	0.850	2110	196	125	300	35	242	170	300	65	17.1	(He et al., 2013)
ZJU-5	1.074	2823	190	130	300	35	228	168	300	65	15.3	(Prajwal & Ayappa, 2014)
ZJU-25	1.183	2124	180	132	300	35	229	181	300	63	15.1	(Wen et al., 2014)
NU-135	1.02	2530	187	127	298	35	230	170	298	65	16.6	(Li et al., 2014a)
NOTT-100	0.677	1661	195	104	300	35	230	139	300	65	18.1	(He et al., 2013)

a: V_p : pore volume. b: Total volumetric uptake, cm^3 (STP) cm^{-3} . c: The deliverable amount is defined as the difference in total uptake between 5 bar and the specified upper limiting working pressure under isothermal conditions

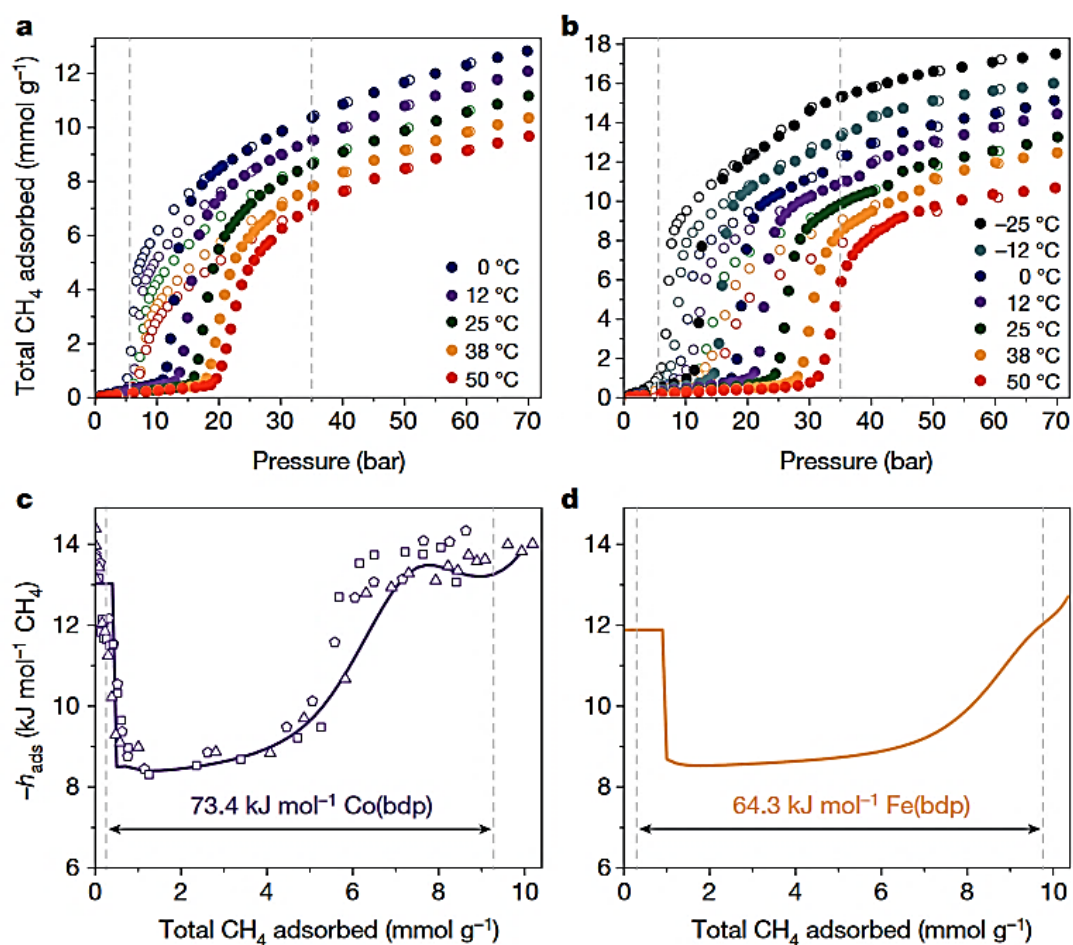


Figure 3: Variable-temperature equilibrium isotherms for (a) Co(bdp), and (b) Fe(bdp), and differential enthalpies for (c) Co(bdp), and (d) Fe(bdp) (Mason et al., 2015)

Figure 3 illustrates the total CH₄ adsorption isotherms at various temperatures for (a) Co(bdp) and (b) Fe(bdp), where a minimum desorption pressure of 5.8 bar and a maximum adsorption pressure of 35 bar are indicated by dashed grey lines. Filled circles represent adsorption; open circles represent desorption. Differential enthalpies of CH₄ adsorption (h_{ads}) for (c) Co(bdp) as determined from variable-temperature adsorption isotherms (purple line) and three separate microcalorimetry experiments (open symbols). Differential enthalpies of CH₄ adsorption (h_{ads}) for (d) Fe(bdp), as

determined by variable-temperature adsorption isotherms. Dashed grey lines in c and d indicate the amount of CH₄ adsorbed at 5.8 bar and 35 bar.

2.3 Mechanical Properties

The volume of gas/volume of the container (V/V) values based on powder adsorption that does not account for losses due to pelletization and bed porosity overestimates the working storage capacity. Furthermore, interparticle void space results in a lower volumetric CH₄ capacity. For onboard applications, the material is extruded or pelletized to reduce the pressure drop. This results in a loss of pore volume and/or surface area (Tian et al., 2015). Compaction can also result in the complete or partial collapse of the framework pores. Pellets of Ni₂(dobdc) (dobdc⁴⁻ = 2,5-dioxido-1,4-benzenedicarboxylate) compacted with 0.1 GPa of pressure adsorbed just 100 v/v of CH₄ at 34 bar and 30°C as compared to 230 v/v before compaction. To meet the Department of Energy target of 263 V/V at the onboard packed bed level, the volumetric loadings for the pelletized sample should be about 373 V/V (Prajwal & Ayappa, 2014). Therefore, MOFs with high mechanical stability is desirable for implementation in ANG systems. These materials can survive compaction without losing their porosity and storage capacity.

To tackle this issue, advanced synthesis engineering and densification of MOFs were used to produce monolithic structures of up to about 1 cm³ in size without high pressure and binders (Tian et al., 2018a). HKUST-1 was synthesized by a sol-gel process and analyzed by optical imaging of the sample as well as powder XRD. The unreacted particles nucleate at the interface connecting the existing primary particles and results in epitaxial growth, yielding a dense monolith. After successful packing and

densification, the monolithic HKUST-1 achieved a capacity of $259 \text{ cm}^3 \text{ (STP) cm}^{-3}$, which is a 50% improvement over any other experimental value and virtually matches the DOE target of $263 \text{ cm}^3 \text{ (STP) cm}^{-3}$ (Figure 4). The hardness of the monolithic HKUST-1 is at least 130% greater than that value measured for other conventional MOFs.

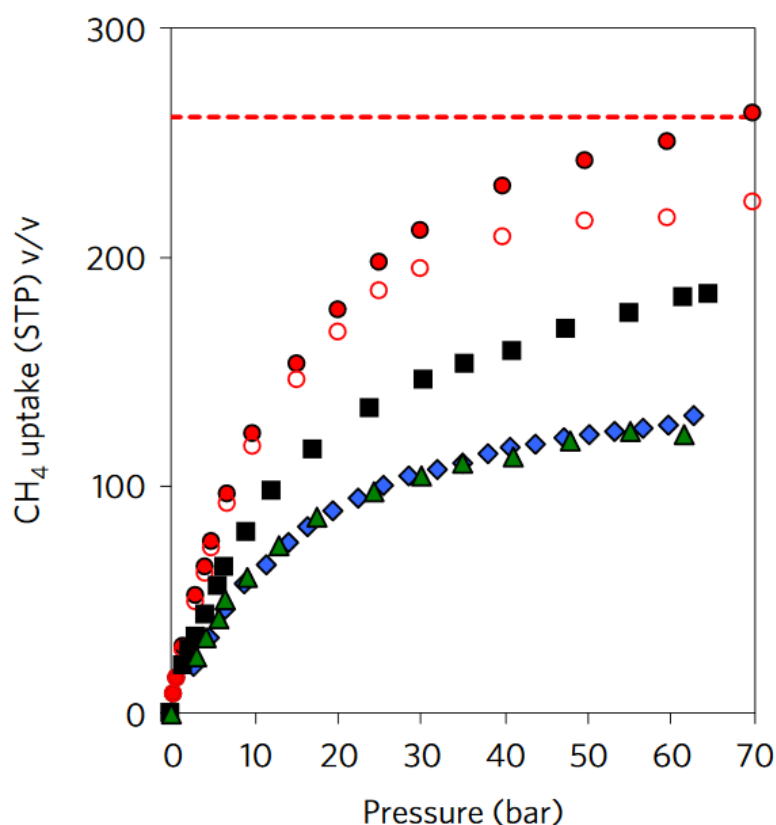


Figure 4: Gas adsorption in HKUST-1 (Tian et al., 2018a)

In Figure 4, the comparison of absolute volumetric methane adsorption isotherms at 298 K on monolithic HKUST-1 (red filled circles), excess volumetric uptake on monolithic HKUST-1 (red open circles), HKUST-1 pellets under hand-packing (blue diamonds), HKUST-1 pellets packed under 27.6 MPa (black squares), and HKUST-1

pellets under 68.9 MPa (green triangles) 5. The DOE target of $263 \text{ cm}^3 \text{ (STP) cm}^{-3}$ is represented by the red dashed line. The mechanical behavior of MOFs can be tuned by functionalization (Yot et al., 2016). UiO-66(Zr) and MIL-125(Ti) and their amino-functionalized derivatives showed a gradual pressure-induced reversible decrease in their crystallinity as determined by high-pressure powder X-ray diffraction up to 3.5 GPa. UiO-66(Zr) has a very high bulk modulus and found to be one of the most resilient MOFs studied. The mechanical behavior of MOFs was correlated to chemical and geometrical features such as metal-oxygen coordination number, the nature of the organic linker, and the porosity and crystal density. In another study, a rationalization was provided relating the mechanical properties of MOFs to framework bonding topology and ligand structure (Moosavi et al., 2018). Functional groups on the organic ligands that comprise the MOF structure can enhance mechanical stability through the formation of a secondary network of nonbonded interactions or can soften the material by destabilizing the bonded network of a MOF. Therefore, mechanical stability may be improved by the selection of functional groups.

2.4 Natural Gas Impurities

Another factor to consider in the implementation of the system is the effect of impurities such as higher hydrocarbons. Natural gas consists of about 90% methane, 3% ethane, 1% C3-C6 hydrocarbons, and 3% nitrogen (Veluswamy et al., 2018). It is not practical to separate all the components other than methane before charging a tank (Sun et al., 2009). These hydrocarbons and impurities can have a deleterious effect and decrease methane storage capacity and affect the long-term stability of the adsorbent. C2 and C3 hydrocarbons may block the binding sites, decreasing deliverable capacity.

Furthermore, the interaction of adsorbent and adsorbate results in heat being adsorbed or desorbed during the operation of ANG systems.

According to a computational study, the adsorbed natural gas tank performance declines, and deliverable energy decreases over 200 operating cycles (Zhang et al., 2015). A ‘cyclic steady-state’ is reached following a monotonic decline. The best MOFs tested at ‘cyclic steady-state’ ordering in increasing performance are MOF-143 > NU-800 > IRMOF-14 > IRMOF-20 > MIL-100 > NU-125 > IRMOF-1 > NU-111. The highest cyclic steady-state energy delivered is 5.43 MJ L^{-1} . HKUST-1 and IRMOF-1 have the best deliverable capacity of $\sim 185 \text{ cm}^3 \text{ (STP) cm}^{-3}$ of adsorbent at pressures between 5.8 and 65 bar. A small amount of higher hydrocarbons can have a significant effect and reduces the deliverable energy to 5.08 MJ L^{-1} .

In another computational study, the impacts of gas impurities from pipeline natural gas on methane storage in MOFs during long-term cycling was studied (Wu et al., 2017). Grande Canonical Monte Carlo (GCMC) and ideal adsorption solution theory (IAST) of multicomponent adsorption were used to study an isothermal tank to assess the accumulation of heavy hydrocarbons and tert-butyl mercaptan (TBM). The deliverable energy was found to reduced up to 50% after 200 cycles. This result again highlights the importance of multicomponent effects on ANG systems.

2.5 Design Strategies of MOF for Methane Storage

There are roughly 70,000 metal-organic compounds, which include 1D, 2D, and 3D structures, as found in the Cambridge structural database (CSD) (Moghadam et al., 2017). To assemble these structures, reticular synthesis is used whereby designed molecular building blocks are judiciously assembled into a network held by strong

covalent bonds, forming a perfect structure (Yaghi & Li, 2009; Tranchemontagne, et al., 2008; Ockwig et al., 2005). The structure or rigidity of building units remains unchanged throughout the reaction, which leads to the formation of a crystalline solid-state framework (O’Keeffe & Yaghi, 2012). The extended network formed by copolymerization of metal ions with organic linkers in ‘Crystal Engineering’ is the process involved in reticular synthesis (Braga & Grepioni, 1999; Moulton & Zaworotko, 2001). Inorganic SBUs are considered primary adsorption sites, where the guest molecule usually binds (Li et al., 2009; Tranchemontagne et al., 2009; Rowsell et al., 2005). MOFs, having metal sites provided with ligands that can be removed, forming a coordinatively unsaturated site called an open-metal site. When SBUs have no open metal sites, guest molecules would stick to organic linkers rather than the inorganic ones (Suh et al., 2008; Eddaoudi et al., 2001). The thermodynamics suggests that MOFs with open metal sites have a stronger interaction with methane as compared to those without open metal sites. This allows for improvements in the deliverable capacity of natural gas or methane storage (Bolinois et al., 2017; Alhamami et al., 2014).

The methane uptake capacity was experimentally tested on six selected MOFs (HKUST-1, PCN-14, NU-125, Ni-MOF-74, NU-111, UTSA-20) (Peng et al., 2013a), due to their pore size and high surface area (Hyeon et al., 2017). It was found that HKUST-1 has a volumetric uptake of $227 \text{ cm}^3 \text{ (STP) cm}^{-3}$ at 35 bar and $267 \text{ cm}^3 \text{ (STP) cm}^{-3}$ at 65 bar (Peng et al., 2013b). In addition, HKUST-1 was able to reduce pressure four-fold when added to storage tanks and reduce the cost associated with high pressures. MOF design strategies are discussed to maximize methane uptake and

delivery by optimizing mesoporosity, linker polarization, functionality, and flexibility to reach the DOE target.

2.5.1 Mesoporosity or Porosity Engineering

The results demonstrate how robust pore engineering can be used to increase deliverable capacity. The inclusion of tight cavities to stronger methane affinity as well as mesoporosity has led to record working capacities.

The introduction of mesoporosity in MOFs led to a record deliverable capacity. Mesoporous $\text{Zn}_4\text{O}(\text{-COO})_6$ -based MOFs were engineered to obtain ultrahigh capacity methane storage. These newly synthesized MOFs are known as ST-1, ST-2, ST-3, and ST-4 (ST= ShanghaiTech University) (Liang et al., 2017). ST-2 surpassed all reported records by achieving a deliverable capacity of $289 \text{ cm}^3 \text{ (STP) cm}^{-3}$ for the pressure range of 5-200 bar, as illustrated in Figure 5. Furthermore, this finding demonstrates how mesoporosity is a critical factor to further improve deliverable capacity at high pressure (200 bar).

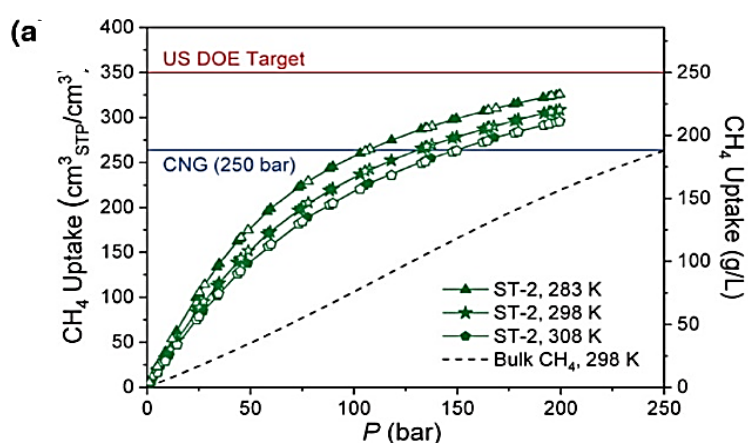


Figure 5: Isotherms for methane uptake in ST-2 MOFs at different temperatures and (0-200bar)

Two essential features of MOFs that impact methane uptake are deep-well “pocket” sites and coordinatively unsaturated metal sites (Dietzel et al., 2009; Ma et al., 2008). Van der Waals interactions occur at the pocket sites and coulombic interactions at the coordinatively unsaturated metal sites. The experiments were done previously to confirm that these are the two binding sites in MOFs (Chen et al., 2012; Sculley et al., 2011). If both these binding sites are adequately arranged, high methane storage capacities may be achieved.

Methane uptake of MOF-950 gradually increases with increasing pressure as it has the smallest pore diameter. The highest methane uptake for this MOF was in the pressure range (20–50 bar) (Jiang et al., 2016). As the pressure increases, excess uptake approaches saturation and is proportional to the surface area (Shen et al., 2015). Volumetric excess uptake is correlated with both the theoretical bulk density and experimental bulk density. It was found that the experimental density of MOF-950 was lower by 5–10 % when compared to its theoretical density. This is due to defects present in MOF crystals. Zn-MOFs were also compared as they are considered low-density MOFs. Methane working capacity can be improved by crystal engineering (Zhang et al., 2017b). By slightly changing MOF-505’s structure and chemistry, methane volumetric deliverable capacity reached $198 \text{ cm}^3 \text{ (STP) cm}^{-3}$. To optimize uptake, the optimal pore diameter and gravimetric surface area are approximately 8 \AA and $2500\text{-}3000 \text{ m}^2 \text{ g}^{-1}$, respectively. The pore size and pore chemistry can be tuned to ensure that there is low uptake at low pressure, which in turn leads to higher deliverable or working capacities. This is done by changing the organic linkers to avoid small pockets in the structure. The interaction between methane and pore walls tuned by

changing the oxamide group to a pyridyl moiety. The introduction of a more hydrophilic structure decreases CH₄-framework interactions.

2.5.2 Linker Engineering

Linker engineering can increase the methane deliverable capacity of MOFs. Linker engineering was used to synthesize NJU-Bai 43 from PCN-14 through slimming, polarizing slimming, and polarizing expansion of the linker H₄L. NJU-Bai 43 has a volumetric capacity of 254 cm³ (STP) cm⁻³ at 65 bar, which is the highest volumetric capacity recorded. This is a fourfold increase in deliverable capacity compared to a tank with only methane (Zhang et al., 2017b). These results illustrate how linker engineering can be useful to boost volumetric and gravimetric methane uptakes and working capacity. NJU-Bai 41, NJU-Bai 42, and NJU-Bai 43 have an adsorption enthalpy of 17.77, 14.49, and 14.45 kJ mol⁻¹, respectively. This change in the enthalpy is due to sub pore polarization and cage elimination, as shown in Figure 6.

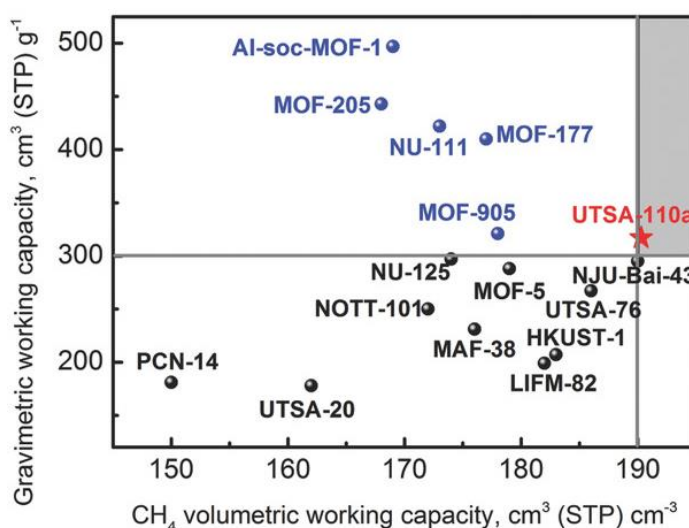


Figure 6: The CH₄ gravimetric/volumetric working capacities (between 5.8 and 65 bar) for UTSA-110a in comparison to best robust MOFs reported (Wen et al., 2018)

In 2018 a MOF was constructed through linker engineering by tweaking functional sites and porosity to achieve high volumetric and gravimetric methane deliverable capacity (Wen et al., 2018). UTSA-110a was designed by using linkers that are highly dense with functional nitrogen sites. This MOF exhibited a volumetric deliverable capacity of $190 \text{ cm}^3 \text{ (STP) cm}^{-3}$ and a gravimetric capacity of $317 \text{ cm}^3 \text{ g}^{-1}$ at 65 bar (Figure 6). The volumetric working capacity and gravimetric working capacity of UTSA-110a are higher than that of the benchmark material, HKUST-1. This can be attributed to the porosity and favorable properties of the linker.

Raman spectroscopy was used to show that linkers within the framework cavities of IRMOFs adsorbed methane. The linkers may be selected in such a way to give the highest affinity to methane. In freshly prepared MOFs, the solvent is coordinated to unsaturated metal centers and is replaced with another solvent that has a lower boiling point. This solvent can be removed under vacuum or heating (Siberio-Pérez et al., 2007). M-MOF-74, also known as CPO-27-M, has primary binding sites at its open metal sites as it was determined by neutron powder diffraction experiments (Wu et al., 2009; Rosi et al., 2003). Experiments show that the advantage to such MOFs lies in their adsorption taking place primarily at these sites, due to the high binding energy of methane when compared to that of other adsorption sites. When one methane molecule gets adsorbed per open metal site, the site was able to store large amounts of methane being equivalent to a volumetric capacity of $165\text{-}175 \text{ cm}^3 \text{ (STP) cm}^{-3}$.

2.5.3 Functionalization of MOFs

Another strategy for improving the storage capacity of MOFs is through immobilizing functional groups. Immobilization can improve the binding strength of the adsorbent (Li et al., 2014b). Although functional groups fulfill this purpose, they occupy space, decreasing the surface area and pore volume, lowering the methane working capacity. UiO type MOFs are known for having highly porous structures with excellent stability, making them favorable materials for methane storage (Wu et al., 2013). One UiO MOF possesses Lewis basic sites that have high structural stability (Li et al., 2014b). In the framework, pyridyl moieties act as Lewis bases with incoming methane to enhance gas uptake capacity (Rao et al., 2013).

For high methane storage, MOFs should have functional sites that improve methane storage capacity at high pressures (Li et al., 2015). NOTT-101 possesses two important properties; tunable functionality with its phenyl rings and high methane storage ability (He et al., 2013). Two ways to functionalize NOTT-101 pores are by synthesizing a functional ligand using nitrogen's Lewis basic sites or combining linkers with various functionalities, like H4L1 and H4L4, as shown in Figure 7 (Lin et al., 2009). Combining suitable functional groups improves the working capacity and the volumetric methane storage by altering the interaction of the adsorbate and adsorbent governed by thermodynamics. Another similar MOF like, UTSA-76 contains the highly concentrated nitrogen sites which have a working capacity of 197 cm^3 (STP) cm^{-3} . Properties such as pore volume, BET surface area, and amounts of nitrogen sites were significant factors in determining methane storage performance (Li et al., 2015).

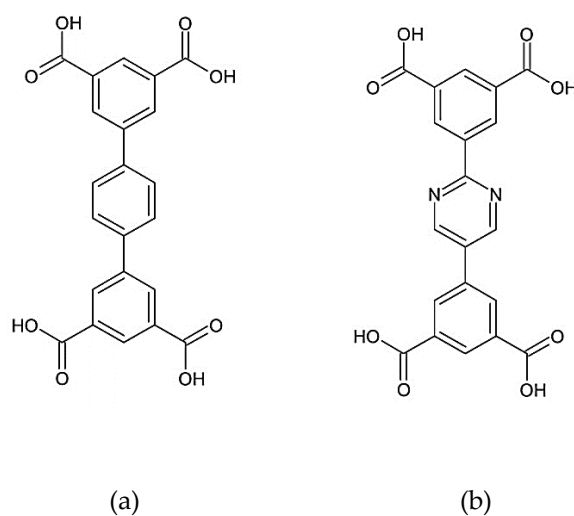


Figure 7: Organic Ligand H4L1 and H4L4 linkers in (a) NOTT-101a, (b)UTSA-76

2.5.4 Flexible MOFs

The MIL-53 MOF family can be synthesized from inorganic SBUs using metals, such as aluminum, iron, gallium, and indium, in addition to organic ligands of benzene-1,4-dicarboxylates. These MOFs have breathing properties that allow them to be highly stable (Boutin et al., 2010; Loiseau et al., 2004; Rallapalli et al., 2010). MIL-53(Al) pores open at low temperatures and pressures, indicating breathing properties because of the low stability of its narrow phase, as shown in Figure 7. At room temperature, hydrogen bonds between amino groups in the ligands and oxygen from the inorganic parts mainly contribute to these breathing properties (Boutin et al., 2010; Loiseau et al., 2004). The deliverable capacity of MIL-53(Al) is low because its large phase is stable. While the low phase is essential for breathable MOFs' performance, MIL-53(Al)-NH₂ completes its transition to the large phase at high pressures (Boutin et al., 2010). When adsorbing methane onto MIL-53(Al)-NH₂, the MOF starts to liquefy under specific temperature and pressure. By calculating the pore volume in each phase,

methane uptake of MIL-53(Al)-NH₂ under high pressure can be estimated as well as the deliverable capacity and compared with MIL-53(Al) (Bolinois et al., 2017). Another closely related structure with breathing property is Co(bpd), closes and opens from a narrow phase to a large phase based on specific properties, such as pressure, and density as illustrated in Figure 6. During methane gas adsorption, this flexible MOF undergoes a transition from collapsed structure to an expanded state, which results in around 90% increase in the unit cell volume, as shown in Figure 6. The methane adsorption increases with elevated pressure while decreases with higher densities. An additional method to enhance methane deliverable capacity is by understanding the hysteresis of adsorption isotherms (Boutin et al., 2010; Loiseau et al., 2004; Mason et al., 2015). With more sorption cycles, the narrow phase can be transferred into a large phase which increases methane working capacity, as the heat builds up from hysteresis.

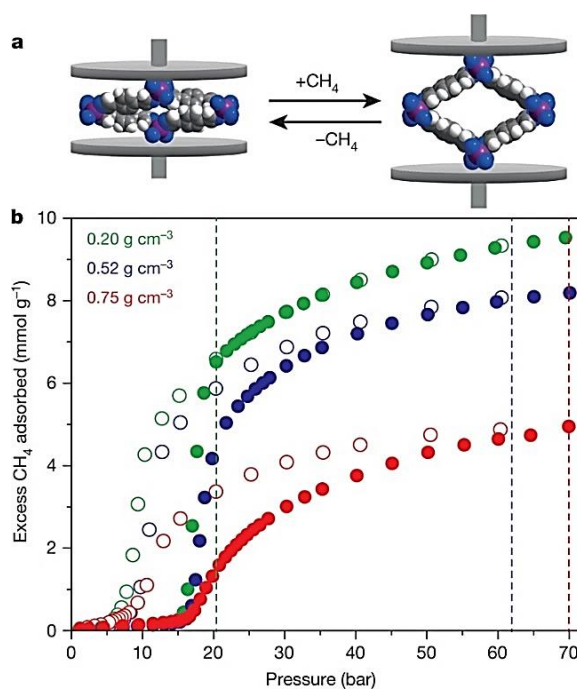


Figure 8: Methane storage in flexible Co(bpd) and its effects on pressure (Mason et al., 2015)

Figure 8 represents (a) Collapsed, and methane expanded Co(bpd) shows the space-filling. Color codes for atoms are carbon; grey, nitrogen; blue, cobalt; purple and green, hydrogen; red. In (b) Methane adsorption isotherms for Co(bpd) at different pressure and varying densities (adsorption- filled circle and desorption- Open circles).

2.6 Practical Implementation

BASF (Badische Anilin und Soda Fabrik), a German chemical company and the largest chemical company producer in the world, fitted fuel tanks packed with BASF MOFs for natural gas storage in transportation application in the EcoFuel World Tour in 2007 (Jacoby, 2008). BASF enhanced the natural gas storage capability by taking advantage of the favorable properties of MOFs, such as their surface areas coupled and their favorable energetics for adsorbing gas. Cylinders filled with MOFs store twice as much gas as do standard cylinders. The test successfully resulted in a six-month, 28,000-mile road trip fueled by natural gas through 40 countries and five continents in a Volkswagen Caddy optimized for natural gas combustion (BASF, 2014). The road trip was aimed at increasing public awareness of the environmental benefits of using natural gas instead of conventional fuels. The MOF-enhanced system provided an overall driving range of more than 1,500 miles between fill-ups. In 2013, BASF followed up with a showcase. A heavy-duty Kenworth truck was equipped with natural gas fuel systems containing BASF MOF materials. In partnership with Quantum Technologies, a storage system was designed that utilized a type IV natural gas storage pressure vessel marking the advancement of MOF technology (Joseph, 2013).

In 2017, BASF continued its MOF commercialization efforts with a focus on higher valued areas, like specialty chemicals (American Chemical Society, 2017). BASF

produced 100 different types of MOFs at the lab scale. The company is selling MOFs via Merck KGaA subsidiary Sigma-Aldrich. HKUST-1, a benchmark MOF for methane storage, is being sold as Basolite C 300. 500 g of Basolite C 300 was sold by Merck for US\$ 9,200. Companies like NUMAT, novoMOF, MOFonics, MOF Technologies, Green Science Alliance Co., Ltd., and BASF have been scaling-up MOF production. NuMAT brought the first MOF-enabled gas storage product to the market in partnership with Linde Group, the second-largest gas company in the world in 2017 (McMahon, 2017). NuMat is now producing hundreds of kg of MOFs in a few hours.

For practical implementation, the cost of MOF manufacture should be considered and minimized (Mueller et al., 2006). A techno-economic analysis was conducted for MOF adsorbents for large-scale manufacture (Rubio-Martinez et al., 2017). $\text{Ni}_2(\text{dobdc})$ ($\text{dobdc}^{4-} = 2,5\text{-dioxido-1,4-benzenedicarboxylate}$; Ni-MOF-74), $\text{Mg}_2(\text{dobdc})$, (Mg-MOF-74), $\text{Zn}_4\text{O}(\text{bdc})_3$ ($\text{bdc}^{2-} = 1,4\text{-benzenedicarboxylate}$; MOF-5), and $\text{Cu}_3(\text{btc})_2$ ($\text{btc}^{3-} = 1,3,5\text{-benzenetricarboxylate}$; HKUST-1) have projected costs in the range of US\$ 35 kg^{-1} to 71 kg^{-1} based on organic solvent for solvothermal syntheses. Alternative synthesis methods such as liquid assisted grinding (LAG), and aqueous synthesis reduces cost by reducing solvent usage and provide cost projections in the range from US\$ 13 kg^{-1} to 36 kg^{-1} (representing 34–83% reductions) for scaled-up manufacture.

Chapter 3: Experimental Work

3.1 Materials

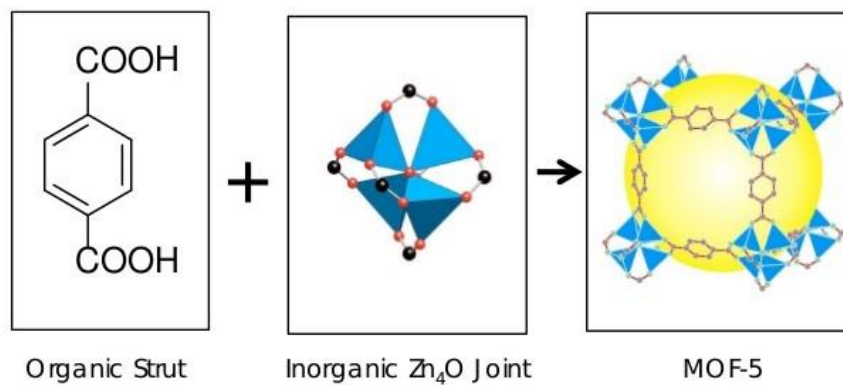
1,3,5-Benzenetricarboxylic acid, copper dinitrate trihydrate, magnesium nitrate tetrahydrate, calcium nitrate tetrahydrate, and chloroform (HPLC Grade) was bought from (Sigma Aldrich). Triethylamine and dimethylformamide were taken from company Fisher Scientific. Zinc nitrate solution, imidazole, and zinc acetate dihydrate were obtained from other departments of the university. All the materials were utilized without any further purification.

3.2 Synthesis

3.2.1 MOF-5

MOF-5 or $Zn_4O(BDC)_3$ is a metal-organic framework that owes an exceptional surface area of about 3000 m²/gram. The MOF-5 synthesis was successfully done as shown in Figure 9 by initially dissolving 16.99 g of zinc acetate dihydrate in 500 mL of dimethylformamide (DMF). Once the inorganic part of MOF-5 was ready, the organic part was prepared by dissolving terephthalic acid (5.06g) and triethylamine (8.5 ml) in 400 mL of DMF. Then the inorganic solution was poured to the organic mixture and stirred for around 15 min; it developed the precipitate and continues stirring the solution for another 2 and ½ hours. The formed precipitate was filtered off entirely and immersed into 250ml DMF overnight. It was then filtered again, and the impurities were removed using the solvent exchange process. The chloroform of HPLC grade 250ml was used as a solvent and replaced at least three times for 7 days. Finally, the precipitate was thoroughly filtered and evacuated at 10 mTorr pressure overnight.

MOF-5 was activated at 120°C and 10 mTorr for 6 hours. The MOF obtained was weighed (6.437g) and stored in the solvent (Tranchemontagne et al., 2008).



(a)



(b)



(c)



(d)

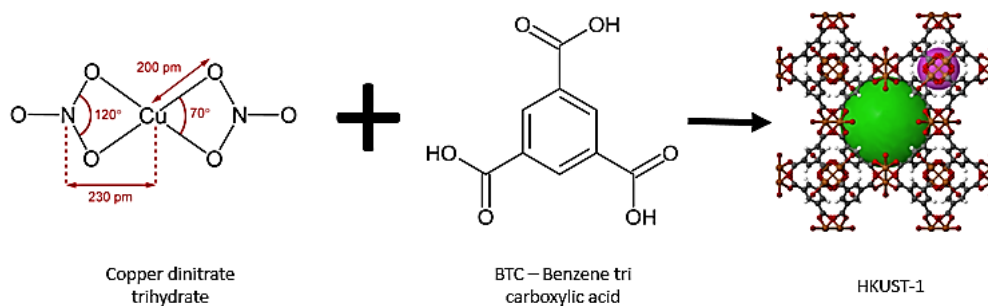


(e)

Figure 9: Chemical synthesis of MOF-5; (a) Structural formula of MOF-5, (b) Filtration of the sample, (c) Filtered sample, (d) Solvent exchange process and (e) Dried MOF-5

3.2.2 HKUST-1

Synthesis of HKUST-1 initiate with a process of stirring mixtures of copper dinitrate trihydrate (0.716g) and benzenetricarboxylic acid (0.421g) with 12ml of ethanol-water combination (50:50) for continuously 30 mins. The concentrated solution was then shifted into a teflon container and then placed into a hydrothermal synthesizer reactor. The reactor lid was closed tightly using the stainless-steel rod. The hydrothermal synthesizer reactor was then kept into an oven, pre-heated at 109°C for 24 hours (1 day). Finally, the hydrothermal synthesizer reactor was allowed to cool down up to room temperature. The solution changed the color into a turquoise blue color. It was then sonicated at an amplitude of 20 for about 8-10 minutes to break the aggregates of micron-sized colloidal particles in the solution. The solution was filtered after sonication by means of Buchner funnel vacuum filtration apparatus for the collection of the precipitate. The precipitate obtained was a turquoise blue color with crystals (HKUST-1, 0.845g) as shown in Figure 10. It was then completely dried under air for 1 day and stored.



(a)

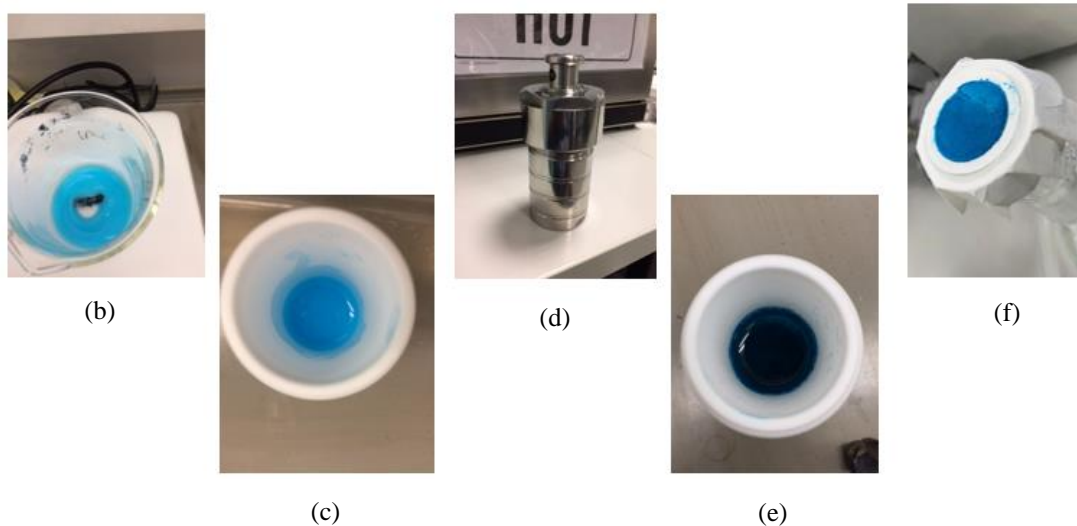
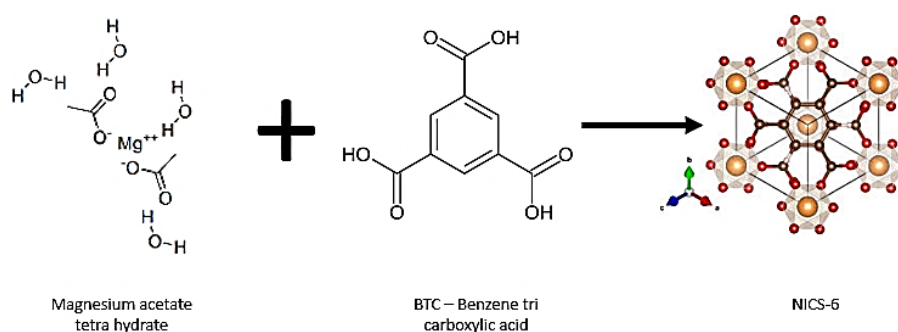


Figure 10: Chemical synthesis of HKUST-1; (a) Structure of HKUST-1, (b) Mixing inorganic and organic parts, (c) Solution transferred to the teflon autoclave, (d) Sample in hydrothermal synthesis reactor, (e) Sample after 24 hours of heating and (f) Synthesized HKUST-1

3.2.3 Magnesium MOF

$\text{Mg}_3(\text{BTC})_2$, Magnesium benzenetricarboxylic acid commonly known as NICS-6, which constitutes trimers of MgO_6 and BTC linkers building up a 3D network. The synthesizing procedure starts with dissolving 0.65 g of each Magnesium acetate tetrahydrate and 1,3,5-benzenetricarboxylic acid in 5 & 12.5 mL of ethanol,

respectively. Both organic and inorganic solutions were combined under vigorous stirring result in the formation of a thick white solution. It was then solvothermal treated in teflon lined hydrothermal synthesizer reactor at 190°C for 24 hours. The solution was filtered using Buchner funnel vacuum filtration to collect the precipitate as shown in Figure 11. The precipitate obtained weighing 0.6g. It was then thoroughly dried under air for 1 day and stored (Mazaj et al., 2013).



(a)

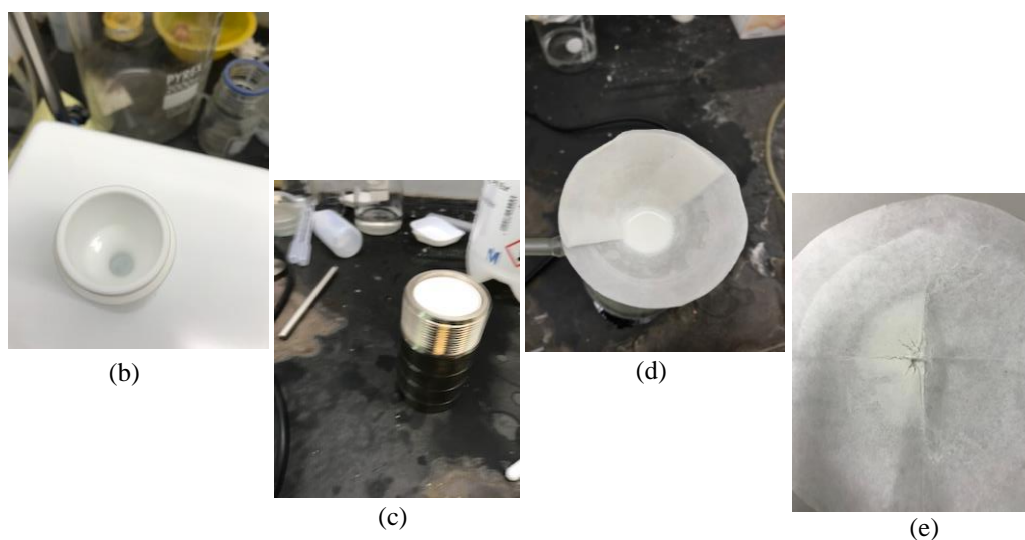
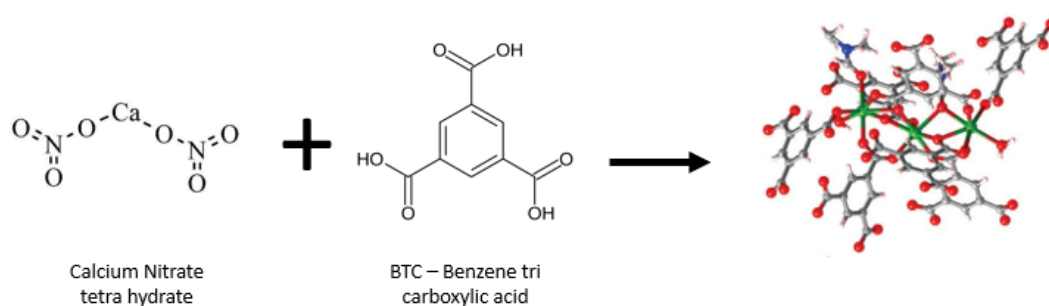


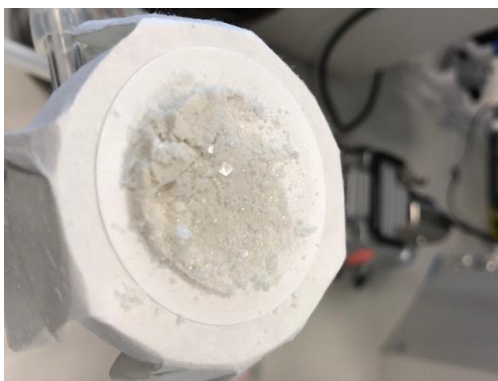
Figure 11: Synthesis of Mg-MOF; (a) Structure of Mg-MOF(NICS-6), (b) Mixing inorganic and organic parts, (c) Sample in hydrothermal synthesizer reactor, (d) Sample filtered and (e) Synthesized NICS-6

3.2.4 Calcium MOF

A homogenous solution was prepared using a mixture of 1, 3, 5-benzenetricarboxylic acid (0.1 mM, 0.021 g), calcium nitrate tetrahydrate $\text{Ca}(\text{NO}_3)_2 \cdot 4\text{H}_2\text{O}$ (0.3 mM, 0.0708 g), 5 ml of DMF, and 1.0 ml of water by stirring for 20 min at room temperature in a vial. Lastly, it was kept into a preheated oven of temperature 85°C for 48 hours. The solution obtained was filtered, and colorless plate-like crystals were obtained as illustrated in Figure 12 (Mallick et al., 2012).



(a)

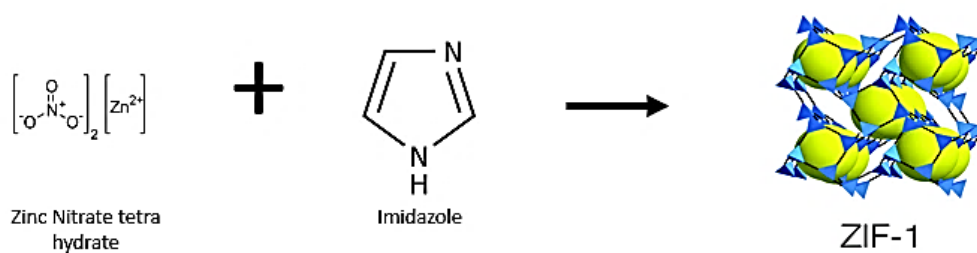


(b)

Figure 12: Synthesis of Ca-BTC; (a) Structural formula of Ca-BTC and (b) Ca-BTC crystals

3.2.5 ZIF-1

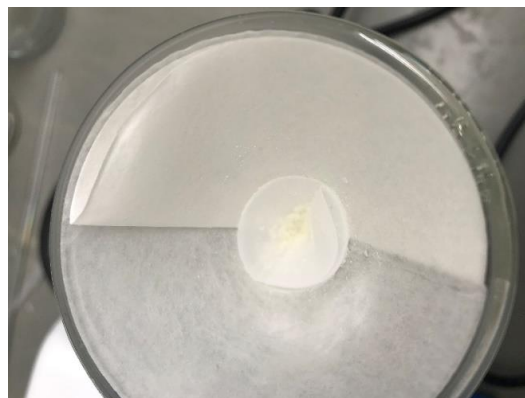
0.09 g of zinc nitrate tetrahydrate with chemical formula $\text{Zn}(\text{NO}_3)_2 \cdot 4\text{H}_2\text{O}$ and about 0.15 g of imidazole were combined to form a solid mixture and mixed within 72 ml DMF in a vial of 100 ml. The capped vial was put into the isothermal oven at the temperature of 85°C for about 36 hrs. After heating, the vial was cooled down at room temperature. ZIF-1 was formed in the form of colorless cubic crystals as in Figure 13, which were further washed with 3ml of DMF, 3 times per day for 2 days, and with ethanol for one day. Finally, it was dried in air for 10 mins and stored (Park et al., 2006).



(a)



(b)

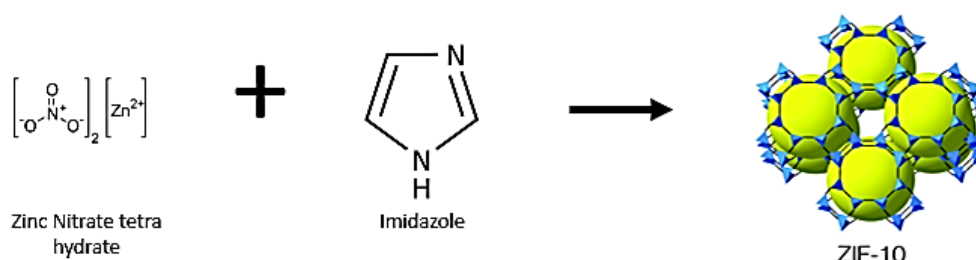


(c)

Figure 13: Chemical synthesis of ZIF-1; (a) Structural formula of ZIF-1, (b) ZIF-1 stick to the bottle walls and (c) Synthesized ZIF-1

3.2.6 ZIF-10

The solid mixture containing 0.020 g zinc nitrate tetrahydrate $\text{Zn}(\text{NO}_3)_2 \cdot 4\text{H}_2\text{O}$ and (0.030 g) imidazole was mixed with 3 mL DMF in a vial of 10-mL. The vial was capped and heated at 85°C for 48 hours in an isothermal oven. The vial was then set for cooling at room temperature. The MOF, named ZIF-10, was formulated along the wall and at the bottom of the vial as in Figure 14 (Park et al., 2006).



(a)



(b)

Figure 14: Synthesis of ZIF-10; (a) Structural formula of ZIF-10 and (b) ZIF-10 crystals stick to the wall

3.3 Instrumentation

3.3.1 X-Ray Diffraction

The crystallinity of the MOFs synthesized was confirmed using XRD. The atoms, molecules, or ions in different crystalline materials were organized regularly, called as the fingerprint of the material. The diffraction occurs when the X-Rays were dispersed through a regular array of atoms within the order of the long-range. Sample dispersed X-rays obstruct each other, either destructively or constructively. The detectors read the signals only at the angles of interference. When the sample scatters incident beams from its different planes, resultantly, diffracted X-Rays will take several optical wave lengths for traveling.

An XPert3 powder X-ray Diffractometer from Malvern Analytical, as shown in Figure 15, was used for the study of the crystallinity of different MOFs synthesized. The XRD scans with “ 2θ ” (it is defined as the angle between the incident beam and the diffracted beam from the sample) in range of 0 - 60°, scan speed of 0.02° per second, 40kV voltage, 20A intensity and 1.5406 Å Cu K α radiation. The graph obtained from the XRD was plotted between the angle of diffraction 2θ along x-axis versus X-ray intensity along the y-axis.



Figure 15: XRD Machine

3.3.2 Scanning Electron Microscope (SEM)

This microscope works on the principle of electron beams that scans the sample surface and produces an image. It is used to get the details regarding the surface topography and composition of the sample. The images are developed when the electrons from SEM collide with atoms of the sample generating diverse signals containing the info regarding sample morphology. The beam of an electron is passed through a raster scan pattern where its position is mixed with a perceived signal to generate an image of the object. For the characterization of synthesized MOFs and understanding the porous texture, the SEM used in the project was manufactured by JEOL, Japan, as shown in Figure 16.

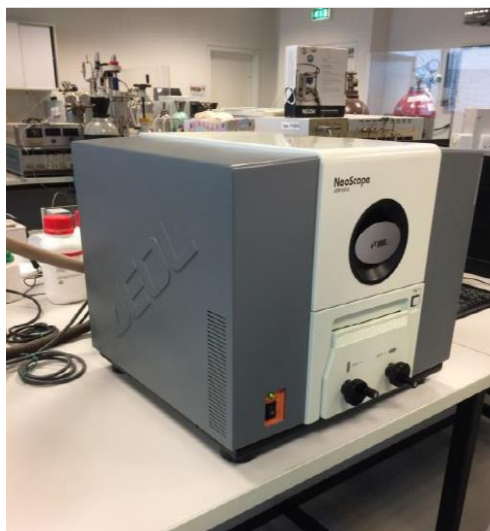


Figure 16: Scanning Electron Microscope

3.3.3 Thermogravimetric Analysis (TGA)

TGA determines the change in mass of the sample as the function of time or temperatures. For quality control and assurance, it is considered as a reliable tool for studying various processes accompanied by mass changes. The TGA, used for analysis was TGA Q50 V20.10 Build 36. The gas flow used for TGA was nitrogen. For each MOFs, it was run at the rate of 20°C per minute from the range of 25°C to 800°C for studying the stability and degradation temperature.

3.3.4 Nitrogen Adsorption Setup

For the nitrogen adsorption testing of synthesized MOFs, a Micromeritics ASAP known as accelerated surface area and porosimeter analyzer, 2010, was utilized. It works on the physical adsorption principle to get desorption and adsorption isotherms. It provides the information about porosity and surface area of the sample. The

applications of ASAP are in adsorption, catalysis, and characterization of porous materials. The results obtained from this setup was:

- Pore size, pore volume distributions, and surface area analyses.
- Langmuir surface areas and Brunauer–Emmett–Teller (BET) can be calculated.

3.3.4.1 System Description

The ASAP 2010 system comprise of a control module like a computer, an analyzer, which allows to enter report and analysis selections, and an interface controller that operates the analyses. It has one analysis and two sample ports. Both the degas and analysis system has inline cold traps that are placed in between the vacuum pump and manifold. The Psat (saturation pressure) tube is placed near the sample analysis port.



Figure 17: Nitrogen Adsorption Experimental Setup

The operation of a vacuum system, heating mantles, and degas valve is performed on a control panel. Liquid nitrogen dewar is kept on the elevator that operates

automatically while running the experiments. Considering the safety, a sliding shield is provided in front of the system. ASAP 2010 analysis can be done only by using compressed gases such as argon, helium, nitrogen and carbon dioxide with pressure set not more than 30 psi. In the case of MOFs characterization, the nitrogen gas was used as inert gas. Two independent stage mechanical vacuum pumps were used. One for degas and other for analysis. The system has two degas ports used for preparing the sample. The analysis part has one sample port and one saturation pressure tube. The whole setup is illustrated in Figure 17.

3.3.5 Gas Chromatography Setup

Gas Chromatography (GC) is generally used for testing the quantitative and qualitative measurements of mixtures of volatile substances. It is used for analysis and separation of multi-component mixtures such as gases, essential oils, hydrocarbons, and solvents (Yusuf et al., 2014). The GC can quantitatively ascertain the materials present at deficient concentrations such as forensic work, pollution studies, and general trace analysis.

An experimental setup was designed and constructed using Shimadzu 2014 GC. The GC was modified to allow for the testing of the adsorption properties of methane gas in MOF and separation of gas. It consists of advanced flow controller (AFC) technology, that has higher-level repeatability of peak area and retention time. It has sixteen 24-volt relays and seven heated zones. The detector used in this GC 2014 system is a thermal conductivity detector (TCD), which is ultimate for measurements of packed columns retaining the semi-diffusion cell design. The system has a Liquid

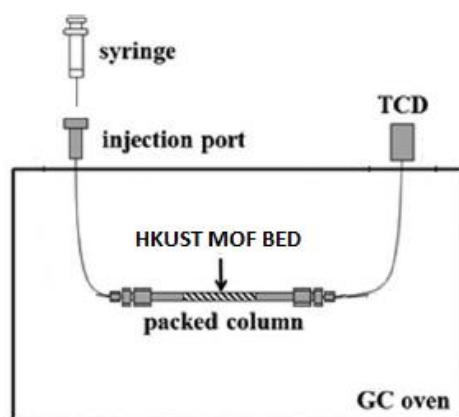
Crystal Display (LCD), which shows the parameters and current readings while running the experiment. The GC used for running experiments is shown in Figure 18.



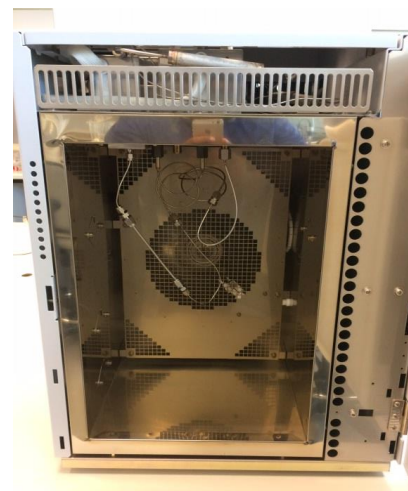
Figure 18: Gas Chromatography Shimadzu GC-2014

A graphical representation of the GC experimental apparatus with some modifications for testing methane gas adsorption in the lab is shown in Figure 19. The apparatus comprised of gas chromatograph model (Schimadzu GC-2014) along with standard column (GC) substituted by a 1/8th inches tube made up of stainless steel of 12-cm long and 2.1-mm ID dimensions. The HKUST-1 (metal-organic framework) was packed in the column and retained by plugs of glass wool. MOF of 0.08 g, generated approximately 4cm bed length, was packed in the column. The sample column inlet contained one port for injection, which allowed injecting the methane gas using a gas-tight syringe, as shown in Figure 20. Before merging at the inlet of the packed column, separate streams of Helium Airgas (UHP grade) were connected to the injection port. The total carrier gas flow rate within the column was stabilized at 10 mL/min in all

experiments. The concentrations of the effluent were checked using a thermal conductivity detector from the column. Due to the interaction between the organics in MOF and analytes, it also has high possibilities of gas separations.



(a)



(b)

Figure 19: Gas chromatography setup; (a) Schematic of the experimental apparatus of GC for testing adsorption of MOFs and (b) Inside view of modified GC connected with packed column



Figure 20: Gas-tight syringe for injection

3.3.5.1 Column Packing

Stainless steel tube of a $1/8^{\text{th}}$ inch with 12 cm long and 2.1 mm ID was used as the column. The column was filled with 0.087 g of HKUST metal-organic framework,

which forms a bed length of 4 cm. The material was packed tightly by plugging the glass wool on both sides of the column, as shown in Figure 22, which was finally inserted and fixed with the gas chromatography set up for testing the adsorption of methane. While packing the MOF in the column, the vibrator, as shown in Figure 21, was used to ensure the sample is filling uniform, tight, and avoided the void spaces. A packing tool kit was used for more perfection, as shown in Figure 21.

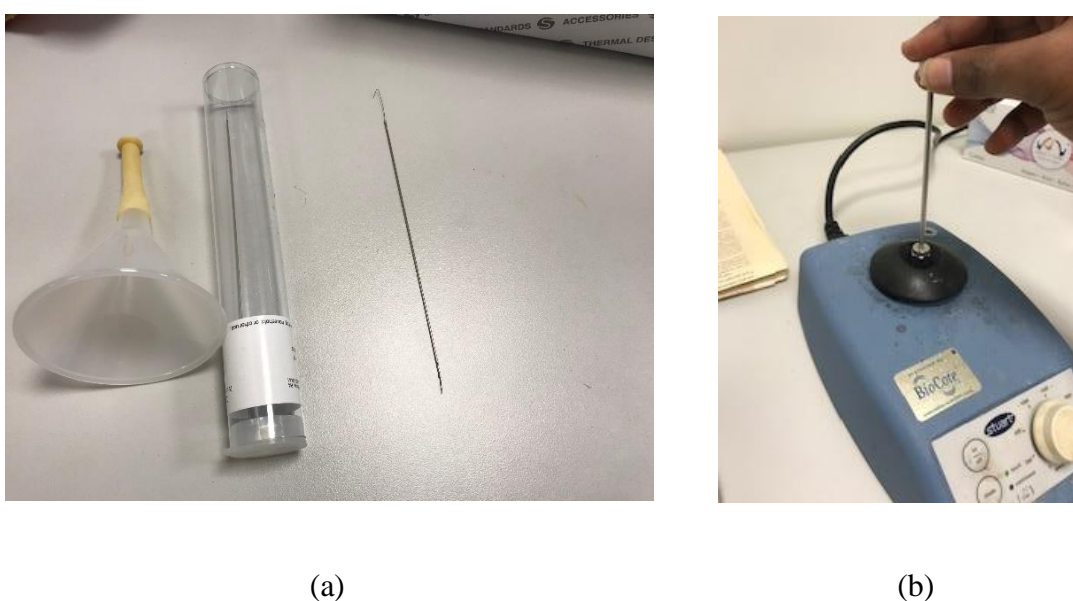


Figure 21: GC column packing apparatus; (a) Packing kit and (b) Vibrator used for packing MOF



Figure 22: Column packed with MOF and glass wool

3.3.5.2 Methane gas filling

A procedure was made for methane gas filling into the syringe for injecting to the GC. Firstly, the gas was filled into a balloon from the gas cylinder directly at very low pressure. Then from the balloon, it was filled into the syringe slowly, by injecting the syringe into the balloon inside the hood. The procedure followed for gas filling is shown in Figure 23. The needle size of the syringe was 22 Ga with point style 2.

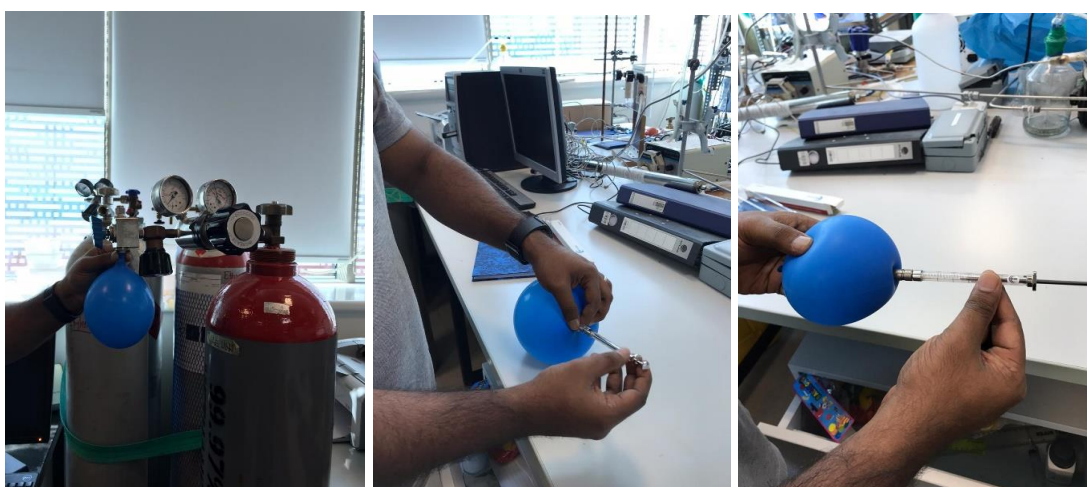


Figure 23: Methane gas filling into the syringe

3.3.6 Calorimeter Design and Setup

The process of adsorption occurs when molecules, ions, and atoms from any phase (solid, liquid, or gas) adhere and attach to the external surface creating a thin film of the adsorbate on the adsorbent surface. Usually, adsorption is modeled using isotherms, such as Freundlich and Langmuir isotherms.

In gas adsorption reactions, a reaction calorimeter and gas calorimeters are the best to be used for getting accurate experimental results about the reaction. In contrast, the reaction calorimeter can offer simultaneous monitoring of a variety of data that are in

control of the adsorption process. The chemical reactions are initiated within an insulated container in case of reaction calorimeters. Generated reaction heats are then measured. The calculation of total heat is done by integrating the flow of heat versus time in the experiment. Besides, different parameters can be used to study the characteristics of mass and heat transfer of the gas system, which can be provided from the gas adsorption studies using calorimeters, such as the gas solubility, enthalpy of adsorption, rate of gas adsorption, gas phase pressure in the tank, heat generation rate, etc. Tian Calvet calorimeter was used in this project to study the heat of adsorption in MOFs.

Tian Calvet calorimeters are used to quantify adsorption isosteric heats from a mixture of different gaseous and the reaction occurring on porous solid surfaces with instantaneous calculations of composition and loading (Dunne et al., 1996). Equilibrium behavior and complete thermodynamic information of a binary mixture can be obtained from collective measurements at a distinct reference temperature. The constituents of a binary mixture are treated interchangeably to determine the individual isosteric heats evolved from two amounts successively. The calorimeter cells designed to support the handling of samples under controlled environmental conditions. It allows studying of treated samples and materials exposed to any catalytic chemical reaction conditions. The optimal structure of pressure swing units of adsorption for storing or separating the mixture of gases depends on data of experimental equilibria for selectivity and loading as temperature, composition, and pressure function. The information of adsorbed mixtures desired equilibrium is the composition or pressure of the gaseous phase upon the adsorbent for assumed loading, also the generated heat for differential enhancements in the loading.

The main components of the calorimeter designed were calorimeter panel, gas inlet, crossover ball valve, pressure transducers, dosing loop, leak valve (between dosing loop and sample cell), sample cell, thermopiles, heat sink, multi-data logger, and pump. The calorimeter sketch and parts required to manufacture are illustrated in Figure 24 and Table 2. The energy flows from the sensor towards the sink where heat flux is calculated by way of time function. The total heat can be collected if the heat flux is integrated.

The sample cell is placed into a calorimetric cell. Thermopiles surround the four sides of the cell in order to collect the heat from all directions during adsorption. The two functions of thermopiles are to transfer the heat and generate signals for the heat produced by the adsorption. Two main processes consume the heat; one is an increase of the temperature of the sample cell and the other when heat flow through the thermopile, due to the temperature gradient between the cell and surrounding block.

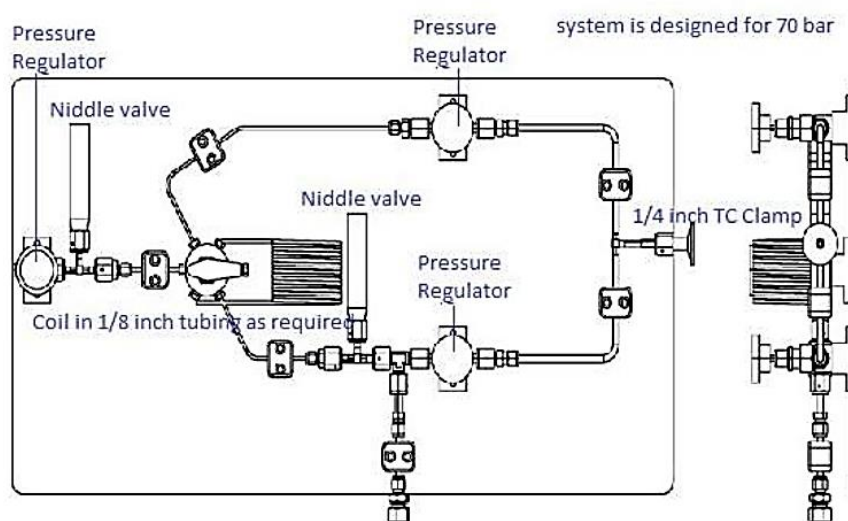


Figure 24: Calorimeter sketch

Table 2: Parts required for building the calorimeter

Item no	Description	Qty
1	Cross over valve	1
2	Tube fitting connector	5
3	T-Connector	2
4	Needle valve	3
5	1/4 th inch micro-Fit TEE	1
6	Union TEE	1
7	SS-T2	4
8	SS-T4	3
9	304-SI	3
10	Panel MS powder coated	1
11	T-joints	3
12	Pressure control valve	2
13	Gasket	12

3.3.6.1 Experimental Procedure

- In the beginning of experiment, the whole setup was evacuated using the vacuum pump for removing the impurities which may stick to the tubing.
- After completely evacuating, the dosing loop was filled with methane gas to the required pressure, and the valve was closed.
- Both sample and calorimetric cells owe the same initial temperature. Whereas, the pressure in the dosing loop would be greater than the pressure in the sample cell.
- Upon opening of the valve, an increase of gas (adsorbate) spreads into the sample cell from the dosing cell, and a part of the adsorbate adsorbs to the sample.

- In the dosing loop, gas temperature decreased due to expansion. On the contrary to this, in the sample cell, the temperature increased because of the compression of incoming gas.
- The sample temperature increased slightly because of the heat generated by the adsorption process.
- The energy ultimately flows through the sensor towards the sink, and as time functions, the flux was measured. The integration of the flux heads to the total collected heat.
- Repeated the same procedure mentioned above by dosing another quantity of gas to the sample cell from the loop, which resulted in a further increase of pressure in the sample cell, and corresponding energy flow was calculated.

3.3.6.2 Calorimetric cell

The calorimetric cell was decided to construct with Aluminum material because of its high thermal conductivity. The heat of adsorption generated from the sample in the sample cell during reaction need to be collected without any loss, which can be achieved by using the aluminum block. The dimensions of the aluminum square block were calculated using the Biot number (Bi). Bi number is a dimensionless quantity that establishes whether the temperature inside the material varies concerning space or not (Xu et al., 2012). If the Bi number is much smaller than 1 (in order of magnitude), then it is considered uniform temperature inside the body, and if it is larger than one, non-uniform temperature distribution is considered. As uniform temperature distribution is required, the length was calculated according to small Bi number, 0.01. The air had

been used as the convective fluid. The heat transfer coefficient of air was 10-100 W/m²K.

$$Bi = \frac{h * L}{k}$$

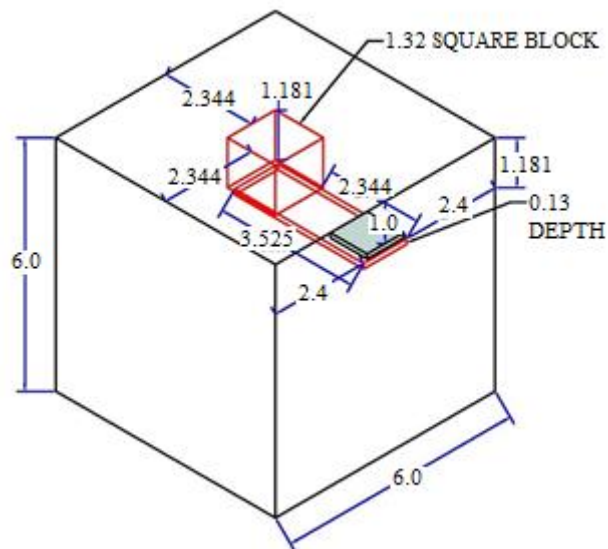
h – Convective heat transfer coefficient of air = 10 W/m²K

L- Characteristic length, defined as the ratio of the volume of the body to the surface area of the body

k- Thermal conductivity of Aluminum = 205 W/m.K

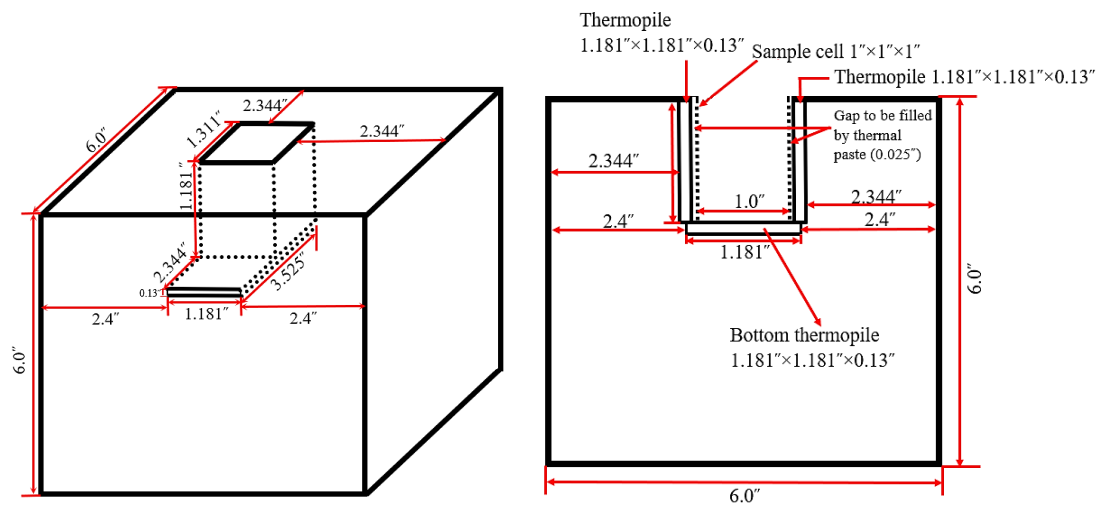
$$L = \frac{0.01 * 205 \text{ W/m.K}}{10 \text{ W/m}^2\text{K}} = 0.205\text{m} = 8 \text{ inches}$$

As per the above calculation, the aluminum block sketch was drawn for constructing with the dimensions calculated, as shown in Figure 25.

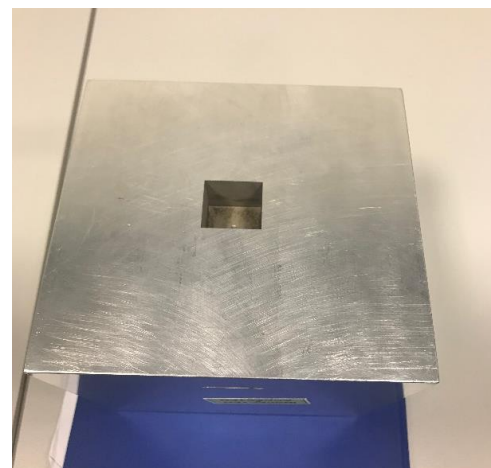
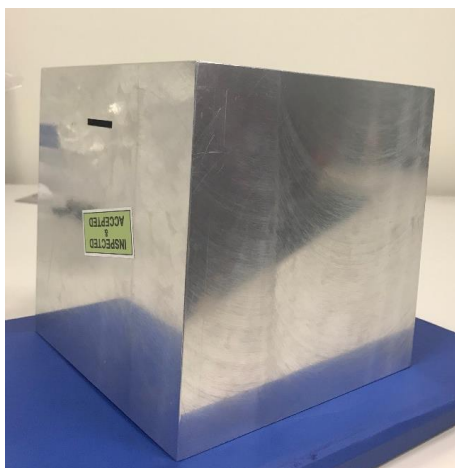


(a)

Figure 25: Construction of calorimetric cell; (a) AutoCAD sketch view of the block, (b) Overview and side view of the block with dimensions, and (c) Constructed Aluminum block



(b)



(c)

Figure 25: Construction of calorimetric cell; (a) AutoCAD sketch view of the block, (b) Overview and side view of the block with dimensions, and (c) Constructed Aluminium block (Continued)

The block and the square pocket on it for placing the pyrex glass cell (sample cell) were manufactured by the process called EDS sparking. Electrical discharge machining (EDM), which also called spark machining, is a process of manufacturing the shape by using electrical discharges, which are called sparks. The material was detached from

m the workpiece by a series of rapidly recurring discharges of the current between two electrodes isolated by a dielectric liquid and introduced to an electric voltage. The five sides of the square pocket in the calorimetric cell were to be covered by thermopiles to collect the heat released during adsorption. Therefore, the required five thermopiles are ordered from Green Teg Company, Switzerland. The information received from the thermopiles would be sent to the multi-data logger. The multi-data logger is the device used to store the data over time. The data logger and thermal paste needed for the calorimetric cells were also being ordered from the same company. The dimensions of thermopiles are $30 \text{ mm} \times 30 \text{ mm} \times 3.3 \text{ mm}$. In order to avoid any free space between the thermopiles and pyrex glass cell for accurate results, the thermal pads of thickness 0.5 mm (from Arctic company) were used, as shown in Figure 27. The thermal conductivity of thermopiles and thermal grease used in the calorimetric cell were 6 and 8 W/m.K , respectively. For a good heat transfer, further the thermal paste was applied on each side of the sample cell. It covers the top of sample cell also with the paste before running the experiment. Glass beads, as shown in Figure 26c, were spread above the sample placed in the glass cell to avoid the heat loss from the top side.

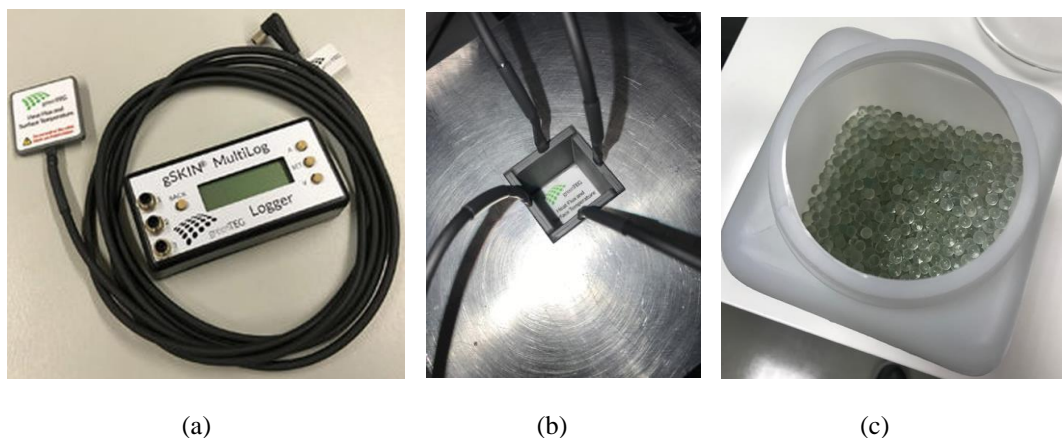


Figure 26: Thermodynamic assessment apparatus; (a) Thermopile and Multi data-logger, (b) Thermopiles fixed in the square pocket, (c) Glass beads

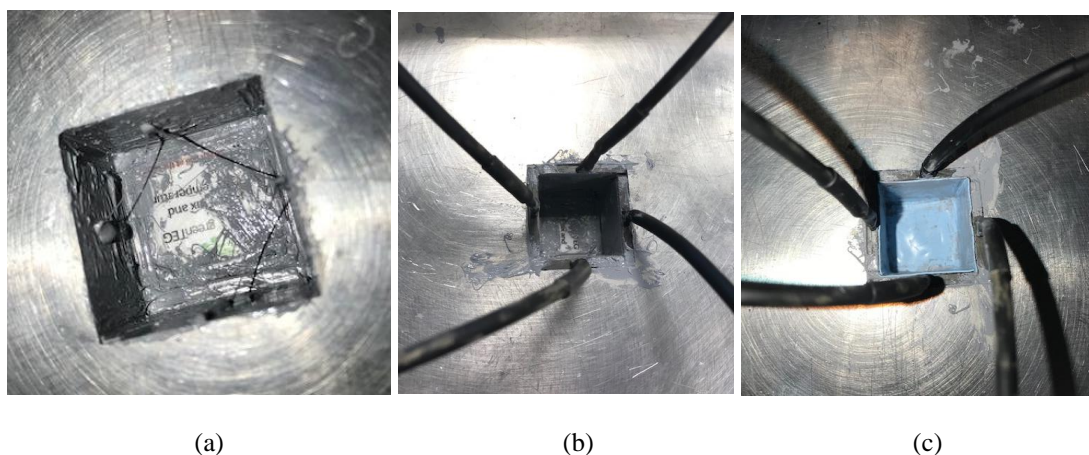


Figure 27: Fixing of thermopiles in calorimetric cell; (a) thermal paste, (b) thermopiles and (c) thermal pads

3.3.6.3 Pyrex Glass Cell

The material used for making sample glass cell was decided according to the thermal conductivity for capturing maximum heat released during adsorption without loss. The thermal conductivity of pyrex glass is $1.005 \text{ W/m} \cdot \text{K}$ at 25°C (Worgull, 2009). The Pyrex glass cell for the calorimeter experiments in which the MOFs for testing the heat of adsorption were placed is designed and sketched with dimensions, as shown in Figure 28. It was then manufactured from China with the help of Alfain lab equipment company. The glass cell was connected to the calorimeter with a rubber coke connector for avoiding the leakage of gas. Four sets of pyrex glass cells were manufactured to run the experiments.

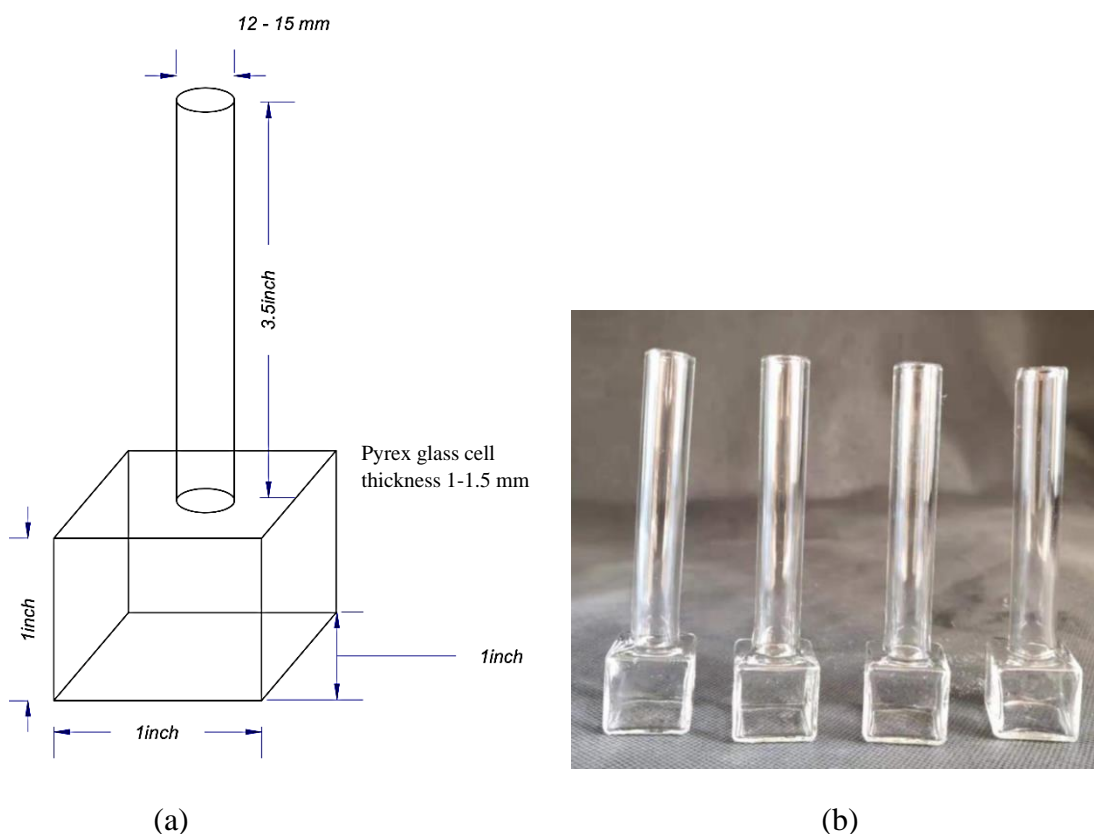


Figure 28: Sample cell preparation; (a) Sketched pyrex glass cell with dimension and (b) Manufactured cell

3.3.6.4 Vacuum Pump

For calorimeter experiments, a vacuum pump was required as described in the working procedure of calorimeter. The vacuum pump is used to evacuate the whole setup to remove the impurities, that get stick on the columns of the calorimeter. An oil vacuum pump with an ultimate pressure of 6.2×10^{-2} Pa was used in the setup. The specification of the pump is shown in Table 3. The pump was then welded with the pipeline, as shown in Figure 29, for connecting to the calorimeter.

Table 3: Specification of vacuum pump

Pumping speed (Hz)	50 (1500 rpm) (20.0 L/min) 60 (23.2 L/min) (0.39 L/s)
Type of Pump	Oil pump
Pressure (pa)	6.2×10^{-2}
Operating Temperature ($^{\circ}\text{C}$)	10 – 40
Oil Capacity	500-800 mL
Type of fluid	Gas
Company	ULVAC



Figure 29: The vacuum pump used for calorimeter setup

3.3.6.5 Calorimeter Stand

A calorimeter stand was designed according to the specification required for running the experiments. The calorimeter was fixed to the stand in such a way that it is easy to

run the experiment by the researcher. A plate was fixed on the stand for placing the aluminum block and data-logger. The bottom of the stand was designed to place the vacuum pump. Alfain Lab Equipments then manufactured the stand according to the sketch provided, as illustrated in Figure 30. After fixing the calorimeter to the stand, the 6-way valve and other connecting joints were fixed tightly to the calorimeter panel using glue for safety.

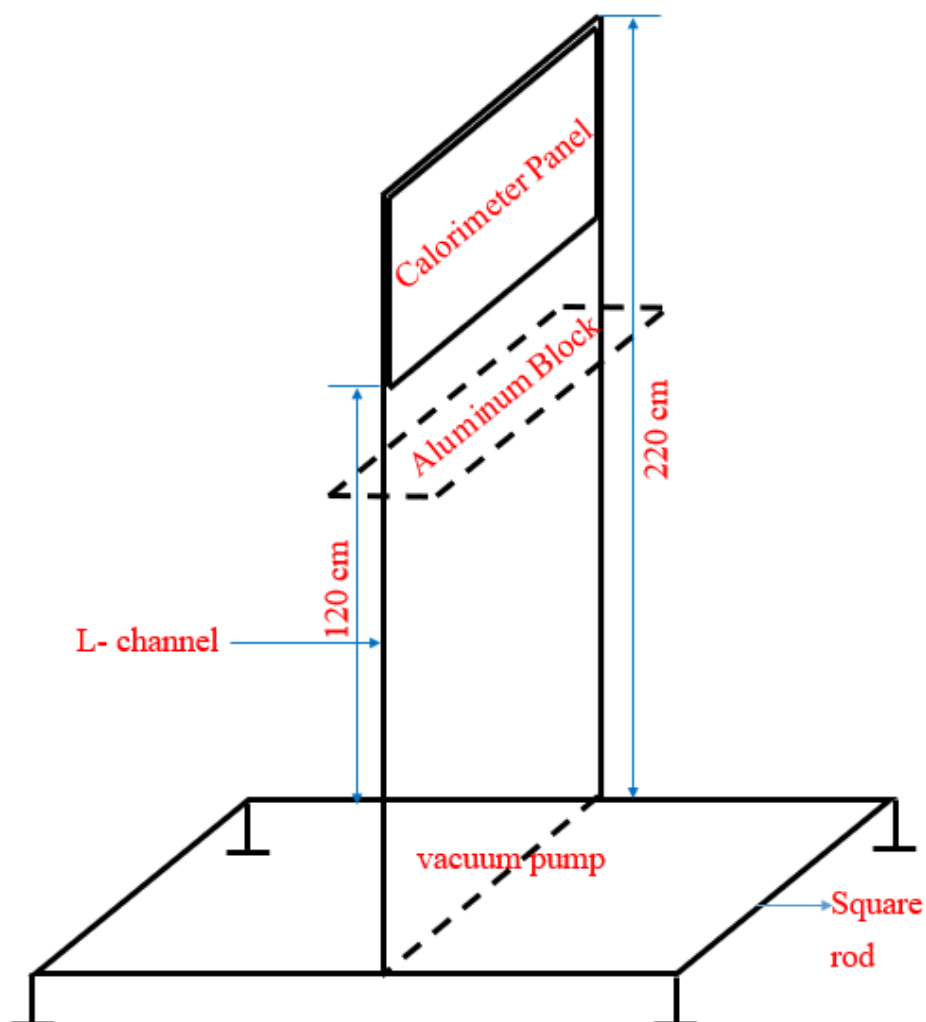


Figure 30: Sketch of calorimeter stand

3.3.6.6 Calorimeter Constructed

After compilation of all the above-mentioned parts, final calorimeter apparatus was constructed as shown in Figure 31. The figure is thoroughly labeled thoroughly with the help of numbering. Detail of each indicated part is tabulated in Table 4. As it can be clearly seen in the figure that the six-way valve and dosing loop are fixed on calorimetric panel supplied with methane gas cylinder. The building of the calorimetric was done in longitudinal way so that it is easy to run the experiments by the operator.

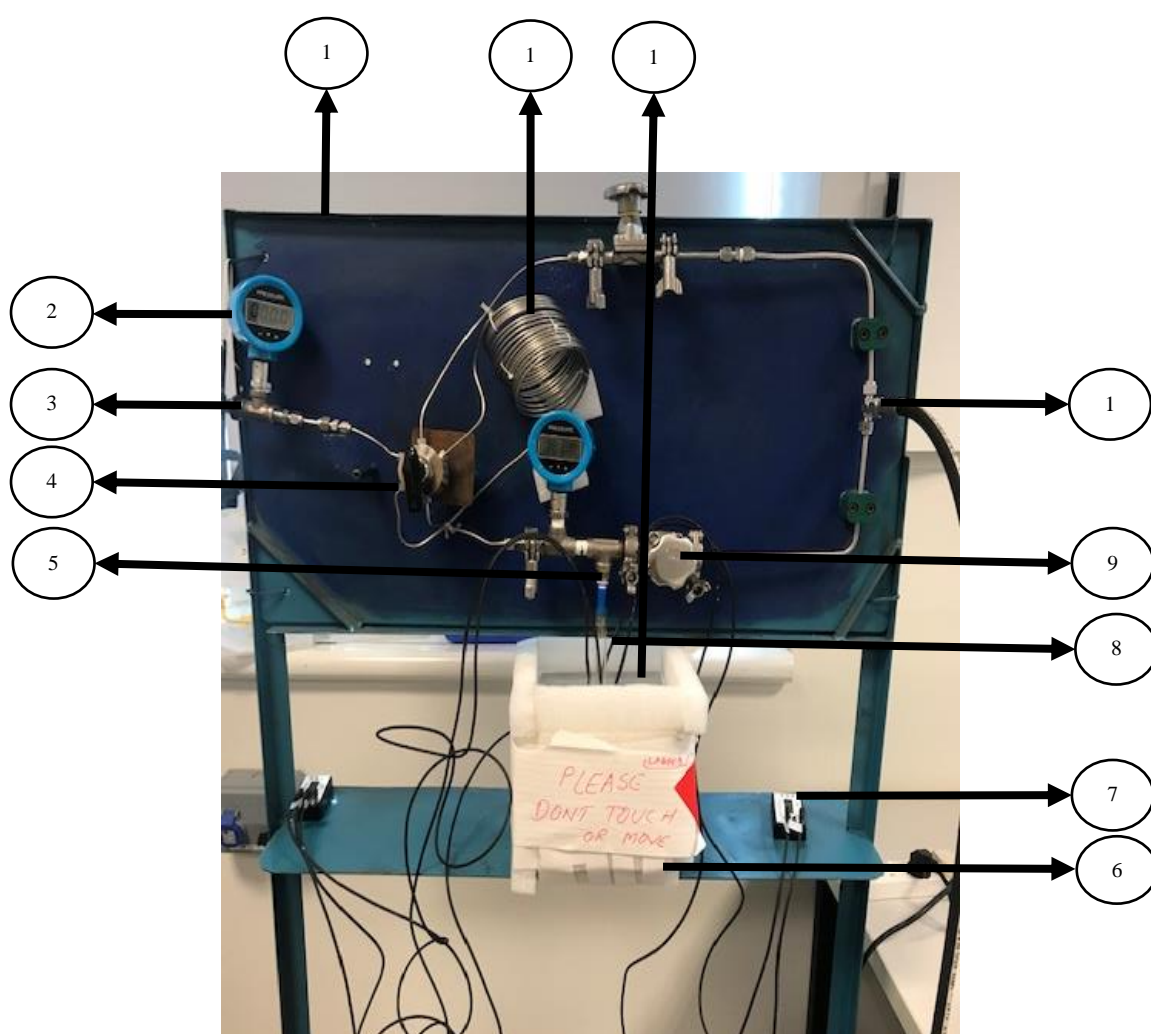


Figure 31: Calorimeter assembled and labeled

Table 4: Parts of calorimeter labeled as numbered in the figure

#	Components
1	Calorimeter Panel
2	Pressure Transducer for dosing loop
3	Inlet Gas (Methane)
4	Cross over (a 6-way valve)
5	Leak valve
6	Heat sink/Styrofoam cooler (Aluminum block, heat flux sensors, and cells)
7	Data logger connected to thermopiles
8	Pyrex glass cell (Sample cell)
9	Gate valve (Control the flow of gas)
10	Connection to the vacuum pump
11	Aluminum Block
12	Dosing loop

Chapter 4. Results and Discussion

4.1 Characterization of MOFs by XRD

Powder X-Ray Diffraction experiment is a significant technique used for studying the periodic structure of the crystalline materials like MOFs. For every experiment of MOFs, the detector was set at 2θ in range of (5-50°) with a step size of 0.02° per second, 40kV voltage, 20A intensity, and 1.5406 Å Cu K α radiation.

XRD patterns are known as the fingerprint of the material. Each MOF has unique XRD patterns. The experiment was run for the above synthesized six organic frameworks, and the pattern obtained from experiments was compared with the simulated pattern to study the structure purity, and crystallinity of MOF synthesized. The simulated patterns of the organic frameworks were developed using the Mercury Software version 4.0 (Macrae et al., 2020), which was measured using the CIF files of resolved structural models. Mercury is a software developed by Cambridge Crystallographic Data Centre, which has wide-ranging tools, and has been used for structure visualization, analysis, prediction, designing, and for the study of crystal packing.

The synthesized MOF-5, HKUST-1, Mg-MOF (NICS-6), ZIF-1, ZIF-10, and Ca-BTC polycrystalline samples were first examined by powder XRD. The patterns obtained from the experiments are shown in Figure 32. These patterns were further compared with the simulated pattern measured by the software. The experimental XRD pattern of the six samples in Figure 32 is consistent with the simulated one signifying the prepared samples are in its pure phase. The crystallographic data for the six samples are listed in Table 5.

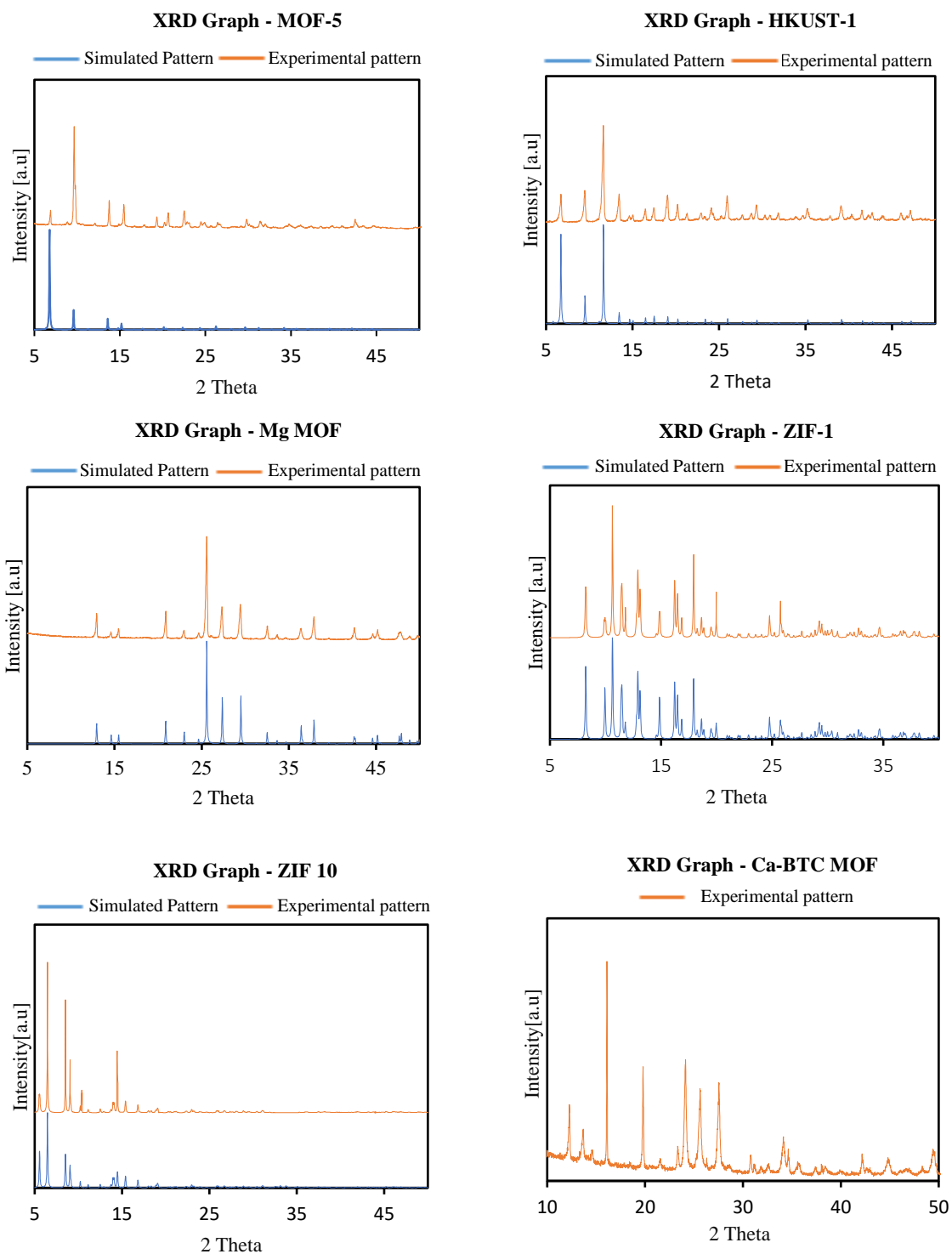


Figure 32: Simulated and experimental XRD patterns for the prepared MOF

Table 5. Crystallographic data for the synthesized MOFs¹

Compound Name	MOF-5	HKUST-1	NICS-6	Ca-BTC	ZIF-1	ZIF-10
Space Group	F m 3 m (225)	F m 3 m (225)	P1(2)	C 2 (5)	P 1 (1)	P 1 (1)
a(Å)	26.07	26.3034	7.7922	16.614	9.9949	21.6837
b(Å)	26.07	26.3034	7.7932	13.1785	15.3976	21.7123
c(Å)	26.07	26.3034	7.7929	15.630	15.18	21.6859
α (°)	90.0	90.0	66.135	90.0	89.9998	101.8203
β (°)	90.0	90.0	66.148	91.528	98.5469	101.8405
γ (°)	90.0	90.0	66.148	90	90.0003	126.4502
Cell volume(Å ³)	17718.4	18198.5	379.056	3420.93	2310.2	7312.73

¹ The data was obtained from mercury software version 4.0 (Macrae et al., 2020)

4.2 Nitrogen Adsorption

The specific surface area, volume distribution, and pore size was studied by using the gas adsorption method. The process was based on the adsorption of a gas on the adsorbate (sample). The gas used in this experiment is Nitrogen; hence the process is known as nitrogen adsorption, which is commonly used to measure the pore size and specific surface area of the sample. The plot obtained from this method is relative pressure (P/P₀) of nitrogen vs. the volume of sample adsorbed, where P and P₀ are the partial pressure and saturated pressure of nitrogen at temperature 77K. If the relative

pressure is between 0.05-0.4, then the adsorption is BET (Brunauer, Emmett, and teller), whereas if it above 0.4, then capillary condensation occurs (Fu et al., 2017). The nitrogen adsorption method is generally used for a sample with a pore size range of 2-50 nm. The specific surface area is defined as the amount of adsorbate adsorbed in one gram of the sample with unite m^2/g . Pore volume (PV) is the ratio of sample air volume to the total volume, and porosity explains the quality of the sample being porous. There are two different types of porous material classified as microporous and mesoporous.

In this project, the specific surface area and the pore volume of the synthesized MOF-5 and HKUST-1 were calculated from nitrogen adsorption isotherm data, obtained from adsorption equipment of Micro Active for Tristar. Initially, before running the test, the sample was evacuated thoroughly to remove all impurities at a temperature of 120°C for 5hrs. This process is known as degasification, as shown in Figure 33. The experiment is run in the range of relative pressure (P/P_0) 0-1 at 77K. The plots obtained for HKUST-1 in Figure 34 and MOF-5 is shown in Figure 35.



Figure 33: Degassing HKUST-1 before nitrogen adsorption experiment

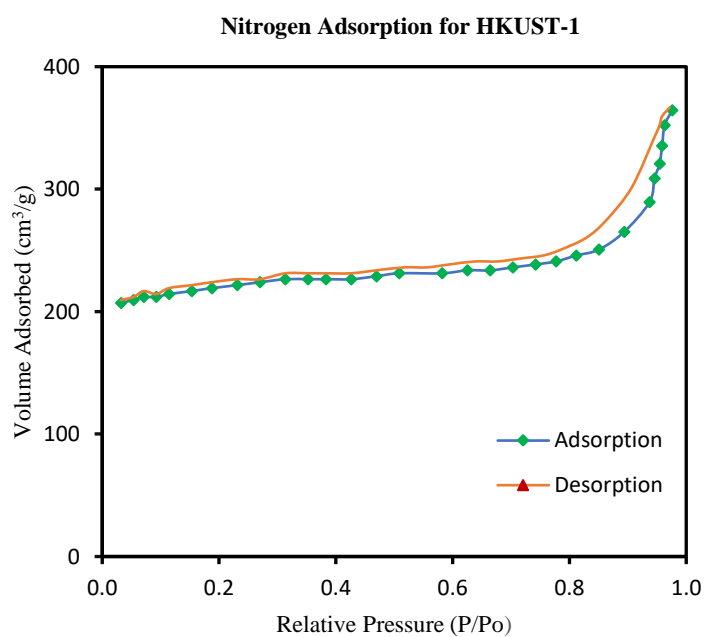


Figure 34: Nitrogen Adsorption-Desorption isotherms of HKUST-1 at 77 K

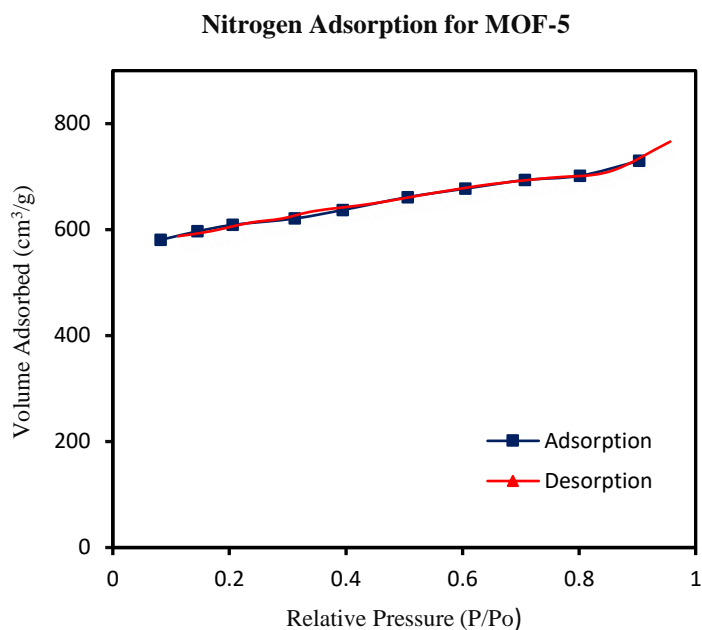


Figure 35: Nitrogen Adsorption-Desorption isotherms of MOF-5 at 77 K

The specific surface area calculated from the experiment for HKUST-1 and MOF-5 was 1092.96 and 2126.471 m²/g, respectively. The pore volume of the two MOFs was obtained as 0.37 and 0.42 cm³/g, respectively. The average pore diameter for MOF-5 by BET of adsorption and desorption was noted as 23.673 Å and 24.9066 Å, respectively. Figure 35 shows an initial steep increase in the volumetric uptake before 0.02 P/Po and then a quick saturation step at relatively low pressure, which signifies micropore filling and a hysteresis loop at relatively higher pressure, typically stemming from the mesopores. These results indicate the micropores and mesopores coexist in the prepared MOF-5 sample. Figure 34 initially at low relative pressure in range 0.01-0.5, it indicated the HKUST-1 is filling its monolayer. Then the nitrogen isotherm has an exponential increase in the range of 0.75-1 relative pressure, which is due to the sample particles were being accumulated and started filling the macropores

between the HKUST-1 particles. The average adsorption pore diameter of HKUST-1 was 16.0987 Å. In both MOFs, the specific surface area is determined by BET at the relative pressure range of 0.1-0.4 at 77K.

4.3 Scanning Electron Microscope

The morphology of the metal-organic frameworks was investigated using the SEM. The SEM used for this experiment was manufactured by JEOL, Japan. The surface of the MOFs and its durability can be explained by using this method. In this thesis, the morphology MOF-5, HKUST-1, Mg MOF(NICS-6), and Ca-BTC are studied. The SEM images for the above synthesized crystalline MOF samples are shown in Figure 37. Initially, the samples, before putting into SEM, need to make it conductive. Therefore, they were coated with a very thin layer of gold by the machine called a sputter coater. Further, it was placed to the specimen holder before viewed in the SEM, as shown in the Figure 36.



Figure 36: Sample prepared for analysis

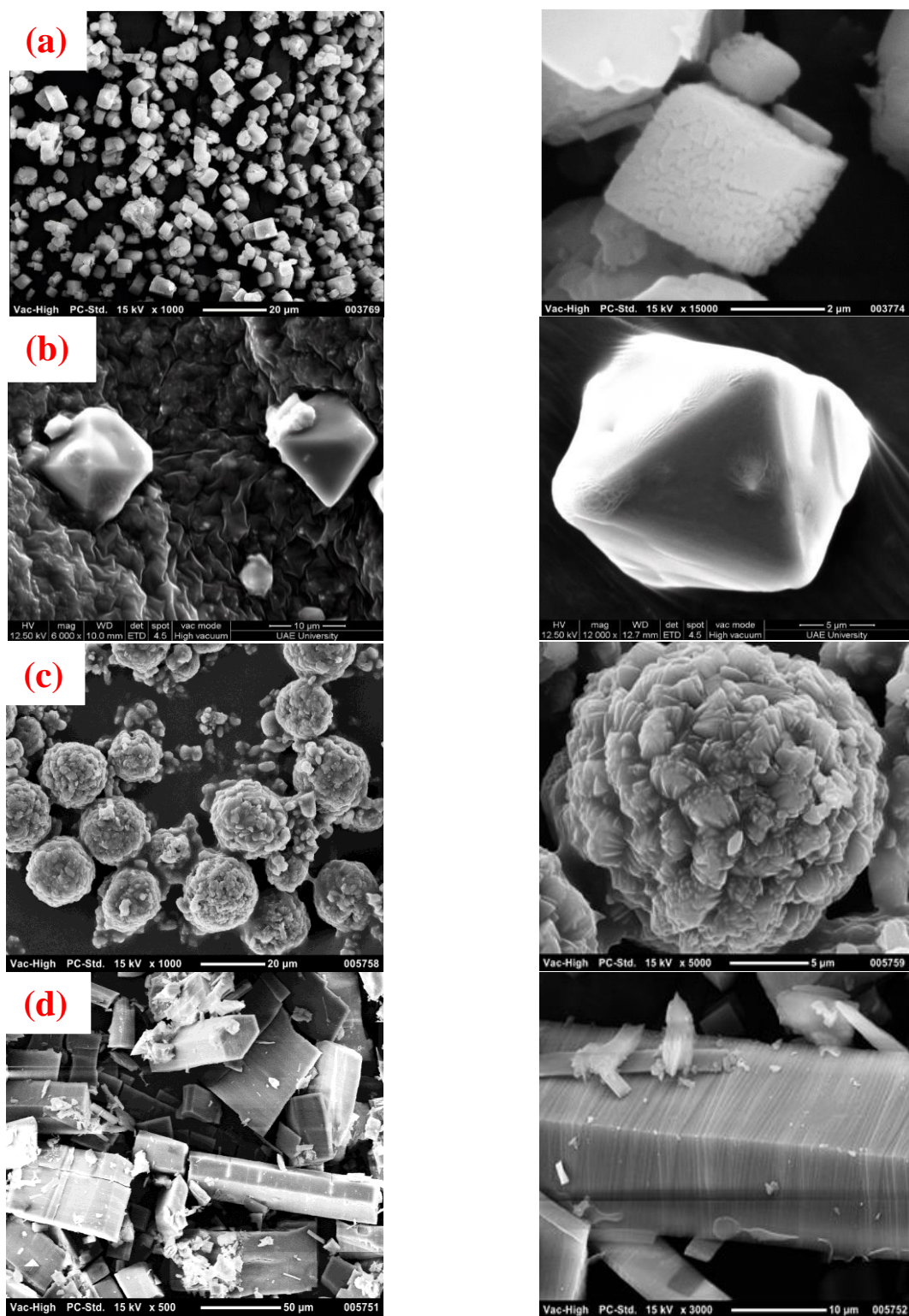


Figure 37: SEM images of different MOFs; (a) MOF-5, (b) HKUST-1, (c) Mg-MOF(NICS-6) and (d) Ca-BTC

In order to characterize the morphology and porous texture, the SEM images showed that each particle consists of intergrown cubic crystals. Figure 37(a) shows the MOF-5 image at two different magnification, which indicate the synthesized sample was highly crystalline and is having a cubic morphology with a particle size of around 10 μm . Representative images are shown in Figure 37(b) for the HKUST-1 organic framework synthesized by the solvothermal process. This MOF is blue colored, which further changes into dark blue after activating it at 120°C. It is composed of octahedral crystals having a smooth surface with the particle size in the range of 0.5 to 5 μm . In the case of Magnesium MOF, it was showing a collapsed image of particles without a clear view, so a small amount of dried powder of Mg-MOF was mixed with ethanol and sonicated to break into fragments in order to get a clear image by SEM. NICS-6 revealed a hollow spherical shape in the SEM view, as illustrated in Figure 37(c). When the image was zoomed in more into a single particle, it also has a flowered structure shape. At last, in the Ca-BTC framework, the images of the particle were aligned like a layered structure. The particles were zoomed-in closely in order to see the layered structure, as shown in Figure 37(d).

4.4 Thermogravimetric Analysis

In TGA, the sample was subjected to a certain controlled temperature for measuring the physical property of the substance as a function of temperature. This experiment revealed the degradation and stability of the material. Solid samples can only be analyzed using this technique. The TGA analysis was conducted for HKUST-1, MOF-5, and Mg-MOF, as shown in Figure 38.

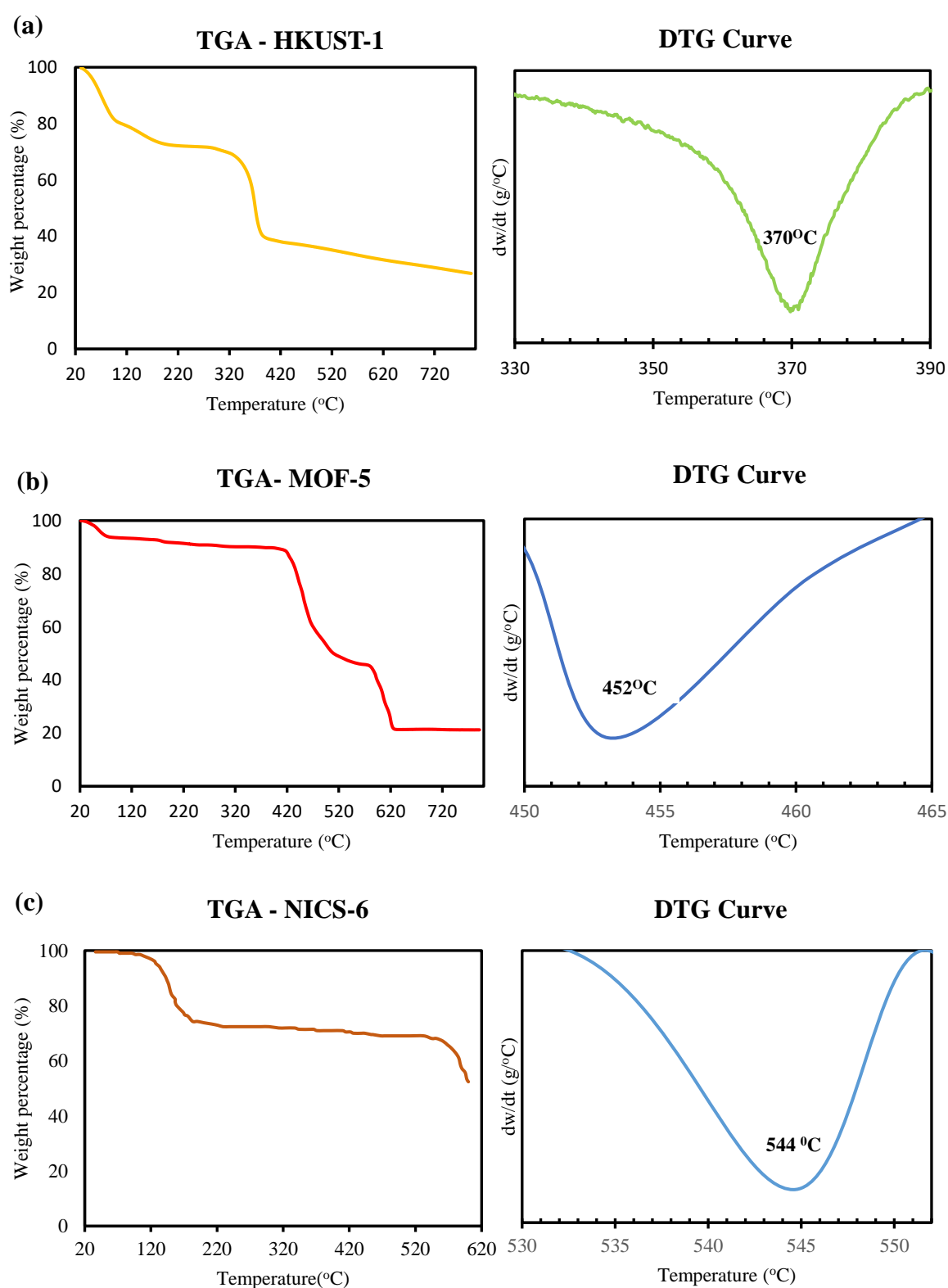


Figure 38: TGA and DTG curves of different MOFs; (a) HKUST-1, (b)MOF-5 and (c) NICS-6

As illustrated in Figure 38(a), two main decomposition steps have taken place in HKUST-1. Firstly, the weight loss of 23% was observed below 150°C, which is due to the evaporation of adsorbed molecules in the organic framework. A gradual small weight loss around 5% is due to the release of physisorbed and chemisorbed molecules within the surface and inside the pores of the framework. Finally, above 370°C the HKUST-1 structure was completely collapsed, and decomposition of the BTC ligands were occurred, resulting in an overall weight percent of 38. The remaining residue left was the copper oxide inside the framework. The degradation temperature was obtained by plotting between dw/dt vs. temperature, as shown in Figure 38(a), which indicate 370°C. In the case of MOF-5, the TGA curve, as shown in Figure 38(b), represents mainly two-step of weight loss. Initially, there was 8% of weight loss below 120°C, due to the evaporation and removal of water molecules and solvent DMF from the MOF-5 sample. An exponential weight loss of approximately 47% was followed above 425°C, which accounts due to the structural collapse of the framework. Around 543°C, the sample was completely decomposed. The degradation temperature is shown in Figure 38(b). The TGA curves of Mg-MOF, also known as NICS-6, is represented in Figure 38(c). In this MOF, it is noticeable a 23% of weight loss occurs around the temperature of 100-130°C, which is due to the evaporation of physically adsorbed water molecules and gases. After this temperature, it was highly stable up to 540°C. Out of these MOFs, magnesium MOF resulted in high stability temperature. The degradation temperature at which the BTC ligands began to be decomposed was obtained at 543°C, as illustrated in Figure 38(c). The high-temperature stability of this MOF is due to its dense structure(Mali et al., 2015).

4.5 Gas Chromatography Adsorption

4.5.1 Methane Gas Adsorption

From the literature reviews, out of the MOFs synthesized, it was known that one of the best MOF for adsorption of methane is HKUST-1 (Mahmoud et al., 2019; Tian et al., 2018b; Peng et al., 2013a). In order to study the adsorption properties of this MOF, an experimental setup was designed, as described in the previous section. The setup consists of gas chromatography (Schimadzu 2014), with the customized column of 1/8th inch stainless steel tube of 2.0 mm inner diameter and 12 cm in length. The column was packed with 0.087 g HKUST-1 which is approximately 4 cm length in the center, and the other both ends with 4 cm were filled with glass wool tightly, such that there is no dead space left in the column. Helium was used as the carrier gas, and the experiment was carried out at 1 bar and 298 K.

In these GC experiments, in order to get a good retention time, the amount of injecting methane should be in the range of 2-4 micromoles (Luo et al., 2014). As the concentration increases, the peak comes out earlier. For a good resolution peak, it needs to inject 0.05-0.1 ml (or micromoles) according to the calculations; if the injection of methane gas is in these ranges, then it is equivalent to 2-4 micromoles. Since methane acts like an ideal gas at STP, $n = 4$ micromoles, $P = 1 \text{ atm}$, $R = 0.0821 \text{ L.atm.K}^{-1}.\text{mol}^{-1}$, $T = 25^\circ\text{C} = 298 \text{ K}$, and $Z = 1$ (Luo et al., 2014).

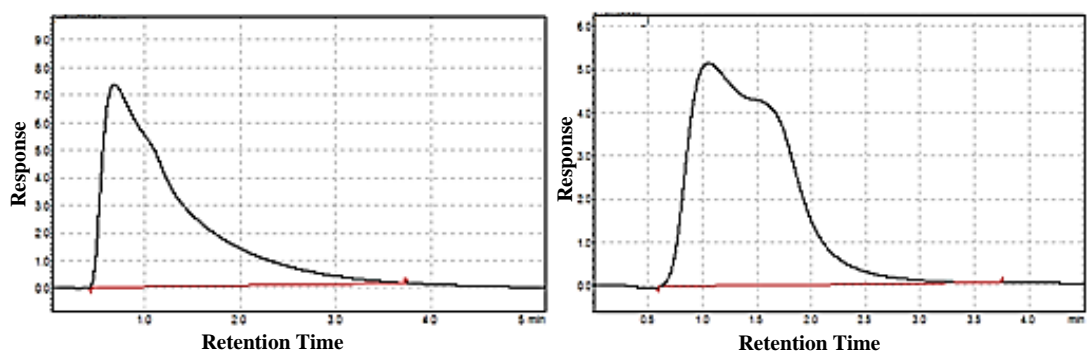
$$PV = nRT$$

$$V = \frac{nRT}{P} = \frac{4 * 10^{-6} * 0.0821 * 298}{1} = 9.786 \times 10^{-6} \text{ l} = 97.86 \mu\text{l}$$

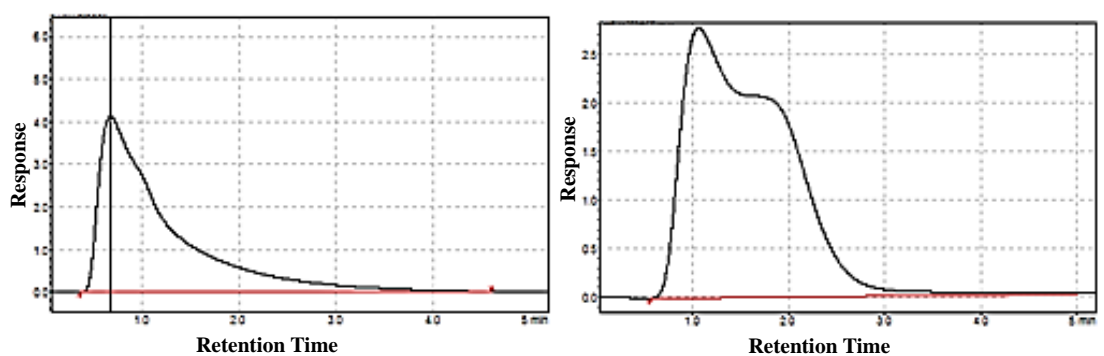
So, the GC experiments were conducted by injecting 100 microliters of methane gas at 1 bar, and the results obtained are discussed. Furthermore, it was compared with the results obtained for the injection rate, when increased up to 500 microliters. The other parametric values of the experiment are shown in Table 6. The graphs obtained from the GC at three different injecting volumes of methane for inert column and HKUST-1 packed column are illustrated in Figure 39.

Table 6: Parameter for Gas Chromatography

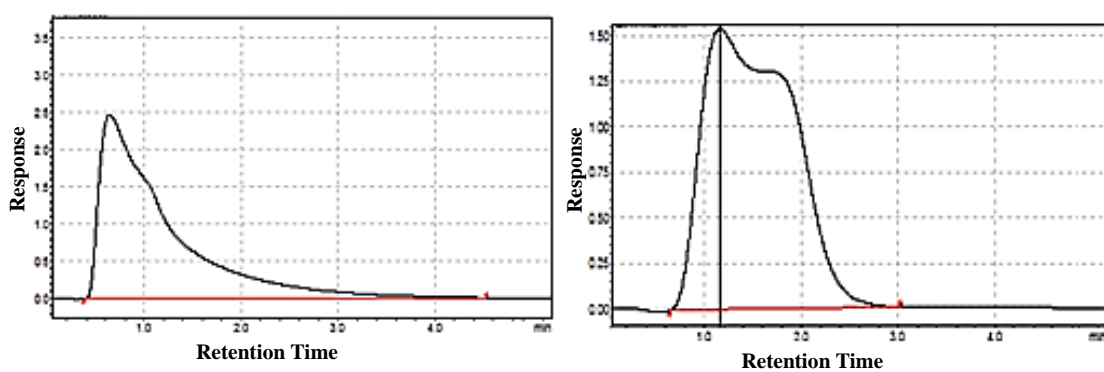
Parameters	Values
Inlet temperature	45 ⁰ C
Column Temperature	25 ⁰ C
Detector Temperature	200 ⁰ C
Flow Rate	10 ml/min
Injecting Volume (Methane Gas)	100-500 μ l
The pressure of the Helium Cylinder	2 kg/cm ²
Hold Time	40 minutes
Current	100 mA



(a)



(b)



(c)

Figure 39: GC graphs of inert column (left side) and HKUST-1 packed column (right side) for various injections of methane (a) 100 µl, (b) 300 µl and (c) 500 µl

The graphs obtained from GC for inert and MOF-packed columns were analyzed. The retention time for the inert column of different volume injections was around 0.665, whereas, for the packed column, it was found to be 1.125. Retention time is the time required for the injected methane to pass through the column until it reaches the detection. High retention time means that the solute interacts with the stationary phase in the column and takes time to come out.

The retention time was higher in the case of a packed column, which concludes that methane molecules interacted with the HKUST-1 packing in the column and got adsorbed. In the case of the packed column graph, the peaks are broader, which indicates the methane molecules take more time to come out compared to inert ones due to adsorption in the framework. The two peaks in the packed column plots indicated that methane is adsorbed to the MOF. The first peak indicates the methane molecules coming out once the MOF get fully saturated. The second peak is methane molecules, which are weakly adsorbed on the pores of the framework, which comes out after some time.

Similar results were observed at different injection volumes. The amount of methane moles adsorbed to the MOF was calculated using a linear calibration curve plotted for the inert column, as shown in Figure 40. The amount of methane adsorbed on the HKUST-1 MOF was obtained by using the area found from the curve in Figure 39 and volume measured from the calibration curve shown in Figure 40. Then the value is converted using the unit conversion. Finally, the calculated value was 0.0184 g/g of methane at 1 bar and 298 K.

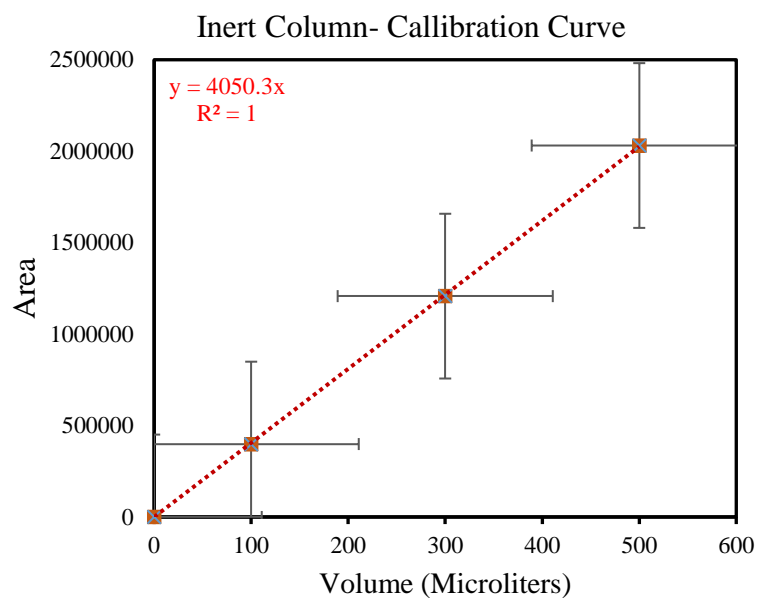


Figure 40: Calibration curve for inert column injections

4.5.2 Methane - Carbon dioxide Adsorption

The same experimental setup was used to test the adsorption property of a mixture of gases. MOFs had resulted in an excellent performance in the separation of gases. In this project, the adsorption property of methane-carbon dioxide mixture (90%, 10%) on HKUST-1 was tested and analyzed. The graphs obtained for this experiment is illustrated in Figure 41.

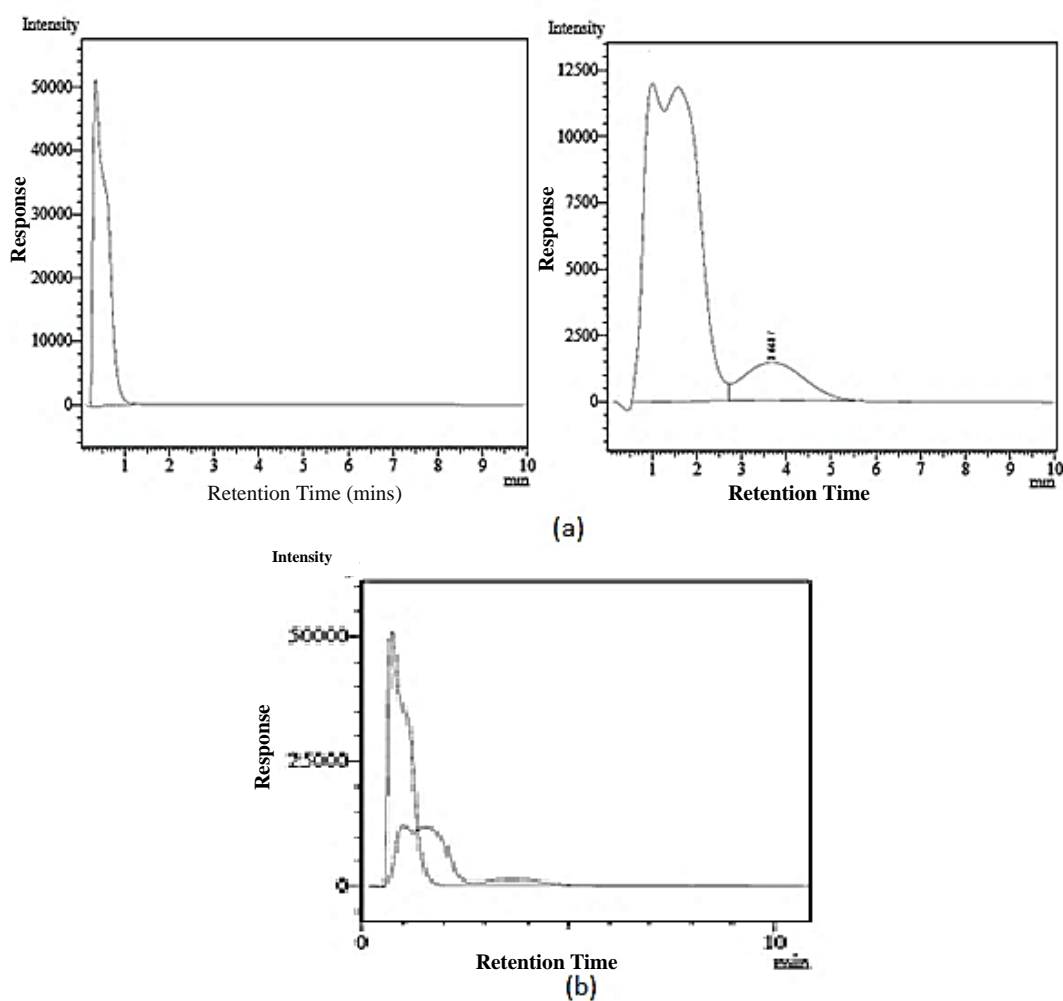


Figure 41: Analysis of gaseous mixture using GC; (a) GC graphs obtained for CH₄-CO₂ gaseous mixture for inert column (left side) and HKUST-1 packed column (right side) and (b) Comparison of the first two graphs

The experiment had run for both inert column, and MOF packed column for methane-carbon dioxide mixture of gases and analyzed. The parameter of the GC experiment is shown in Table 6. In the comparison of the packed and inert column area, there is a difference in both areas. The area is found to be less in case of a packed column, which explains the gaseous mixture injected to the column has not come completely out because it is adsorbed to the organic framework packing. Pulsed chromatography experiments on the MOF, as shown in Figure 41, illustrates that the first shoulder peak

is due to carbon dioxide with the lowest elution time. The second peak is due to methane, and the third peak belongs to carbon dioxide that adsorbed to MOF (Quartapelle Procopio et al., 2010).

The retention time for methane and adsorbed carbon oxide was 1.006 and 3.668, respectively. In Figure 41 (a, left side), the split occurred in between the first peak, which is due to weakly adsorbed methane molecules that further confirm that HKUST-1 MOF is adsorbing the methane weakly to its pore walls and then releasing it. Nevertheless, carbon dioxide was adsorbed stronger than methane, and it took more time to go through the column. The shape of the peaks in the packed column is wider than the inert column, which shows that the CH₄-CO₂ mixture is traveling through the MOF, and it is taking more time to pass due to adsorption.

4.6 Adsorption analysis using Calorimeter

The heat of adsorption for methane gas on the different metal-organic frameworks synthesized were calculated using the designed calorimeter as described in the instrumentation section. The adsorption isotherms were measured at 298 K. Separate measurements were made over an interval of 0-3 bar. The experiments were run three times in order to confirm the reproducibility of the results obtained from the calorimeter. Before running the experiments, the samples were activated by heating in a vacuum oven at 120°C and 10 mmtorr for 6 hours. One gram of each activated sample was weighed to carry out the calorimeter testing. It was noticed while activating the HKUST-1 sample; it changed its color from light turquoise blue color to darker, as shown in Figure 42. The activated samples are then filled to the pyrex glass cell at the height of 5 mm, which would be enough sample in the glass cell for methane to adsorb.

The adsorbent (sample) in the glass cell was then covered with a layer of glass chips for about 15 mm height, as shown in Figure 43. The glass chips were used for minimizing the heat loss from the top of the cell.

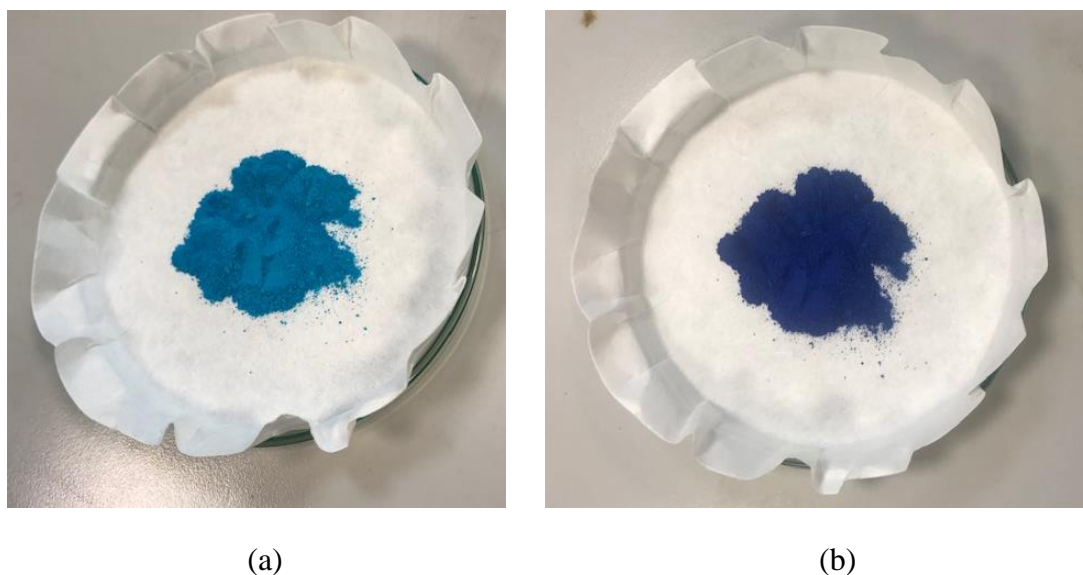


Figure 42: HKUST-1 activation; (a) before and (b) after at 120°C

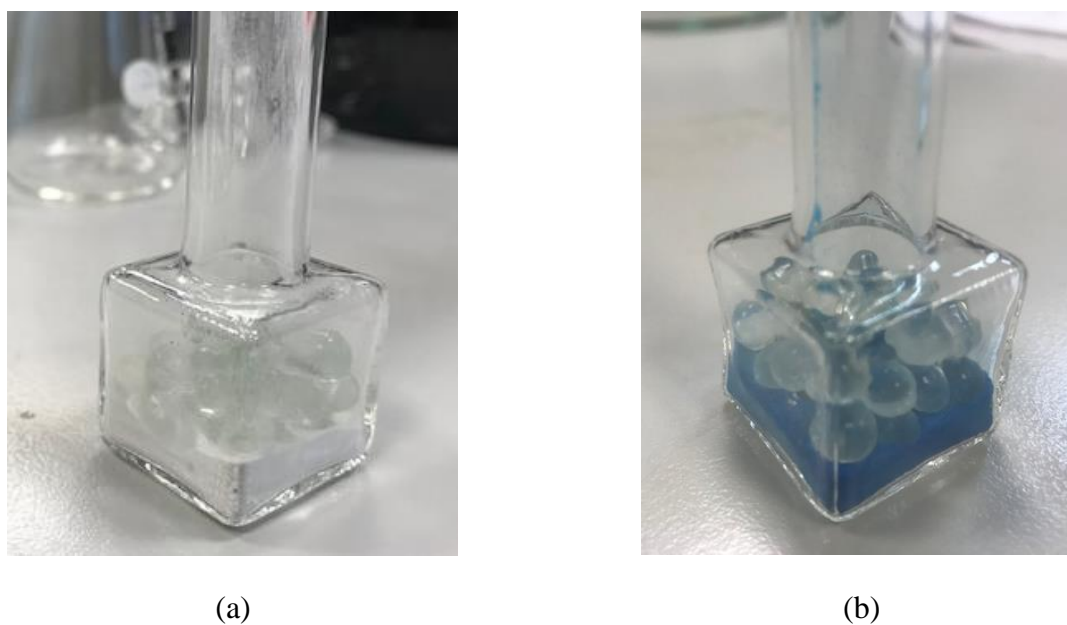


Figure 43: Pyrex glass cell packed with MOFs and glass chips; (a) NICS-6 and (b) HKUST-1

4.6.1 Spurious Heat

The spurious heat of compression was calculated by adding the dosage of gases into the sample cell without the adsorbent at different pressure. It was calculated because initially, the temperature of the dosing loop and sample cell were the same. However, while dosing the increment of gases into the cell, there will be a generation of heat due to compression. The thermopiles connected in the calorimeter measured the sensible heat released by the gas compressed when it cooled down to the normal temperature. This heat was subtracted from the heat of adsorption values obtained for the adsorbents.

The sample cell volume was calculated as 26.38 cm³ using the dimensions illustrated in Figure 28. The spurious heat of compression for the sample cell with dead space of the volume mentioned above is given by the linear correlation (García-Cuello et al., 2008).

$$Q_{sp} = a\Delta P$$

The graph obtained for spurious heat of compression using calorimeter is shown in Figure 44. The five thermopiles surrounding the sample cell individually collected the heat flux liberated due to compression of the gas dosed from the dosing loop. From this graph, the total heat flux was calculated by integrating the total area under the five curves. Further, another plot of total heat liberated vs. pressure difference was established, as shown in Figure 45. The 'a' value for the above equation was calculated from this plot as $a = 1.5356 \text{ J/bar}$, where ΔP is the pressure difference between the

sample cell and the dosing loop. The Qsp obtained at various pressure differences is tabulated in Table 7, presented in the following section.

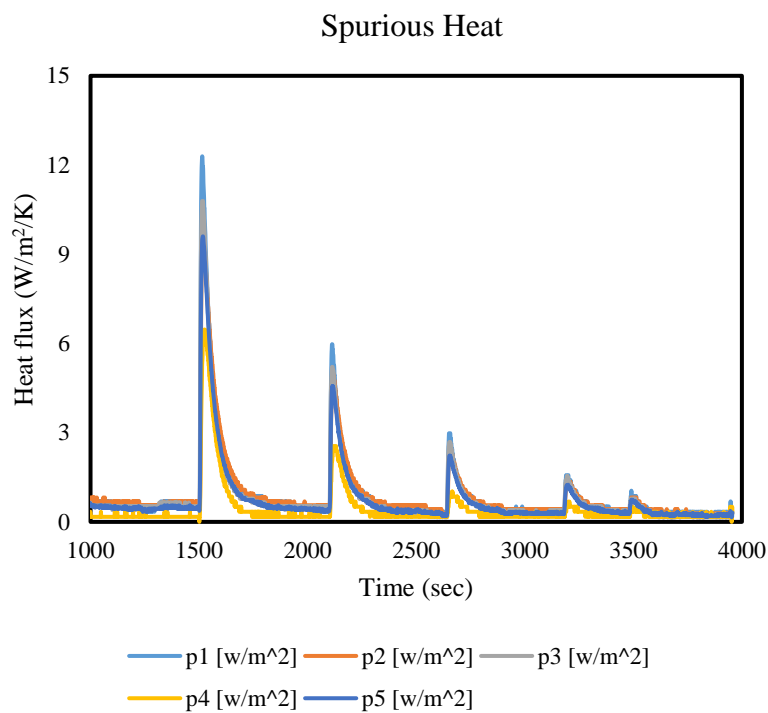


Figure 44: Heat Flux vs. Time for Spurious heat of compression

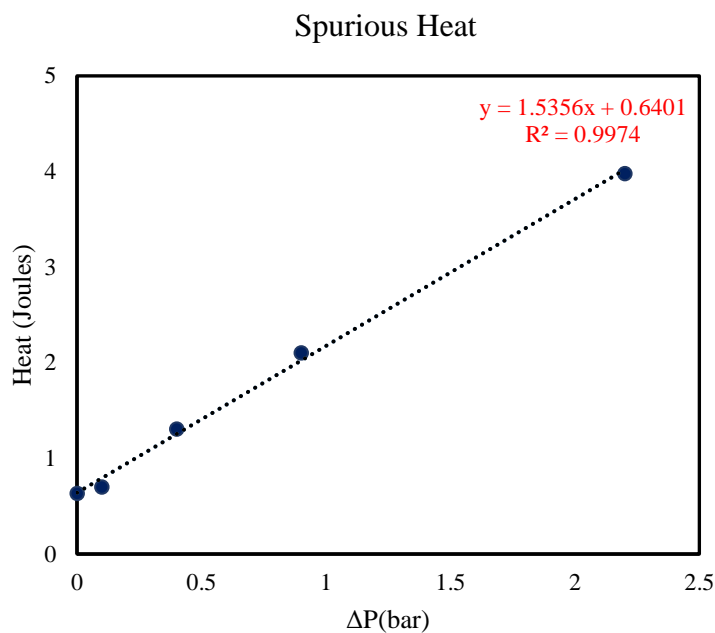
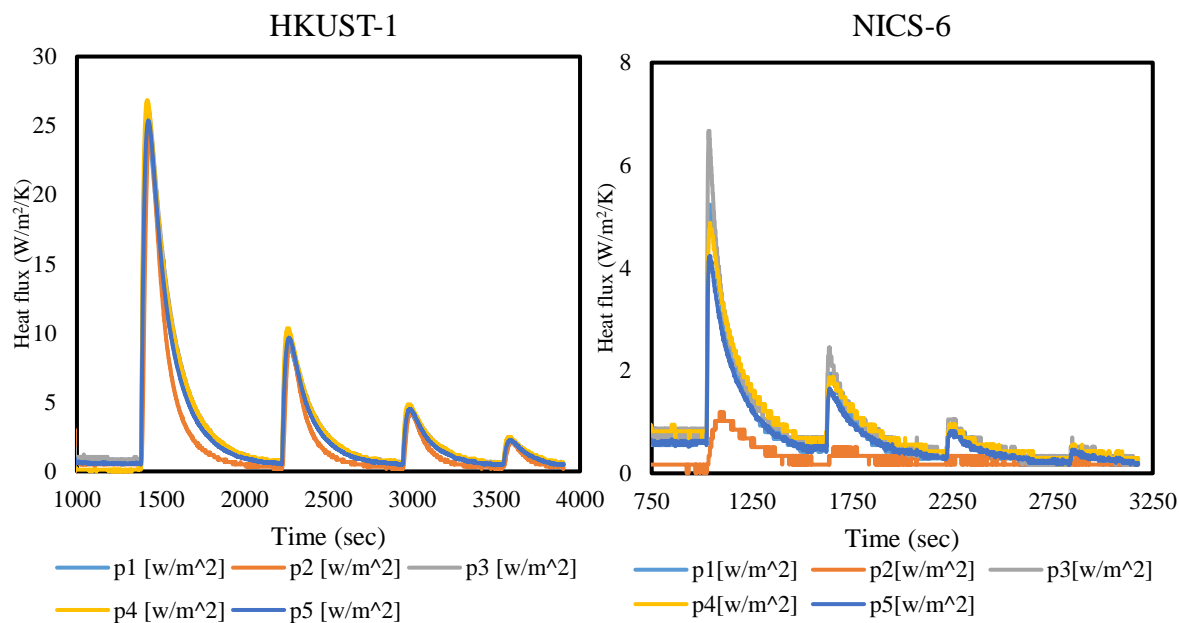


Figure 45: Linear correlation of spurious heat for gas dosage at different pressure

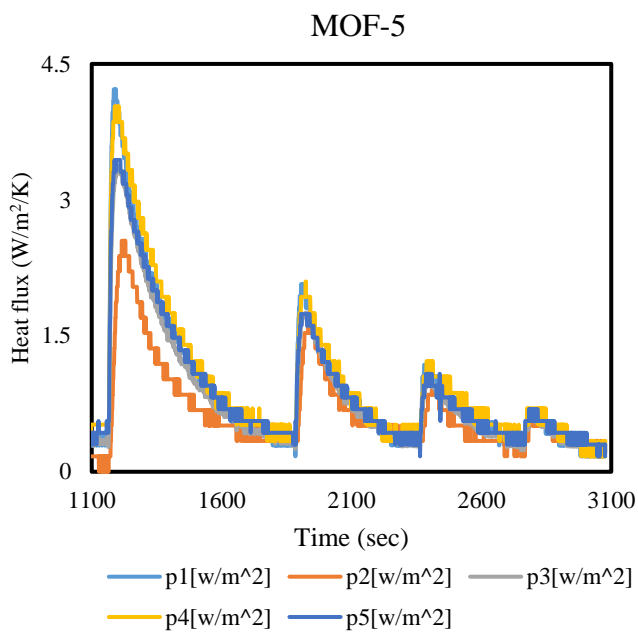
4.6.2 Heat of adsorption of MOFs using the calorimeter

The heat of adsorption (Q_{ad}) was measured for the three MOFs synthesized previously, HKUST-1, MOF-5, and NICS-6 using a calorimeter. The activated samples were placed in the pyrex glass cell along with the glass chips and connected to the calorimetric cell (Aluminum block) surrounded with five thermopiles. The heat flux obtained from each thermopile for various pressure difference was integrated to obtain the total heat liberated by adsorption. The heat thus obtained was subtracted from the heat of compression to obtain the Q_{ad} values for each MOFs. The pressure difference, along with the calculated heat of adsorption for each MOFs, are tabulated in Table 7. The plot of heat flux at each second with various pressure for different samples are shown in Figure 46. The experiments were carried out at room temperature.



(a)

(b)



(c)

Figure 46: Heat Flux vs. Time for different MOFs; (a) HKUST-1, (b) NICS-6 and (c) MOF-5

Table 7: The heat of adsorption for different MOFs synthesized obtained from the calorimeter

Samples	Pdl (bar)	Psc (bar)	ΔP (bar)	Heat flux (J/m ²)	Area (m ²)	Total Heat (J)	Qsp(J)	Qad (J)
Spurious Heat	2.7	0.5	2.2	4421.12	0.0009	3.979	3.3783	-
	2.2	1.3	0.9	2339.3	0.0009	2.1054	1.382	-
	2	1.6	0.4	1453.11	0.0009	1.3078	0.6142	-
	1.9	1.8	0.1	779.49	0.0009	0.7015	0.1536	-
	1.8	1.8	0	705.86	0.0009	0.6353	0	-
HKUST-1	2.7	0.3	2.4	23683.52	0.0009	21.315	3.6854	17.629
	2.1	1.1	1	9549.68	0.0009	8.5947	1.5356	7.0591
	1.8	1.4	0.4	4741.56	0.0009	4.2674	0.6142	3.6532
	1.6	1.6	0	2075.49	0.0009	1.8679	0	1.8679
(NICS-6)	2.7	0.7	2	4000.96	0.0009	3.6009	3.0712	0.5297
	2.3	1.5	0.8	2009.36	0.0009	1.8084	1.2285	0.5799
	2.1	1.8	0.3	1160.86	0.0009	1.0448	0.4607	0.5841
	2	2	0	482.84	0.0009	0.4346	0	0.4346
MOF-5	2.9	1.2	1.7	4548.46	0.0009	4.0936	2.6105	1.4831
	2.6	1.8	0.8	1971.65	0.0009	1.7745	1.2285	0.546
	2.4	2.1	0.3	1204.04	0.0009	1.0836	0.4607	0.623
	2.3	2.3	0	629.79	0.0009	0.5668	0	0.5668

Pdl- Dosing loop pressure; Psc- Sample loop pressure; Qsp- Spurious Heat; Qad- Adsorption Heat

From the above Table 7, it is clear that there is an exothermic reaction happening in the case of HKUST-1, which raised its heat flux to 23684 J/K at $\Delta P = 2.4$ bar, and that

came down to 4742 j/k at $\Delta P = 0.4$ bar. However, in the case of Magnesium framework and MOF-5, the highest flux obtained is in the range of 4000 j/k in $\Delta P = 2$ bar, which is lowered by an order-of-magnitude when compared to HKUST-1. Thus, these analyses prove that HKUST-1 is an excellent adsorbent of methane gas.

When comparing the heat of adsorption values (Q_{ad}), the HKUST-1 was calculated as 17.6297 joules after subtracting the spurious heat. In contrast, in the case of Mg MOF, the adsorption values are around 0.5 J, which is the marginal error obtained in Figure 44. Hence in NICS-6, there was no adsorption of methane at this range of pressure. Nevertheless, in MOF-5, the Q_{st} values were very low as magnesium framework below 1 bar, while when the pressure is increased above 1 bar, the heat of adsorption values started rising to 1.5 J, which explains there is adsorption happening. Out of these three MOFs, HKUST-1 comes up with good adsorbent MOF for methane gas. For more clarification, another graph of $\ln Q_{ad}$ vs. pressure difference is plotted, as illustrated in Figure 47.

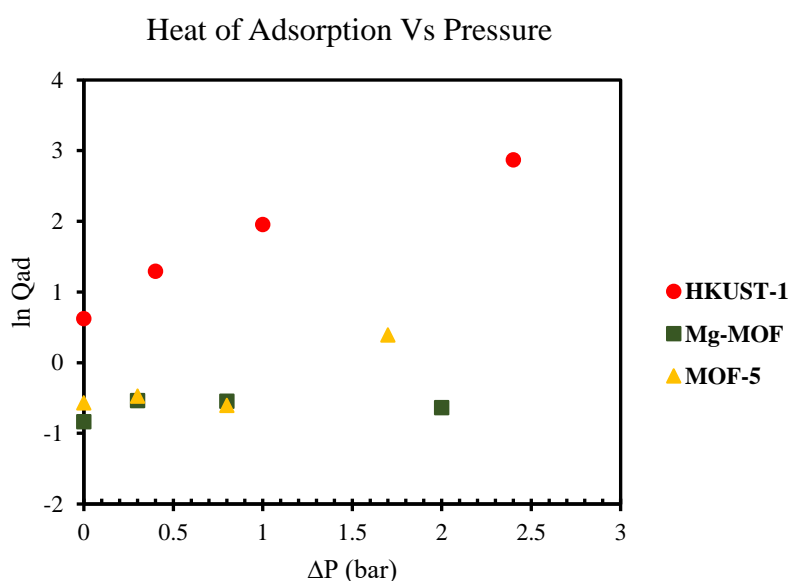


Figure 47: $\ln Q_{ad}$ vs. ΔP for HKUST-1, NICS-6, and MOF-5.

The log plots are useful for examining the low-pressure portion of the adsorption isotherm. From the above Figure 47, if the trendline was added to the NICS-6 curve, all the values seem to be constant at a pressure ranging 0-3 bar, which illustrates there is no adsorption of methane happening. In the case of MOF-5, the adsorption was increasing above 1 bar, whereas HKUST-1 gives good heat of adsorption in this pressure range that proves it is a good adsorbent for methane gas.

Chapter 5: Conclusion

For the design of new MOFs or isorecticular MOFs, new approaches have been explored, such as flexible or breathing MOFs, linker engineering, and functionalization. Pore engineering via functionalization have shown good results in fine-tuning the design of MOF for gas storage and delivery. A specific advantage of the approaches mentioned above is that the organic group can be rationally selected and combined with desired functional properties. This will allow for the best structure of adsorbent and results in great interaction with gas-phase molecules. Further experimental studies directed towards determining the influence of the metal precursors would assist in developing strategies to maximize natural gas delivery. Moreover, experimental studies on the effects of functional groups, such as hydrophilicity, would reveal further possible advances for real-world application of MOFs. In addition, it is critical to minimize the cost of MOFs for commercial viability. The manufacturing cost of MOFs can be reduced by minimizing the cost of organic linkers.

In this study, different MOFs were successfully synthesized by the solvothermal process. The samples were characterized by different techniques like XRD, SEM, TGA, and Nitrogen adsorption. The adsorption properties of natural gas on the organic frameworks were studied using gas chromatography and gas calorimeter experiments. A calorimeter setup was designed and manufactured for conducting the adsorption experiments. The XRD pattern obtained for the MOFs synthesized was compared to the simulated pattern, which showed proper matching. From the nitrogen adsorption experiments, HKUST-1 has a high surface area compared to that of MOF-5, and further, the filling of micropores and macropores at the pressure ranges were discussed.

In TGA analysis, Mg MOF had higher thermal stability of the above 500⁰C, whereas HKUST-1 was in the range of 375-400⁰C. The temperature range of HKUST-1 is enough for the application of ANG in various fields. Furthermore, HKUST-1 proved that this MOF is to be the best for adsorption of methane as well as the separation of a gaseous mixture by the gas chromatographic experimental setup. The heat of adsorption for MOFs was studied using gas calorimetric experiments at 273 K and 0-3 bar pressure. In HKUST-1, there was an exothermic reaction due to the adsorption of methane gas, and as the pressure increased, the adsorption was also increasing. Furthermore, MOF-5 has noticed as not a suitable adsorbent of methane gas at low pressure, but above 1 bar, it showed adsorption, whereas NICS-6 showed no adsorption of methane gas in this pressure range.

Future work into building MOFs for methane storage require focusing on extra-adsorption sites, phase change processes, MOF structural phase changes, and structure flexibility during adsorption. Extracting new/hidden adsorption sites is a hot research topic because it will enhance storage capacity. Whether through functionalization or combining two MOF lattices, there is huge potential in unlocking these extra sites. Another research area that needs more experimental data is the phase change that occurs during adsorption. The process of phase change is important in understanding how heat is generated in the MOF lattice. The structural change will aid in understanding MOF selectivity of methane for natural gas applications. Finally, it is important to study MOF flexibility during adsorption regarding temperature, pressure, and density. This is important for designing MOFs with good mechanical properties. These experimental avenues will help in building MOFs for real-world methane storage applications.

References

- Akella, A. K., Saini, R. P., & Sharma, M. P. (2009). Social, economical and environmental impacts of renewable energy systems. *Renewable Energy*, *34*(2), 390–396. <https://doi.org/10.1016/j.renene.2008.05.002>
- Alhamami, M., Doan, H., & Cheng, C. H. (2014). A review on breathing behaviors of metal-organic-frameworks (MOFs) for gas adsorption. *Materials*, *7*(4), 3198–3250. <https://doi.org/10.3390/ma7043198>
- Alvarez, R. A., Pacala, S. W., Winebrake, J. J., Chameides, W. L. & Hamburg, S. P. (2012). Greater focus needed on methane leakage from natural gas infrastructure. *Proceedings of the National Academy of Sciences*, *109*(17), 6435–6440. <https://doi.org/10.1073/pnas.1202407109>
- American Chemical Society. (2017). Round two for MOF commercialization. *Chemical & Engineering News*, *95*(24), 30–34.
- ARPA-E. (2012). *MOVE Program Overview*. Retrieved June 27, 2019, from http://arpa-e.energy.gov/sites/default/files/documents/files/MOVE_ProgramOverview.pdf
- Babaei, H., McGaughey, A. J. H., & Wilmer, C. E. (2016). Effect of pore size and shape on the thermal conductivity of metal-organic frameworks. *Chemical Science*, *8*(1), 583–589. <https://doi.org/10.1039/C6SC03704F>
- Babaei, H., McGaughey, A. J. H., & Wilmer, C. E. (2018). Transient Mass and Thermal Transport during Methane Adsorption into the Metal-Organic Framework HKUST-1. *ACS Applied Materials and Interfaces*, *10*(3), 2400–2406. <https://doi.org/10.1021/acsami.7b13605>
- Babaei, H., & Wilmer, C. E. (2016). Mechanisms of Heat Transfer in Porous Crystals Containing Adsorbed Gases: Applications to Metal-Organic Frameworks. *Physical Review Letters*, *116*(2), 025902. <https://doi.org/10.1103/PhysRevLett.116.025902>
- Bae, C., & Kim, J. (2017). Alternative fuels for internal combustion engines. *Proceedings of the Combustion Institute*, *36*(3), 3389–3413. <https://doi.org/10.1016/j.proci.2016.09.009>
- Bae, Y. S., & Snurr, R. Q. (2010). Optimal isosteric heat of adsorption for hydrogen storage and delivery using metal-organic frameworks. *Microporous and Mesoporous Materials*, *132*(1–2), 300–303. <https://doi.org/10.1016/j.micromeso.2010.02.023>
- BASF Metal Organic Frameworks (MOFs): Innovative Fuel Systems for Natural Gas Vehicles (NGVs). (2014). *Chem. Soc. Rev.*, *43*(16), 6173–6174. <https://doi.org/10.1039/C4CS90070G>
- Bolinois, L., Kundu, T., Wang, X., Wang, Y., Hu, Z., Koh, K., & Zhao, D. (2017).

- Breathing-induced new phase transition in an MIL-53(Al)-NH₂ metal-organic framework under high methane pressures. *Chem. Commun.*, 53(58), 8118–8121. <https://doi.org/10.1039/C7CC02743E>
- Bordiga, S., Regli, L., Bonino, F., Groppo, E., Lamberti, C., Xiao, b., Wheatley, P. S., Morris, R. E. & Zecchina, A. (2007). Adsorption properties of HKUST-1 toward hydrogen and other small molecules monitored by IR. *Physical Chemistry Chemical Physics*, 9(21), 2676–2685. <https://doi.org/10.1039/b703643d>
- Boutin, A., Coudert, F.-X., Springuel-Huet, M.-A., Neimark, A. V, Férey, G., & Fuchs, A. H. (2010). The behavior of flexible MIL-53(Al) upon CH₄ and CO₂ adsorption. *Journal of Physical Chemistry C*, 114(50), 22237–22244. <https://doi.org/10.1021/jp108710h>
- BP. (2015). BP Statistical Review of World Energy June 2015. In *British Petroleum*. Retrieved November 6, 2019, from <https://doi.org/bp.com/statisticalreview>
- Braga, D., & Grepioni*, F. (1999). Organometallic crystal engineering: prospects for a systematic design. *Coordination Chemistry Reviews*, 183(1), 19–41. [https://doi.org/http://dx.doi.org/10.1016/S0010-8545\(98\)90172-2](https://doi.org/http://dx.doi.org/10.1016/S0010-8545(98)90172-2)
- Chang, K. J., & Talu, O. (1996). Behavior and performance of adsorptive natural gas storage cylinders during discharge. *Applied Thermal Engineering*, 16(5), 359–374. [https://doi.org/10.1016/1359-4311\(95\)00017-8](https://doi.org/10.1016/1359-4311(95)00017-8)
- Chen, L., Morrison, C. A., & Düren, T. (2012). Improving predictions of gas adsorption in metal-organic frameworks with coordinatively unsaturated metal sites: Model potentials, ab initio parameterization, and gcmc simulations. *Journal of Physical Chemistry C*, 116(35), 18899–18909. <https://doi.org/10.1021/jp3062527>
- Chui, S. S. Y., Lo, S. M. F., Charmant, J. P. H., Orpen, A. G., & Williams, I. D. (1999). A chemically functionalizable nanoporous material [Cu₃(TMA)₂(H₂O)₃](n). *Science*, 283(5405), 1148–1150. <https://doi.org/10.1126/science.283.5405.1148>
- Cohen, S. M. (2012). Postsynthetic methods for the functionalization of metal-organic frameworks. *Chemical Reviews*, 112(2), 970–1000. <https://doi.org/10.1021/cr200179u>
- Compressed Natural Gas (CNG) in transport / *ClimateTechWiki*. (2012). Retrieved September 13, 2019, from <https://www.ctc-n.org/technologies/compressed-natural-gas-cng-fuel>
- Coren, M. J. (2018). *Nine countries say they'll ban internal combustion engines. So far, it's just words*. Quartz. Retrieved July 28, 2019, from <https://qz.com/1341155/nine-countries-say-they-will-ban-internal-combustion-engines-none-have-a-law-to-do-so/>
- Deng, H., Grunder, S., Cordova, K. E., Valente, C., Furukawa, H., Hmadeh, M., Gándara, F., Whalley, A. C., Liu, Z., Asahina, S., Kazumori, H., O’Keeffe, M.,

- Terasaki, O., Stoddart, J. F., & Yaghi, O. M. (2012). Large-pore apertures in a series of metal-organic frameworks. *Science*, 336(6084), 1018–1023. <https://doi.org/10.1126/science.1220131>
- Deng, H., Doonan, C. J., Furukawa, H., Ferreira, R. B., Towne, J., Knobler, C. B., Wang, B., & Yaghi, O. M. (2010). Multiple functional groups of varying ratios in metal-organic frameworks. *Science*, 327(5967), 846–850. <https://doi.org/10.1126/science.1181761>
- Dietzel, P. D. C., Besikiotis, V., & Blom, R. (2009). Application of metal-organic frameworks with coordinatively unsaturated metal sites in storage and separation of methane and carbon dioxide. *Journal of Materials Chemistry*, 19(39), 7362–7370. <https://doi.org/10.1039/b911242a>
- Drennen, T. E. (1994). Renewable Energy: Sources for Fuels and Electricity. *Journal of Environmental Quality*, 23(3), 622–622. <https://doi.org/10.2134/jeq1994.00472425002300030032x>
- Dunne, J. A., Mariwala, R., Rao, M., Sircar, S., Gorte, R. J., & Myers, A. L. (1996). Calorimetric Heats of Adsorption and Adsorption Isotherms. 1. O₂, N₂, Ar, CO₂, CH₄, C₂H₆, and SF₆ on Silicalite. *Langmuir*, 12(24), 5888–5895. <https://doi.org/10.1021/la960495z>
- Eddaoudi, M., Moler, D. B., Li, H., Chen, B., Reineke, T. M., O’Keeffe, M., & Yaghi, O. M. (2001). Modular chemistry: Secondary building units as a basis for the design of highly porous and robust metal-organic carboxylate frameworks. *Accounts of Chemical Research*, 34(4), 319–330. <https://doi.org/10.1021/ar000034b>
- EIA. (2010). Key World Energy Statistics. *Statistics*. Energy Information Administration, USA. Retrieved September 11, 2019, from <https://www.eia.gov/international/data/world>
- European Council. (2018). 2030 climate & energy framework | Climate Action. 2030 Climate & Energy Framework. Retrieved February 6, 2019, from https://ec.europa.eu/clima/policies/strategies/2030_en%0Ahttps://ec.europa.eu/clima/policies/strategies/2030_en#tab-0-1
- Farha, O. K., & Hupp, J. T. (2010). Rational design, synthesis, purification, and activation of metal-organic framework materials. *Accounts of Chemical Research*, 43(8), 1166–1175. <https://doi.org/10.1021/ar1000617>
- Filipe A. Almeida Paz, Jacek Klinowski, Sergio M. F. Vilela, Joao P. C. Tome, J. A. S. C. and J. R. (2012). Ligand design for functional metal-organic frameworks. *Chemical Society Reviews*, 41(3), 1088–1110. <https://doi.org/10.1039/c1cs15055c>
- Fu, F., Lin, L., & Xu, E. (2017). 4 - Functional pretreatments of natural raw materials. In *Advanced High Strength Natural Fibre Composites in Construction* (pp. 87–114). Woodhead Publishing. <http://www.sciencedirect.com/science/article/pii/B9780081004111000042>

- Furukawa, H., Cordova, K. E., O’Keeffe, M., & Yaghi, O. M. (2013a). The chemistry and applications of metal-organic frameworks. *Science*, *341*(6149), 973–987. <https://doi.org/10.1126/science.1230444>
- Furukawa, H., Cordova, K. E., O’Keeffe, M., & Yaghi, O. M. (2013b). The chemistry and applications of metal-organic frameworks. *Science*, *341*, 1–12. <https://doi.org/10.1126/science.1230444>
- Furukawa, H., Ko, N., Go, Y. B., Aratani, N., Choi, S. B., Choi, E., Yazaydin, A. Ö., Snurr, R. Q., O’Keeffe, M., Kim, J., & Yaghi, O. M. (2010). Ultrahigh porosity in metal-organic frameworks. *Science*, *329*(5990), 424–428. <https://doi.org/10.1126/science.1192160>
- Gándara, F., Furukawa, H., Lee, S., & Yaghi, O. M. (2014). High methane storage capacity in aluminum metal-organic frameworks. *Journal of the American Chemical Society*, *136*(14), 5271–5274. <https://doi.org/10.1021/ja501606h>
- García-Cuello, V., Moreno-Piraján, J. C., Giraldo-Gutiérrez, L., Sapag, K., & Zgrablich, G. (2008). Design, calibration, and testing of a new Tian-Calvet heat-flow microcalorimeter for measurement of differential heats of adsorption. *Instrumentation Science and Technology*, *36*(5), 455–475. <https://doi.org/10.1080/10739140802234899>
- Getman, R. B., Bae, Y. S., Wilmer, C. E., & Snurr, R. Q. (2012). Review and analysis of molecular simulations of methane, hydrogen, and acetylene storage in metal-organic frameworks. *Chemical Reviews*, *112*(2), 703–723. <https://doi.org/10.1021/cr200217c>
- Gómez-Gualdrón, D. A., Wilmer, C. E., Farha, O. K., Hupp, J. T., & Snurr, R. Q. (2014a). Exploring the limits of methane storage and delivery in nanoporous materials. *Journal of Physical Chemistry C*, *118*(13), 6941–6951. <https://doi.org/10.1021/jp502359q>
- Gómez-Gualdrón, D. A., Wilmer, C. E., Farha, O. K., Hupp, J. T., & Snurr, R. Q. (2014b). Exploring the limits of methane storage and delivery in nanoporous materials. *Journal of Physical Chemistry C*, *118*(13), 6941–6951. <https://doi.org/10.1021/jp502359q>
- Gotthardt, M. A., Schoch, R., Wolf, S., Bauer, M., & Kleist, W. (2015). Synthesis and characterization of bimetallic metal-organic framework Cu-Ru-BTC with HKUST-1 structure. *Dalton Transactions*, *44*(5), 2052–2056. <https://doi.org/10.1039/c4dt02491e>
- Guo, Z., Wu, H., Srinivas, G., Zhou, Y., Xiang, S., Chen, Z., Yang, Y., Zhou, W., O’Keeffe, M., & Chen, B. (2011). A metal-organic framework with optimized open metal sites and pore spaces for high methane storage at room temperature. *Angewandte Chemie - International Edition*, *50*(14), 3178–3181. <https://doi.org/10.1002/anie.201007583>
- Hamza, U. D., Nasri, N. S., Mohammed, J., & Majid, Z. A. (2016). Natural gas adsorption on biomass derived activated carbons: A mini review. *MATEC Web*

- of Conferences*, 60(04011), 1–5.
<https://doi.org/10.1051/mateconf/20166004011>
- He, Y., Zhou, W., Qian, G., & Chen, B. (2014). Methane storage in metal-organic frameworks. *Chemical Society Reviews*, 43(16), 5657–5678.
<https://doi.org/10.1039/c4cs00032c>
- He, Y., Zhou, W., Yildirim, T., & Chen, B. (2013). A series of metal-organic frameworks with high methane uptake and an empirical equation for predicting methane storage capacity. *Energy and Environmental Science*, 6(9), 2735–2744.
<https://doi.org/10.1039/c3ee41166d>
- Himeno, S., Komatsu, T., & Fujita, S. (2005). High-Pressure Adsorption Equilibria of Methane and Carbon Dioxide on Several Activated Carbons. *Journal of Chemical & Engineering Data*, 50(2), 369–376.
<https://doi.org/10.1021/je049786x>
- Horcajada, P., Serre, C., Vallet-Regí, M., Sebban, M., Taulelle, F., & Férey, G. (2006). Metal-organic frameworks as efficient materials for drug delivery. *Angewandte Chemie - International Edition*, 45(36), 5974–5978.
<https://doi.org/10.1002/anie.200601878>
- Howarth, A. J., Liu, Y., Li, P., Li, Z., Wang, T. C., Hupp, J. T., & Farha, O. K. (2016). Chemical, thermal and mechanical stabilities of metal-organic frameworks. *Nature Reviews Materials*, 1(3), 1–15.
<https://doi.org/10.1038/natrevmats.2015.18>
- Huang, B. L., Ni, Z., Millward, A., McGaughey, A. J. H., Uher, C., Kaviani, M., & Yaghi, O. (2007). Thermal conductivity of a metal-organic framework (MOF-5): Part II. Measurement. *International Journal of Heat and Mass Transfer*, 50(3–4), 405–411. <https://doi.org/10.1016/j.ijheatmasstransfer.2006.10.001>
- Huang, J., Xia, X., Hu, X., Li, S., & Liu, K. (2019). A general method for measuring the thermal conductivity of MOF crystals. *International Journal of Heat and Mass Transfer*, 138(1), 11–16.
<https://doi.org/10.1016/j.ijheatmasstransfer.2019.04.018>
- Hyeon, S., Kim, Y.-C., & Kim, J. (2017). Computational prediction of high methane storage capacity in V-MOF-74. *Physical Chemistry Chemical Physics*, 19(31), 21132–21139. <https://doi.org/10.1039/C7CP03605A>
- Id, U. (2016). *The Outlook for energy: a view to 2040*.
<https://doi.org/10.1080/01998595.2012.10491656>
- Jacoby, M. (2008). Heading to market with MOFS. *Chemical and Engineering News*, 86(34), 13–16. <https://doi.org/10.1021/cen-v086n034.p013>
- James, S. L. (2003). Metal-organic frameworks. *Chemical Society Reviews*, 32(5), 276–288. <https://doi.org/10.1039/b200393g>
- Jiang, J., Furukawa, H., Zhang, Y. B., & Yaghi, O. M. (2016). High Methane Storage Working Capacity in Metal-Organic Frameworks with Acrylate Links. *Journal*

of the American Chemical Society, 138(32), 10244–10251.
<https://doi.org/10.1021/jacs.6b05261>

- Joseph M. J. (2013). BASF to showcase metal organic frameworks (MOFs) for energy storage at NGV Americas Conference. *North American Natural Gas Vehicle Conference and Expo*, <https://www.basf.com/us/en/company/news-and-media/>.
https://www.hydrogen.energy.gov/pdfs/review15/st010_veenstra_2015_o.pdf
- Kloutse, F. A., Zacharia, R., Cossement, D., & Chahine, R. (2015). Specific heat capacities of MOF-5, Cu-BTC, Fe-BTC, MOF-177 and MIL-53 (Al) over wide temperature ranges: Measurements and application of empirical group contribution method. *Microporous and Mesoporous Materials*, 217(1), 1–5.
<https://doi.org/10.1016/j.micromeso.2015.05.047>
- Kondo, M., Yoshitomi, T., Seki, K., Matsuzaka, H., & Kitagawa, S. (1997). Three-Dimensional Framework with Channeling Cavities for Small Molecules: $\{[M_2(4,4'\text{-bpy})_3(\text{NO}_3)_4] \cdot x\text{H}_2\text{O}\}_n$ (M = Co, Ni, Zn). *Angewandte Chemie (International Edition in English)*, 36(16), 1725–1727.
<https://doi.org/10.1002/anie.199717251>
- Li, B., Wen, H. M., Wang, H., Wu, H., Yildirim, T., Zhou, W., & Chen, B. (2015). Porous metal-organic frameworks with Lewis basic nitrogen sites for high-capacity methane storage. *Energy and Environmental Science*, 8(8), 2504–2511.
<https://doi.org/10.1039/c5ee01531f>
- Li, B., Wen, H. M., Zhou, W., Xu, J. Q., & Chen, B. (2016). Porous Metal-Organic Frameworks: Promising Materials for Methane Storage. *Chem*, 1(4), 557–580.
<https://doi.org/10.1016/j.chempr.2016.09.009>
- Li, H., Eddaoudi, M., O’Keeffe, M., & Yaghi, O. M. (1999). Design and synthesis of an exceptionally stable and highly porous metal-organic framework. *Nature*, 402, 276–279. <https://doi.org/10.1038/46248>
- Li, H., Wang, K., Sun, Y., Lollar, C. T., Li, J., & Zhou, H. C. (2018). Recent advances in gas storage and separation using metal-organic frameworks. *Materials Today*, 21(2), 108–121. <https://doi.org/10.1016/j.mattod.2017.07.006>
- Li, L., Tang, S., Wang, C., Lv, X., Jiang, M., Wu, H., & Zhao, X. (2014a). High gas storage capacities and stepwise adsorption in a UiO type metal-organic framework incorporating Lewis basic bipyridyl sites. *Chemical Communications*, 50, 2304–2307. <https://doi.org/10.1039/c3cc48275h>
- Li, L., Tang, S., Wang, C., Lv, X., Jiang, M., Wu, H., & Zhao, X. (2014b). High gas storage capacities and stepwise adsorption in a UiO type metal-organic framework incorporating Lewis basic bipyridyl sites. *Chemical Communications*, 50(18), 2304–2307. <https://doi.org/10.1039/c3cc48275h>
- Li, Q., Zhang, W., Miljanić, O. Š., Sue, C. H., Zhao, Y. L., Liu, L., Knobler, C. B., Stoddart, J. F., & Yaghi, O. M. (2009). Docking in metal-organic frameworks. *Science*, 325(5942), 855–859. <https://doi.org/10.1126/science.1175441>

- Liang, C. C., Shi, Z. L., He, C. T., Tan, J., Zhou, H. D., Zhou, H. L., Lee, Y., & Zhang, Y. B. (2017). Engineering of Pore Geometry for Ultrahigh Capacity Methane Storage in Mesoporous Metal-Organic Frameworks. *Journal of the American Chemical Society*, *139*(38), 13300–13303. <https://doi.org/10.1021/jacs.7b08347>
- Lin, X., Telepeni, I., Blake, A. J., Dailly, A., Brown, C. M., Simmons, J. M., Zoppi, M., Walker, G. S., Thomas, K. M., Mays, T. J., Hubberstey, P., Champness, N. R., & Schröder, M. (2009). High capacity hydrogen adsorption in Cu(II) tetracarboxylate framework materials: The role of pore size, ligand functionalization, and exposed metal sites. *Journal of the American Chemical Society*, *131*(6), 2159–2171. <https://doi.org/10.1021/ja806624j>
- Lin, Y., Kong, C., Zhang, Q., & Chen, L. (2017). Metal-Organic Frameworks for Carbon Dioxide Capture and Methane Storage. *Advanced Energy Materials*, *7*(4), 1601296. <https://doi.org/10.1002/aenm.201601296>
- Liu, L., Konstas, K., Hill, M. R., & Telfer, S. G. (2013). Programmed pore architectures in modular quaternary metal-organic frameworks. *Journal of the American Chemical Society*, *135*(47), 17731–17734. <https://doi.org/10.1021/ja4100244>
- Loiseau, T., Serre, C., Huguenard, C., Fink, G., Taulelle, F., Henry, M., Bataille, T., & Férey, G. (2004). A Rationale for the Large Breathing of the Porous Aluminum Terephthalate (MIL-53) Upon Hydration. *Chemistry - A European Journal*, *10*(6), 1373–1382. <https://doi.org/10.1002/chem.200305413>
- Long, J. R., & Yaghi, O. M. (2009). The pervasive chemistry of metal-organic frameworks. *Chemical Society Reviews*, *38*(5), 1213–1214. <https://doi.org/10.1039/b903811f>
- Luo, J., McCabe, R. W., Dearth, M. A., & Gorte, R. J. (2014). Transient adsorption studies of automotive hydrocarbon traps. *AIChE Journal*, *60*(8), 2875–2881. <https://doi.org/10.1002/aic.14477>
- Ma, S., Sun, D., Simmons, J. M., Collier, C. D., Yuan, D., & Zhou, H. C. (2008). Metal-organic framework from an anthracene derivative containing nanoscopic cages exhibiting high methane uptake. *Journal of the American Chemical Society*, *130*(3), 1012–1016. <https://doi.org/10.1021/ja0771639>
- Macrae, C. F., Sovago, I., Cottrell, S. J., Galek, P. T. A., McCabe, P., Pidcock, E., Platings, M., Shields, G. P., Stevens, J. S., Towler, M., & Wood, P. A. (2020). Mercury 4.0: from visualization to analysis, design and prediction. *Journal of Applied Crystallography*, *53*(1), 226–235. <https://doi.org/10.1107/S1600576719014092>
- Mahmoud, E., Ali, L., Sayah, A. El, Alkhatib, S. A., Abdulsalam, H., Juma, M., & Al-Muhtaseb, A. H. (2019). Implementing metal-organic frameworks for natural gas storage. *Crystals*, *9*(406), 1–19. <https://doi.org/10.3390/cryst9080406>

- Makal, T. A., Li, J. R., Lu, W., & Zhou, H. C. (2012). Methane storage in advanced porous materials. *Chemical Society Reviews*, 41(23), 7761–7779. <https://doi.org/10.1039/c2cs35251f>
- Mali, G., Trebosc, J., Martineau, C., & Mazaj, M. (2015). Structural study of Mg-based metal-organic frameworks by X-ray diffraction, ¹H, ¹³C, and ²⁵Mg solid-state NMR spectroscopy, and first-principles calculations. *Journal of Physical Chemistry C*, 119(14), 7831–7841. <https://doi.org/10.1021/acs.jpcc.5b01381>
- Mallick, A., Kundu, T., & Banerjee, R. (2012). Correlation between coordinated water content and proton conductivity in Ca–BTC-based metal–organic frameworks. *Chemical Communications*, 48(70), 8829–8831. <https://doi.org/10.1039/c2cc34006b>
- Mason, J. A., Oktawiec, J., Taylor, M. K., Hudson, M. R., Rodriguez, J., Bachman, J. E., Gonzalez, M. I., Cervellino, A., Guagliardi, A., Brown, C. M., Llewellyn, P. L., Masciocchi, N., & Long, J. R. (2015). Methane storage in flexible metal-organic frameworks with intrinsic thermal management. *Nature*, 527(7578), 357–361. <https://doi.org/10.1038/nature15732>
- Mason, J. A., Veenstra, M., & Long, J. R. (2014). Evaluating metal–organic frameworks for natural gas storage. *Chem. Sci.*, 5(1), 32–51. <https://doi.org/10.1039/C3SC52633J>
- Matranga, K. R., Myers, A. L., & Glandt, E. D. (1992). Storage of Natural-Gas By Adsorption on Activated Carbon. *Chemical Engineering Science*, 47(7), 1569–1579. [https://doi.org/10.1016/0009-2509\(92\)85005-v](https://doi.org/10.1016/0009-2509(92)85005-v)
- Mazaj, M., Birsa Čelič, T., Mali, G., Rangus, M., Kaučič, V., & Zabukovec Logar, N. (2013). Control of the crystallization process and structure dimensionality of Mg-benzene-1,3,5-tricarboxylates by tuning solvent composition. *Crystal Growth and Design*, 19(8), 3825–3834. <https://doi.org/10.1021/cg400929z>
- McMahon, M. M. (2017). NuMat Brings First MOF-Enabled Gas Storage Product to Market | Institute for Sustainability and Energy at Northwestern (ISEN). In *Northwestern institute for sustainability and energy*. Retrieved April 6, 2019, from <https://isen.northwestern.edu/numat-brings-first-mof-enabled-gas-storage-product-to-market>
- Menon, V. C., & Komarneni, S. (1998). Porous adsorbents for vehicular natural gas storage: a review. *Journal of Porous Materials*, 5(1), 43–58. <https://doi.org/10.1023/A:1009673830619>
- Moellmer, J., Moeller, A., Dreisbach, F., Glaeser, R., & Staudt, R. (2011). High pressure adsorption of hydrogen, nitrogen, carbon dioxide and methane on the metal-organic framework HKUST-1. *Microporous and Mesoporous Materials*, 138(1–3), 140–148. <https://doi.org/10.1016/j.micromeso.2010.09.013>
- Moghadam, P. Z., Li, A., Wiggin, S. B., Tao, A., Maloney, A. G. P., Wood, P. A., Ward, S. C., & Fairen-Jimenez, D. (2017). Development of a Cambridge

- Structural Database Subset: A Collection of Metal-Organic Frameworks for Past, Present, and Future. *Chemistry of Materials*, 29(7), 2618–2625. <https://doi.org/10.1021/acs.chemmater.7b00441>
- Moosavi, S. M., Boyd, P. G., Sarkisov, L., & Smit, B. (2018). Improving the Mechanical Stability of Metal-Organic Frameworks Using Chemical Caryatids. *ACS Central Science*, 4(7), 832–839. <https://doi.org/10.1021/acscentsci.8b00157>
- Morris, R. E., & Wheatley, P. S. (2008). Gas storage in nanoporous materials. *Angewandte Chemie - International Edition*, 47(27), 4966–4981. <https://doi.org/10.1002/anie.200703934>
- Moulton, B., & Zaworotko, M. J. (2001). From molecules to crystal engineering: Supramolecular isomerism and polymorphism in network solids. *Chemical Reviews*, 101(6), 1629–1658. <https://doi.org/10.1021/cr9900432>
- Mu, B., & Walton, K. S. (2011). Thermal analysis and heat capacity study of metal-organic frameworks. *Journal of Physical Chemistry C*, 115(46), 22748–22754. <https://doi.org/10.1021/jp205538a>
- Mueller, U., Schubert, M., Teich, F., Puetter, H., Schierle-Arndt, K., & Pastré, J. (2006). Metal-organic frameworks—prospective industrial applications. *J. Mater. Chem.*, 16(7), 626–636. <https://doi.org/10.1039/B511962F>
- Nathan, A. J., & Scobell, A. (2012). How China sees America. *Foreign Affairs*, 91(5), 32–47. <https://doi.org/10.1017/CBO9781107415324.004>
- Nguyen, N. T. T., Furukawa, H., Gándara, F., Nguyen, H. T., Cordova, K. E., & Yaghi, O. M. (2014). Selective capture of carbon dioxide under humid conditions by hydrophobic chabazite-type zeolitic imidazolate frameworks. *Angewandte Chemie - International Edition*, 53(40), 10645–10648. <https://doi.org/10.1002/anie.201403980>
- NGV Global. (2019). *Current Natural Gas Vehicle Statistics | NGV Global Knowledgebase*. Retrieved August 9, 2019, from <http://www.iangv.org/current-ngv-stats/>
- Noro, S., Kitagawa, S., Kondo, M., & Seki, K. (2000). A New, Methane Adsorbent, Porous Coordination Polymer [$\{\text{CuSiF}_6(4,4'\text{-bipyridine})_2\}_n$]. *Angewandte Chemie International Edition*, 39(12), 2081–2084. [https://doi.org/10.1002/1521-3773\(20000616\)39:12<2081::aid-anie2081>3.0.co;2-a](https://doi.org/10.1002/1521-3773(20000616)39:12<2081::aid-anie2081>3.0.co;2-a)
- O’Keeffe, M., & Yaghi, O. M. (2012). Deconstructing the crystal structures of metal-organic frameworks and related materials into their underlying nets. *Chemical Reviews*, 112(2), 675–702. <https://doi.org/10.1021/cr200205j>
- Ockwig, N. W., Delgado-Friedrichs, O., O’Keeffe, M., & Yaghi, O. M. (2005). Reticular chemistry: Occurrence and taxonomy of nets and grammar for the design of frameworks. *Accounts of Chemical Research*, 38(3), 176–182. <https://doi.org/10.1021/ar020022l>

- Öhrström, L. (2015). Let's talk about MOFs—Topology and terminology of metal-organic frameworks and why we need them. *Crystals*, 5(1), 154–162. <https://doi.org/10.3390/cryst5010154>
- Painuly, J. P. (2001). Barriers to renewable energy penetration: A framework for analysis. *Renewable Energy*, 24(1), 73–89. [https://doi.org/10.1016/S0960-1481\(00\)00186-5](https://doi.org/10.1016/S0960-1481(00)00186-5)
- Park, K. S., Ni, Z., Côté, A. P., Choi, J. Y., Huang, R., Uribe-Romo, F. J., Chae, H. K., O'Keeffe, M., & Yaghi, O. M. (2006). Exceptional chemical and thermal stability of zeolitic imidazolate frameworks. *Proceedings of the National Academy of Sciences*, 103(27), 10186–10191. <https://doi.org/10.1073/pnas.0602439103>
- Peng, Y., Krungleviciute, V., Eryazici, I., Hupp, J. T., Farha, O. K., & Yildirim, T. (2013a). Methane storage in metal-organic frameworks: Current records, surprise findings, and challenges. *Journal of the American Chemical Society*, 135(32), 11887–11894. <https://doi.org/10.1021/ja4045289>
- Peng, Y., Srinivas, G., Wilmer, C. E., Eryazici, I., Snurr, R. Q., Hupp, J. T., Yildirim, T., & Farha, O. K. (2013b). Simultaneously high gravimetric and volumetric methane uptake characteristics of the metal-organic framework NU-111. *Chemical Communications*, 49(29), 2992–2994. <https://doi.org/10.1039/c3cc40819a>
- Perry, J. J., Perman, J. A., & Zaworotko, M. J. (2009). Design and synthesis of metal-organic frameworks using metal-organic polyhedra as supermolecular building blocks. *Chemical Society Reviews*, 38(5), 1400–1417. <https://doi.org/10.1039/b807086p>
- Prajwal, B. P., & Ayappa, K. G. (2014). Evaluating methane storage targets: From powder samples to onboard storage systems. *Adsorption*, 20(5–6), 769–776. <https://doi.org/10.1007/s10450-014-9620-1>
- Quartapelle Procopio, E., Linares, F., Montoro, C., Colombo, V., Maspero, A., Barea, E., & Navarro, J. A. R. (2010). Cation-Exchange Porosity Tuning in Anionic Metal–Organic Frameworks for the Selective Separation of Gases and Vapors and for Catalysis. *Angewandte Chemie International Edition*, 49(40), 7308–7311. <https://doi.org/10.1002/anie.201003314>
- Rallapalli, P., Patil, D., Prasanth, K. P., Somani, R. S., Jasra, R. V., & Bajaj, H. C. (2010). An alternative activation method for the enhancement of methane storage capacity of nanoporous aluminium terephthalate, MIL-53(Al). *Journal of Porous Materials*, 17(5), 523–528. <https://doi.org/10.1007/s10934-009-9320-5>
- Rao, X., Cai, J., Yu, J., He, Y., Wu, C., Zhou, W., Yildirim, T., Chen, B., & Qian, G. (2013). A microporous metal–organic framework with both open metal and Lewis basic pyridyl sites for high C₂H₂ and CH₄ storage at room temperature. *Chemical Communications*, 49(60), 6719–6721. <https://doi.org/10.1039/c3cc41866a>

- Rosi, N. L., Eckert, J., Eddaoudi, M., Vodak, D. T., Kim, J., O’Keeffe, M., & Yaghi, O. M. (2003). Hydrogen storage in microporous metal-organic frameworks. *Science*, *300*(5622), 1127–1129. <https://doi.org/10.1126/science.1083440>
- Rowsell, J. L. C., Spencer, E. C., Eckert, J., Howard, J. A. K., & Yaghi, O. M. (2005). Gas adsorption sites in a large-pore metal-organic framework. *Science (New York, N.Y.)*, *309*(5739), 1350–1354. <https://doi.org/10.1126/science.1113247>
- Rubio-Martinez, M., Avci-Camur, C., Thornton, A. W., Imaz, I., MasPOCH, D., & Hill, M. R. (2017). New synthetic routes towards MOF production at scale. *Chemical Society Reviews*, *46*(11), 3453–3480. <https://doi.org/10.1039/c7cs00109f>
- Schoedel, A., Ji, Z., & Yaghi, O. M. (2016). The role of metal–organic frameworks in a carbon-neutral energy cycle. *Nature Energy*, *1*(4), 1–13. <https://doi.org/10.1038/nenergy.2016.34>
- Sculley, J., Yuan, D., & Zhou, H. C. (2011). The current status of hydrogen storage in metal–organic frameworks—updated. *Energy & Environmental Science*, *4*(8), 2721–2735. <https://doi.org/10.1039/c1ee01240a>
- Sezginel, K. B., Asinger, P. A., Babaei, H., & Wilmer, C. E. (2018). Thermal Transport in Interpenetrated Metal-Organic Frameworks. *Chemistry of Materials*, *30*(7), 2281–2286. <https://doi.org/10.1021/acs.chemmater.7b05015>
- Shen, J., Sulkowski, J., Beckner, M., & Dailly, A. (2015). Effects of textural and surface characteristics of metal-organic frameworks on the methane adsorption for natural gas vehicular application. *Microporous and Mesoporous Materials*, *212*(C), 80–90. <https://doi.org/10.1016/j.micromeso.2015.03.032>
- Siberio-Pérez, D. Y., Wong-Foy, A. G., Yaghi, O. M., & Matzger, A. J. (2007). Raman spectroscopic investigation of CH₄ and N₂ adsorption in metal-organic frameworks. *Chemistry of Materials*, *19*(15), 3681–3685. <https://doi.org/10.1021/cm070542g>
- Sircar, S., Golden, T. C., & Rao, M. B. (1996). Activated carbon for gas separation and storage. *Carbon*, *34*(1), 1–12. [https://doi.org/10.1016/0008-6223\(95\)00128-X](https://doi.org/10.1016/0008-6223(95)00128-X)
- Stock, N., & Biswas, S. (2012). Synthesis of metal-organic frameworks (MOFs): Routes to various MOF topologies, morphologies, and composites. *Chemical Reviews*, *112*(2), 933–969. <https://doi.org/10.1021/cr200304e>
- Suh, M. P., Cheon, Y. E., & Lee, E. Y. (2008). Syntheses and functions of porous metallosupramolecular networks. *Coordination Chemistry Reviews*, *252*(8–9), 1007–1026. <https://doi.org/10.1016/j.ccr.2008.01.032>
- Sun, Y., Liu, C., Su, W., Zhou, Y., & Zhou, L. (2009). Principles of methane adsorption and natural gas storage. *Adsorption*, *15*(2), 133–137. <https://doi.org/10.1007/s10450-009-9157-x>

- Szilágyi, P. Á., Serra-Crespo, P., Gascon, J., Geerlings, H., & Dam, B. (2016). The Impact of Post-Synthetic Linker Functionalization of MOFs on Methane Storage: The Role of Defects. *Frontiers in Energy Research*, 4(9), 1–6. <https://doi.org/10.3389/fenrg.2016.00009>
- Tagliabue, M., Rizzo, C., Millini, R., Dietzel, P. D. C., Blom, R., & Zanardi, S. (2011). Methane storage on CPO-27-Ni pellets. *Journal of Porous Materials*, 18(3), 289–296. <https://doi.org/10.1007/s10934-010-9378-0>
- Taylor, M. K., Runčevski, T., Oktawiec, J., Gonzalez, M. I., Siegelman, R. L., Mason, J. A., Ye, J., Brown, C. M., & Long, J. R. (2016). Tuning the Adsorption-Induced Phase Change in the Flexible Metal-Organic Framework Co(bdp). *Journal of the American Chemical Society*, 138(45), 15019–15026. <https://doi.org/10.1021/jacs.6b09155>
- Tian, T., Velazquez-Garcia, J., Bennett, T. D., & Fairen-Jimenez, D. (2015). Mechanically and chemically robust ZIF-8 monoliths with high volumetric adsorption capacity. *Journal of Materials Chemistry A*, 3(6), 2999–3005. <https://doi.org/10.1039/c4ta05116e>
- Tian, T., Zeng, Z., Vulpe, D., Casco, M. E., Divitini, G., Midgley, P. A., Silvestre-Albero, J., Tan, J. C., Moghadam, P. Z., & Fairen-Jimenez, D. (2018a). A sol-gel monolithic metal-organic framework with enhanced methane uptake. *Nature Materials*, 17(2), 174–179. <https://doi.org/10.1038/NMAT5050>
- Tian, T., Zeng, Z., Vulpe, D., Casco, M. E., Divitini, G., Midgley, P. A., Silvestre-Albero, J., Tan, J. C., Moghadam, P. Z., & Fairen-Jimenez, D. (2018b). A sol-gel monolithic metal-organic framework with enhanced methane uptake. *Nature Materials*, 17(2), 174–179. <https://doi.org/10.1038/NMAT5050>
- Tranchemontagne, D. J., Hunt, J. R., & Yaghi, O. M. (2008). Room temperature synthesis of metal-organic frameworks: MOF-5, MOF-74, MOF-177, MOF-199, and IRMOF-0. *Tetrahedron*, 64(36), 8553–8557. <https://doi.org/10.1016/j.tet.2008.06.036>
- Tranchemontagne, D. J., Mendoza-Cortés, J. L., O’Keeffe, M., & Yaghi, O. M. (2009). Secondary building units, nets and bonding in the chemistry of metal-organic frameworks. *Chemical Society Reviews*, 38(5), 1257–1283. <https://doi.org/10.1039/b817735j>
- Tranchemontagne, D. J., Ni, Z., O’Keeffe, M., & Yaghi, O. M. (2008). Reticular chemistry of metal-organic polyhedra. *Angewandte Chemie - International Edition*, 47(28), 5136–5147. <https://doi.org/10.1002/anie.200705008>
- Veluswamy, H. P., Kumar, A., Seo, Y., Lee, J. D., & Linga, P. (2018). A review of solidified natural gas (SNG) technology for gas storage via clathrate hydrates. *Applied Energy*, 216(02), 262–285. <https://doi.org/10.1016/j.apenergy.2018.02.059>
- Vikrant, K., Kumar, V., Kim, K. H., & Kukkar, D. (2017). Metal-organic frameworks (MOFs): Potential and challenges for capture and abatement of

- ammonia. *Journal of Materials Chemistry A*, 5(44), 22877–22896.
<https://doi.org/10.1039/c7ta07847a>
- Wang, Z., & Cohen, S. M. (2009). Postsynthetic modification of metal–organic frameworks. *Chemical Society Reviews*, 38(5), 1315–1329.
<https://doi.org/10.1039/b802258p>
- Wen, H. M., Li, B., Li, L., Lin, R. B., Zhou, W., Qian, G., & Chen, B. (2018). A Metal–Organic Framework with Optimized Porosity and Functional Sites for High Gravimetric and Volumetric Methane Storage Working Capacities. *Advanced Materials*, 30(16), 1704792. <https://doi.org/10.1002/adma.201704792>
- Wen, H. M., Li, B., Yuan, D., Wang, H., Yildirim, T., Zhou, W., & Chen, B. (2014). A porous metal-organic framework with an elongated anthracene derivative exhibiting a high working capacity for the storage of methane. *Journal of Materials Chemistry A*, 2(29), 11516–11522.
<https://doi.org/10.1039/c4ta01860e>
- Wilmer, C. E., Farha, O. K., Yildirim, T., Eryazici, I., Krungleviciute, V., Sarjeant, A. A., Snurr, R. Q., & Hupp, J. T. (2013). Gram-scale, high-yield synthesis of a robust metal-organic framework for storing methane and other gases. *Energy and Environmental Science*, 6(4), 1158–1163.
<https://doi.org/10.1039/c3ee24506c>
- Wilmer, C. E., Leaf, M., Lee, C. Y., Farha, O. K., Hauser, B. G., Hupp, J. T., & Snurr, R. Q. (2012). Large-scale screening of hypothetical metal-organic frameworks. *Nature Chemistry*, 4(2), 83–89.
<https://doi.org/10.1038/nchem.1192>
- Worgull, M. (2009). Molding Materials for Hot Embossing. In *Hot Embossing*. pp 57- 112. Elsevier. <https://doi.org/10.1016/b978-0-8155-1579-1.50009-4>
- World Bank. (2014). *CO2 emissions (kt) | Data*. Retrieved
<https://data.worldbank.org/indicator/EN.ATM.CO2E.KT>
- Wu, H., Zhou, W., & Yildirim, T. (2009). High-capacity methane storage in metal-organic frameworks M2(dhtp): the important role of open metal sites. *J Am Chem Soc*, 131(13), 4995–5000. <https://doi.org/10.1021/ja900258t>
- Wu, H., Yildirim, T., & Zhou, W. (2013). Exceptional mechanical stability of highly porous zirconium metal-organic framework UiO-66 and its important implications. *Journal of Physical Chemistry Letters*, 4(6), 925–930.
<https://doi.org/10.1021/jz4002345>
- Wu, Y., Tang, D., Verploegh, R. J., Xi, H., & Sholl, D. S. (2017). Impacts of Gas Impurities from Pipeline Natural Gas on Methane Storage in Metal-Organic Frameworks during Long-Term Cycling. *Journal of Physical Chemistry C*, 121(29), 15735–15745. <https://doi.org/10.1021/acs.jpcc.7b03459>
- Xu, B., Li, P. W., & Chan, C. L. (2012). Extending the validity of lumped capacitance method for large Biot number in thermal storage application. *Solar Energy*, 86(6), 1709–1724. <https://doi.org/10.1016/j.solener.2012.03.016>

- Yaghi, O. M., & Li, Q. (2009). Reticular chemistry and metal-organic frameworks for clean energy. *MRS Bulletin*, *34*(9), 682–690. <https://doi.org/10.1557/mrs2009.180>
- Yaghi, O. M., O’Keeffe, M., Ockwig, N. W., Chae, H. K., Eddaoudi, M., & Kim, J. (2003). Reticular synthesis and the design of new materials. *Nature*, *423*(6941), 705–714. <https://doi.org/10.1038/nature01650>
- Yan, Y., Kolokolov, D. I., Da Silva, I., Stepanov, A. G., Blake, A. J., Dailly, A., Manuel, P., Tang, C. C., Yang, S., & Schröder, M. (2017). Porous Metal-Organic Polyhedral Frameworks with Optimal Molecular Dynamics and Pore Geometry for Methane Storage. *Journal of the American Chemical Society*, *139*(38), 13349–13360. <https://doi.org/10.1021/jacs.7b05453>
- Yot, P. G., Yang, K., Ragon, F., Dmitriev, V., Devic, T., Horcajada, P., Serre, C., & Maurin, G. (2016). Exploration of the mechanical behavior of metal organic frameworks UiO-66(Zr) and MIL-125(Ti) and their NH₂ functionalized versions. *Dalton Transactions*, *45*(10), 4283–4288. <https://doi.org/10.1039/c5dt03621f>
- Yuan, D., Zhao, D., Sun, D., & Zhou, H. C. (2010). An isoreticular series of metal-organic frameworks with dendritic hexacarboxylate ligands and exceptionally high gas-uptake capacity. *Angewandte Chemie - International Edition*, *49*(31), 5357–5361. <https://doi.org/10.1002/anie.201001009>
- Yusuf, K., Aqel, A., & ALOthman, Z. (2014). Metal-organic frameworks in chromatography. *Journal of Chromatography A*, *1348*, 1–16. <https://doi.org/10.1016/j.chroma.2014.04.095>
- Zhang, H., Deria, P., Farha, O. K., Hupp, J. T., & Snurr, R. Q. (2015). A thermodynamic tank model for studying the effect of higher hydrocarbons on natural gas storage in metal-organic frameworks. *Energy Environ. Sci.*, *8*(5), 1501–1510. <https://doi.org/10.1039/C5EE00808E>
- Zhang, H., Nai, J., Yu, L., & Lou, X. W. D. (2017a). Metal-Organic-Framework-Based Materials as Platforms for Renewable Energy and Environmental Applications. *Joule*, *1*(1), 77–107. <https://doi.org/10.1016/j.joule.2017.08.008>
- Zhang, M., Zhou, W., Pham, T., Forrest, K. A., Liu, W., He, Y., Wu, H., Yildirim, T., Chen, B., Space, B., Pan, Y., Zaworotko, M. J., & Bai, J. (2017b). Fine Tuning of MOF-505 Analogues To Reduce Low-Pressure Methane Uptake and Enhance Methane Working Capacity. *Angewandte Chemie - International Edition*, *56*(38), 11426–11430. <https://doi.org/10.1002/anie.201704974>
- Zhao, D., Timmons, D. J., Yuan, D., & Zhou, H. C. (2011). Tuning the topology and functionality of metal-organic frameworks by ligand design. *Accounts of Chemical Research*, *44*(2), 123–133. <https://doi.org/10.1021/ar100112y>
- Zhou, H. C., Long, J. R., & Yaghi, O. M. (2012a). Introduction to metal-organic frameworks. *Chemical Reviews*, *112*(2), 673–674. <https://doi.org/10.1021/cr300014x>

Zhou, N., Fridley, D., McNeil, M., Zheng, N., Ke, J., & Levine, M. (2012b). China's energy and carbon emissions outlook to 2050 (No. LBNL- 4472E). Lawrence Berkely National Lab (LBNL), Berkely, CA (United States), pp: 41.
<https://china.lbl.gov/sites/all/files/lbl-4472e-energy-2050april-2011.pdf>

List of Publications

- Mahmoud, E., Ali, L., El Sayah, A., Alkhatib, S. A., Abdulsalam, H., Juma, M., & Al-Muhtaseb, A. A. H. (2019). Implementing Metal-Organic Frameworks for Natural Gas Storage. *Crystals*, 9(8), 406.
<https://doi.org/10.3390/cryst9080406>